Title
The Critical Role for Type-2 Dendritic Cells in Antitumor Immune Responses

Author
Binnewies, Mikhail

Publication Date
2018

Peer reviewed|Thesis/dissertation

The Critical Role for Type-2 Dendritic Cells in Antitumor Immune Responses

by

Mikhail Binnewies

DISSERTATION

Submitted in partial satisfaction of the requirements for the degree of

DOCTOR OF PHILOSOPHY

in

Developmental and Stem Cell Biology

in the

GRADUATE DIVISION

of the

UNIVERSITY OF CALIFORNIA, SAN FRANCISCO

[redacted]

ACKNOWLEDGEMENTS

First and foremost, I would like to thank Dr. Max Krummel for the guidance and mentorship he has provided throughout my time in graduate school. Max inspired me through his incredible energy and enthusiasm and has always encouraged me to perform research that is thoughtful, innovative and fun. I would like to thank my high school AP Biology teacher, Mr. Sapp, whose teaching acted as the catalyst for encouraging my curiosity of the natural world. I would like to thank Drs. Lindsay Hinck and Emmanuelle Passegué for guidance during my initial scientific training. I would also like to thank lab members Miranda Broz, Bijan Boldajipour, Mark Headley, Edward Roberts, Megan Ruhland, Kevin Barry and Adriana Mujal for their friendship and mentorship. I would also like to thank my longtime collaborator Joshua Pollack. I would like to thank members of my thesis committee Clifford Lowell, Michael Rosenblum and Mark Anderson. They have provided sage advice and helpful feedback that has guided my thesis work. I would also like to thank my longtime non-science friends, particularly Nat, Thom, Jordan, Matt, Alex and Aram, for their years of brotherhood and support. Lastly, I would like to thank my family – both those alive and dead – for a lifetime of unconditional love and relentless bickering. To my wife Anna, your love and support has made this whole process achievable and somewhat bearable. I love you dearly.

The text and figures within Chapter 1 are adapted from Binnewies, M. et al. Understanding the tumor immune microenvironment (TIME) for effective therapy. *Nat Med* **24,** 541-50 (2018). The text and figures within Chapter 2 were done in collaboration primarily with Adriana Mujal, Joshua Pollack and Alexis Combes with

supervision by Max Krummel. Adriana Mujal contributed toward experimental design and execution. Joshua Pollack computationally processed the single-cell RNA sequencing data and assisted with downstream analysis. Alexis Combes analyzed and interpreted all human data.

The Critical Role for Type-2 Dendritic Cells in Antitumor Immune Responses

Mikhail Binnewies

ABSTRACT

The clinical successes in immunotherapy have been both astounding and at the same time unsatisfactory. Countless patients with varied tumor types have seen pronounced clinical response with immunotherapeutic intervention; however, many more patients have experienced minimal or no clinical benefit when provided the same treatment. Even as our ability to isolate and assay individual immune components from the tumor microenvironment (TME) has improved, the immunological features that dictate therapeutic success or failure are poorly understood. As technology has advanced, so has the understanding of the complexity and diversity of the immune context of the TME and its influence on response to therapy. As cancer treatments move away from broadly eliminating dividing cells to specifically activating components of the immune system within the TIME, our understanding of the cell types critical for eliciting antitumor responses must be better understood.

Just as tumors can been subcategorized based on pathological and genetic features, categorizing tumors based on their TIME is equally informative. Specific combinations of immune populations within TIME can be highly predictive of both survival and response to immunotherapy. Antigen presenting cells (APCs), and in particular dendritic cells (DC), are emerging as critical components of a responsive TIME. DC have long been recognized for their exquisite ability to bridge detection of a

harmful pathogen or virus with the activation of an adaptive T cell response. More recent work from our lab and others has highlighted the function that specific DC populations have in activating $CD8^+$ T cells within the tumor-draining lymph node (tdLN) and tumor. However, $CD4^+$ conventional T cells (T_{conv}) are emerging as critical partners for productive antitumor responses, but the conditions required for effective $CD4^+$ T_{conv} activation remain poorly understood.

Differentiation of proinflammatory $CD4^+$ conventional T cells (T_{conv}) are critical for productive antitumor responses yet their elicitation remains poorly understood. We exhaustively characterized myeloid cells in tumor draining lymph nodes (tdLN) of mice and identified two subsets of conventional type-2 dendritic cells (cDC2) that traffic from tumor to tdLN and present tumor-derived antigens to $CD4^+$ T_{conv}, but then fail to support antitumor $CD4^+$ T_{conv} differentiation. Regulatory T cell (T_{reg}) depletion enhanced their capacity to elicit strong $CD4^+$ T_{conv} responses and ensuing antitumor protection. Analogous cDC2 populations were identified in patients, and as in mice their abundance relative to T_{reg} predicts protective $ICOS^{hi}$ $PD\text{-}1^{lo}$ $CD4^+$ T_{conv} phenotypes and survival. Further, in melanoma patients with low T_{reg} abundance, intratumoral cDC2 density alone correlates with abundant $CD4^+$ T_{conv} and with responsiveness to anti-PD-1 therapy. Together, this highlights a pathway which restrains cDC2, and whose reversal enhances $CD4^+$ T_{conv} abundance and controls tumor growth.

TABLE OF CONTENTS

FIGURES

TABLES

CHAPTER 1: UNDERSTANDING THE TUMOR IMMUNE MICROENVIRONMENT (TIME) FOR EFFECTIVE THERAPY

I. INTRODUCTION

The past decade has seen a revolution in cancer treatments by moving away from drugs that target tumors broadly (for example, chemotherapy and radiation) and toward the use of antibody-based immunotherapies that modulate immune responses against tumors. The first generation of antibody-based immunotherapy, so-called immune-checkpoint blockade (ICB), works by blocking the receptor and/or ligand interactions of molecules, such as CTLA-4 and PD-1, that are involved in dulling T cell activation or function[1]. ICB therapies have shown significant clinical benefit for a minority of patients, who demonstrate durable responses. Unfortunately, there is still an unmet clinical need for the majority of patients, who do not respond to ICB. Retrospective analyses of patient populations treated with ICB have revealed that there are classes of TIME that are associated with those tumors more prone to ICB responsiveness.

Deeper analysis of complexity within the TIME is likely to reveal advanced biomarkers that will prove fruitful in identifying patient populations responsive to current ICB therapy and will benefit the search for novel targets for therapeutic modulation. Past efforts to characterize the TIME have provided a foundation for future efforts in which recent technological advances in techniques such as high-resolution single-cell RNA sequencing, flow cytometry and imaging are expected to provide an unprecedented view of the composition, function and location of immune cells within the TIME. In this

Review, we provide a summary of the current knowledge centered around classes of TIME, focusing on the use of new technologies to study the TIME with increased granularity and the roles of systemic immune- and nonimmune-related factors in influencing TIME character and quality, and hence how tumors respond to immunotherapy.

II. CENTRAL CELL TYPES OF THE TIME

Along with tumor and stromal populations, the TME is infiltrated by more than 10 distinct immune cell types with varied abundance and function. Understanding the who, what and why of the TIME is of the utmost importance as each additional cell type certainly impacts the quality of antitumor responses, the immunological pressure applied to the tumor itself and the potential success of immunotherapy. Below is a summary of 8 distinct immune subsets whose presence in the TME is of functional consequence.

Monocytes. Monocytes represent a critically important class of evolutionarily conserved innate leukocytes of hematopoietic origin. In both mouse and man, monocytes develop in a colony-stimulating factor 1 (CSF-1) dependent manner primarily in the bone marrow, through differentiation of monocyte-committed common monocyte progenitor (cMoP) population[2,3]. Following generation in the bone marrow, monocytes egress and enter the blood in a CCR2-dependent manner[4]. Although it currently appears that there is a single monocyte population present within the bone marrow, two primary subtypes, classical and non-classical or “patrolling”, exist within the blood[5].

In human, classical monocytes are characterized by their expression of both CD14 and CD16, while in mouse they are described as being Ly6C^{hi}CCR2^{+}. Classical monocytes, hereby referred to as Ly6C^{hi} monocytes, are thought to persist in circulation for 1-2 days, at which point they have either entered a tissue site in response to a stimuli, differentiated into a non-classical monocyte, or died[6]. Following injury or inflammation, Ly6C^{hi} monocytes are recruited into tissue sites where they can begin express to a series of inflammatory molecules and and differentiate into macrophages[7]. While the fate of a Ly6C^{hi} monocyte in tissue is generally thought to be differentiation into a macrophage, recent evidence suggests the existence of a tumor-resident tissue monocyte, which lacks overt macrophage or dendritic cell (DC) gene expression programs[8]. The presence of a "tissue-resident" Ly6C^{hi} monocyte population raises significant intrigue, particularly in questions related to the role of monocytes in the tumor microenvironment, where a discrete role for monocytes beyond that of a tumor-associated macrophage (TAM) precursor population is unclear.

Studies on a heterogeneous population of cells known as monocytic myeloid-derived suppressor cells (mMDSC)[9], which likely includes monocytes and macrophages, have been shown to promote tumor growth through the production of various immunosuppressive cytokines and factors[10-12] and the suppression T cell proliferation and function[13], suggesting that perhaps, even as an undifferentiated precursor monocytes may contain functional capacity of consequence. Furthermore, a recent study using multiphoton intravital imaging of the lung pre-metastatic site in mice revealed that as pioneering metastatic tumor cells arrived and died, distinct waves of myeloid cells ingested tumor material, supplying antigen to both pro- and anti-tumor

immune compartments [14]. Monocytes were found to engulf the majority of tumor material, potentially sequestering valuable tumor antigen from stimulatory DC populations and genetic reductions in monocytes resulted in higher antigen loads in those DC.

Non-classical monocytes, hereby referred to as Ly6C^{low} monocytes, are described in human as being CD14^{low} CD16^{+} and mouse as Ly6C^{low}CCR2^{-}Nr4a1^{+}[8]. Unlike their Ly6C^{hi} monocyte counterparts, the function and critical features of Ly6C^{low} monocytes are poorly understood, particularly in the tumor microenvironment. Ly6C^{low} monocytes are generally characterized as being blood-resident, which helps explain data suggesting a role for them in the surveying of endothelial integrity[15,16]. While the role and even presence of Ly6C^{low} monocytes in the tumor microenvironment is debatable, Ly6C^{low} monocyte involvement in the metastatic site is more clear. A recent study[17] using Nr4a1-deficient mice, which lack Ly6C^{low} monocytes, demonstrated that in the absence of Ly6C^{low} monocytes tumor metastatic burden significantly increased but could be reduced by adoptive transfer of Nr4a1-proficent LyC^{low} monocytes. It was shown that infiltrated Ly6C^{low} monocytes detect tumor through CX3CR1 and were capable of phagocytosing tumor material.

Tumor-associated macrophages. Tumor associated macrophages (TAM) encompass a population of macrophages that reside primarily in the tumor or metastatic site. TAM are perhaps the most extensively studied and well characterized immune population within the TIME, primarily because of their abundance in the TIME relative ease of isolation[18]. While *in vitro* derived macrophages have been shown to be tumor-

eliminating[19], TAM are largely considered pro-tumoral immune population due to their production of pro-tumoral factors (EGF, IL-10, TGFb), expression of immune inhibitory molecules and T cell inhibitory capacity[20]. While generally characterized as a single population of cells, being the tumor-borne equivalent of a tissue macrophage, TAM instead likely represent a class of cells that is diverse in nature due to the distinct tumor environments and cytokine mileu in which they reside[21].

Recent data in mice suggests that the immunological origin of TAM (yolk-sac or monocyte-derived) can have a significant impact on their overall suppressiveness. In studies of spontaneous mouse PDAC, yolk-sac-derived tumor-associated macrophages (YS-TAM), which are seeded into tissues in early development and thus before malignant transformation were shown to be more tumor-supporting than monocyte-derived TAM[22]. The authors noted comparable expression of immune inhibitory and immune stimulatory receptors on both YS-TAM and monocyte-derived TAMs but demonstrated that tumor burden was significantly reduced only by loss of YS-TAM, and not monocyte-derived TAMs, suggesting a more immunologically suppressive role for YS-TAM. Since YS-TAM are theoretically more dominant during the early stages of malignant development and thus during the initial adaptive anti-tumor response, this may make elimination of nascent tumors fundamentally different compared to the targeting of more advanced tumors. While the results of this paper are intriguing, the origin of TAM in different tumor types might be ontologically and functionally distinct. In the *MMTV-PyMT* breast cancer model, the proportion of exhausted PD-1+ CD8+ T cells have been found to increase in parallel with monocyte-derived TAM[23]. In this study, the

authors found that depletion of monocyte-derived TAMs and not tissue-resident macrophage equivalent relieved suppression of cytotoxic T cells.

The inconsistencies of which ontologically distinct macrophage subset is the dominantly immunosuppressive and tumor-promoting type might have more to do with macrophage phenotype than origin. While the specific macrophage phenotype or subset most involved in T cell dysfunction in tumor progression is unclear and the diversity of macrophage states *in vivo*[24] is still quite an open question, *in vitro* macrophages can be generated with two extremes of phenotypes suggested to be tumoricidal (M1) and pro-tumorigenic (M2) [25,26]. The plasticity of these cells makes therapeutic targeting challenging, but recent studies have shed more light on the molecular switches that control macrophage phenotype. One source of phenotypic switching from immunostimulatory to immune-inhibitory transcriptional macrophage programming may be controlled by either BTK[27], a signal transducer downstream of the bacterial lipopolysaccharide receptor TLR4, or PI3Ky[28], a complex signaling molecule linked to the regulation of central myeloid transcriptional regulators NFκB and C/EBPβ as inhibition of either restored anti-tumor cytotoxic T cell responses, demonstrating the involvement of these pathways in promoting immune tolerance. In pancreatic cancer, signaling of the innate immune receptor Dectin-1 signaling promotes tolerogenic macrophage phenotype and T cell suppression facilitating tumor progression[29]. Together, these data indicate that therapeutic targeting of macrophages, to alter their phenotype, could alleviate immune suppression and improve anti-tumor immunity.

Neutrophils. Neutrophils are the most abundant granulocyte population present with in the polymorphonuclear family and critical for defense against pathogens, including viruses and bacteria. Similar to monocytes, neutrophils are produced in the bone marrow but instead require the cytokine granulocyte-colony stimulating factor (G-CSF)[30] for their development.

While the role for neutrophils in pathogenic elimination is well established, their role in cancer development is less clear. Several preclinical mouse cancer models revealed elevated neutrophil proportions in the circulation and accumulation in peripheral organs during tumor progression[31-34]. Neutrophil ablation in the primary tumor has consistently shown reduced tumor burden– supporting a pro-tumoral role for neutrophils[35]. Neutrophil suppression of adaptive immune responses and production of molecules like elastase[36] have been suspected to be mechanisms through which neutrophils support tumor growth, however, additional work is required to fully understand the tumor-promoting abilities of neutrophils.

Conventional Dendritic Cells. Conventional dendritic cells (cDC) represent a subset of professional antigen presenting cells (APC), which are able to initiate activation of T cells through the presentation of self and foreign antigens on MHC-I and MHC-II, T cell co-stimulation through expression of CD80 and CD86, and production of cytokines critical for effector differentiation of T cells[37]. cDC are bone-marrow derived but seed peripheral tissues as a pre-DC precursor population where they differentiate and divide into a committed cDC[38]. Within cDC exist two distinct cellular lineages (cDC1 and

cDC2) which differ in their transcription factor requirements, surface marker expression and function[39].

While innate in origin, cDC act as the critical linker between innate and adaptive immunity. The type of antigen cDC engulf and the signals they receive while in the periphery dictate the resultant T cell response that is initiated in the draining lymph node. As the arbiters of initiating adaptive immune responses, understanding the factors that influence cDC and promote productive versus non-productive T cell activation are critical. As the role for cDC in anti-tumor responses are becoming more clear, it is well accepted that cDC are central to what is termed the "cancer immunity cycle"[40], the process through which DC sample and process tumor antigen within a primary tumor, receive stimulus to migrate to the tumor draining lymph node (tdLN) and initiate adaptive T cell responses.

cDC1 are defined by their expression of XCR1[41] and their development requirement for the transcription factors BATF3[42], IRF8[43], ID2[44] and NFIL3[45]. cDC1 exist as two major populations, one that is resident in lymphoid tissues ($CD8\alpha^+$ cDC1)[46] and one that surveys peripheral tissues and tumors but has the ability to migrate to draining lymph nodes to initiate T cell responses ($CD103^+$ cDC1)[41]. For the purposes of this introduction, the role of $CD8\alpha^+$ cDC1 will not be discussed further.

$CD103^+$ cDC1 along with $CD11b^+$ cDC2, utilize expression of the chemokine receptor CCR7 to traffic antigen from the periphery to the source of CCR7 ligand, CCL19 and CCL21, in the tdLN[47]. $CD103^+$ cDC1 are critical for directing $CD8^+$ T cell immunity as depletion of $CD103^+$ cDC1 abrogates $CD8^+$ T cell priming and reduces response to anti-PD-L1 checkpoint blockade[47,48]. Importantly, expansion and activation

of CD103$^+$ cDC1 synergized with immune checkpoint blockade in multiple experimental models [48,49]. While this demonstrates that enhancing the functionality of these cells could improve the efficacy of immunotherapy, the abundance and localization of these cells in the tumor microenvironment is likely of profound importance.

CD103$^+$ cDC1 exist as a rare population within the tumor microenvironment[18]. While TAM numbers increase in tumors over time in mice and humans, mouse studies demonstrate that there is a progressive slow loss of CD103$^+$ cDC1. The importance of CD103$^+$ cDC1 cellular abundance has been demonstrated through gene expression analysis of human cancer biopsies that revealed a correlation between a 'CD103-associated gene signature', T cell infiltration into tumors and improved prognosis [18,47] but longitudinal studies have not yet confirmed that these cells are also progressively lost in human tumors. It has, however, been demonstrated in humans tumors that the increased abundance of BDCA-3+ DC (human equivalent of CD103$^+$ cDC1) positively correlates with responsiveness to immune checkpoint blockade (unpublished data). Considering that CD103$^+$ cDC1 are potent activators of anti-tumor CD8$^+$ T cells [18,42,47,48,50], it makes sense that their abundance would influence outcome.

cDC2 commonly express SIRPα[46] and require IRF4[51] and ZEB2[52] for their development. In contrast to CD103$^+$ cDC1, cDC2 are considered to be important for the initial activation of CD4$^+$ T cells through presentation on MHC-II[46]. In humans a population of BDCA-1 (CD1C) expressing DC present in peripheral tissues[53] and blood appear[54] to be the most likely direct comparator to the cDC2. Unlike cDC1, cDC2 contain substantial heterogeneity in both marker expression, transcription factor dependency and function. In the tumor, however, the diversity of cDC2 populations is

unclear. $CD11b^+$ cDC2 have been identified within the tumor and shown to induce both $CD4^+$ T cell proliferation and T_h17 differentiation, although both were only demonstrated *in vitro*[55]. While the abundance of CD103+ cDC1/BDCA-3+ DC has been shown to influence disease outcome, the functional consequence for presence of cDC2/BDCA-1+ DC in the TME in unknown. Prior to such studies, a full elucidation of the heterogeneity of cDC2 present in the TIME is necessary, as further heterogeneity within cDC2 is likely.

$CD8^+$ T cells. As mentioned before, anti-tumor $CD8^+$ T cell responses are initiated in the tdLN through interaction of a naïve $CD8^+$ T cell and a $CD103^+$ cDC1 presenting cognate tumor antigen on MHC-I. After receiving the appropriate signals, activated CD8+ T cells proliferate and differentiate into an effector phenotype (T_{eff}), characterized by expression of granzyme B, IFNγ and TNFα[56]. $CD8^+$ T_{eff} migrate through the blood and utilize a slew of chemokine receptors[57] and adhesion molecules[58] to enter the tumor. In an ideal setting, once in the tumor $CD8^+$ T_{eff} recognize tumor cells via ligation of their TCR with cognate antigen loaded pMHC-I, at which point CD8+ T_{eff} exert cytolytic function[40]. While this process does occur, the cancer immunoediting theory[59] posits that tumor cells will eventually evade CD8+ T cell elimination through trimming of vulnerable tumor cell clones and ultimately escape detection through utilization of discrete oncogenic pathways.

Additionally, several studies in mouse models have revealed that during *de novo* carcinogenesis, anti-tumor T cells fail to control tumor growth due to tumor-induced tolerance mechanisms[60-62]. Interestingly, T cell dysfunction in cancer shares many features with T cell exhaustion (**Figure 1.3**) observed in chronic viral infections[63], and is

generally characterized by high surface expression of inhibitory receptors (CTLA-4, PD-1, TIM-3, LAG-3, 2B4) on T cells, loss of effector functions like the production of cytokines IFNy, IL-2 and TNFα and loss of proliferative capacity[63,64]. The plasticity and reversibility of T cell exhaustion is an important and open question in studies of tumor immunology. Reversible and irreversible states of T cell exhaustion have been identified[65], with the irreversible exhausted cells being unresponsive to ICB like anti-PD-1/anti-PD-L1 therapy[66]. Preventing or reversing T cell exhaustion for long-term tumor control will be challenging and perhaps simultaneous targeting of other tolerance pathways, like the immunosuppressive TIME, or encouraging the priming of new T cell clones might be required to obtain durable anti-tumor T cell responses. T cell exhaustion and establishment of an immunosuppressive TIME are likely a linked event, with exhaustion occurring due to the combination of chronic exposure to tumor antigen[67], unproductive interactions from DC present in the TME[50], and exposure to immunosuppressive cytokines and cell types.

$CD4^+$ conventional T cells. $CD4^+$ conventional T cells **(**$CD4^+$ T_{conv}), like $CD8^+$ T cells, are initially activated in the draining LN through interaction with a DC presenting cognate antigen on MHC-II[68]. Similar to $CD8^+$ T cells, $CD4^+$ T_{conv} require co-stimulatory signals and specific cytokines in order for productive activation to occur. Due to their specialized function as supportive cells and not clearly involved in direct cytolytic killing, $CD4^+$ T_{conv} have the capacity to differentiate into a series of T helper (Th) subtypes, each characterized by production of distinct cytokines involved in the elimination of varied pathogenic threats[69]. T helper 1 (T_h1) cells, important for the elimination of

intracellular pathogens and productive antitumor responses, rely on the transcription factor T-bet for their development and are characterized by production of the cytokines IFNγ and TNFα[70]. T helper 2 (T_h2) cells, by contrast, require GATA3 and secrete IL-4 and IL-13[71]. T_h2 differentiation is associated with the elimination of helminth infections and in the tumor microenvironment has been shown to induce macrophage polarization toward a tumor-promoting, M2, phenotype[72]. T helper 17 (T_h17) cells require RORγT and STAT3 for their differentiation and produced the cytokines IL-17 and IL-22[73]. While primarily associated with the control of extracellular pathogens, T_h17 cells can have potently antitumor effects in specific contexts[74,75].

In tumor settings, $CD4^+$ T_{conv} have been demonstrated to be of critical importance[76,77]. As initiators and orchestrators of adaptive immunity, $CD4^+$ T_{conv} are critical for the priming and differentiation of cytolytic CD8+ T cells[78], supporting their expansion and survival in the tumor site and maintaining long-term CD8+ T cell memory responses[79]. Paradoxically, $CD4^+$ T_{conv} have also been shown to support tumor development directly[80] and indirectly[81]. Although $CD8^+$ T cells are understandably primary targets for therapeutic intervention, the important and often critical role of $CD4^+$ T_{conv} in the tumor makes them seem equally important for therapeutic manipulation.

Regulatory T cells. Just as the immune system is expert at elimination of pathogens, it is equally capable of suppressing itself in order to prevent reactivity to self and inflammation-associated damage. Central to the prevention of autoimmunity is a population of $CD4^+$ T cells known as regulatory T cells (T_{reg}). While the thymus serves as a major source of T_{reg}, extrathymic generation of T_{reg} can also occur through

conversion of $CD4^+$ T_{conv} in the periphery[82]. Within the thymus, differentiation of T_{reg} requires both high avidity interactions between TCR and self-antigen loaded MHC-II in addition to ample IL-2 receptor signaling[83].

Due to their role as potent suppressors of self-reactivity, T_{reg} are generally in high abundance within the tumor microenvironment[84] and their numbers are often associated with poor survival[85,86]. The suppressive potency of T_{reg} is evident in mouse as even short-term depletion of T_{reg} through genetic means induces a potent antitumor response[87]. To control immunity T_{reg} utilize a host of mechanisms, including production of both IL-10 and TGF-β1, excessive IL-2 consumption[88], and regulation of DC function through forced downregulation of costimulatory molecules CD80 and CD86[89]. The incredible suppressive function of T_{reg} makes them an obvious candidate for therapeutic elimination. Specific anti-CTLA-4[90] and anti-CD25 (IL-2RA)[91] antibody clones can induce substantial reduction in T_{reg} numbers, which induced antitumor responses as either single agent or synergized with ICB. Additionally, recent studies in human have identified tumor-specific Treg markers that have the potential to be exploited for therapeutic development.

III. TUMOR IMMUNE MICROENVIRONMENTAL CLASSIFICATION

Predicting responsiveness to ICB on the basis of high-resolution data on the character and quality of tumor immune infiltrates is a critical next step in improving the success of current ICB and developing next-generation immunotherapies. To date, large bodies of work have established moderate-resolution TIME data from low-resolution sources, such as bulk tissue microarrays and immunohistochemistry[92,93]. Techniques such as CIBERSORT[93] and XCell[94] estimate the abundance of immune

infiltrate into the tumor by using gene expression data from bulk tissues. Immunoscore [95] uses a combination of immunohistochemistry and bulk tissue gene expression data to stratify patients according to immune-related criteria and subsequently predict disease outcome.

Unfortunately, because of the nature of the datasets being used, most of these studies can estimate the immunological frequency and cellular status in the tumor microenvironment, but they lack information related to actual cellular proportions, cellular heterogeneity and deeper spatial distribution. Nonetheless, these techniques have gleaned substantial information that has provided a basis for classifying TIME according to broad criteria—the composition of the immune infiltrate and the character of the inflammatory response. Using next-generation technologies to improve TIME classifications should expand understanding of how the immunological composition and quality vary in tumor types (such as breast) and subtypes (such as luminal B), inform the success or failure of current ICB, and encourage the discovery of new immunotherapeutics. Currently, three broad classes of moderate-resolution TIME can be described according to recent human and mouse data. These three classes almost certainly miss key subclasses that should be revealed by ongoing studies using higher-resolution techniques to uncover heterogeneity in immunological composition, spatial distribution and function.

TIMEs that are broadly populated with immune cells but are relatively void of cytotoxic lymphocytes (CTLs) in the tumor core are termed infiltrated–excluded (I–E) TIMEs herein. I–E TIMEs have CTLs localized along the border of the tumor mass in the invasive margin or ‘caught’ in fibrotic nests (**Figure 1.1A**). I–E TIMEs are associated

with various epithelial cancers such as colorectal carcinoma (CRC),[96], melanoma[97] and pancreatic ductal adenocarcinoma (PDAC) [98], in which Ly6CloF4/80hi tumor-associated macrophages (TAMs) along the tumor margins have been hypothesized to prevent CTL infiltration into the tumor core[99]. Tumors classified as I–E TIMEs have been hypothesized to be poorly immunogenic or 'cold', although this hypothesis remains to be clearly verified[100]. I–E TIMEs, compared with more inflamed TIMEs, contain CTLs with low expression of the activation markers GZMB (GRZB) and IFNG and poor infiltration of CTLs into the tumor core. A lack of activation-marker expression and exclusion from the tumor core are characteristics indicative of immunological ignorance, an immunological state in which adaptive immunity is unable to recognize or respond to a pathogen or malignancy [101].

Infiltrated–inflamed (I–I) TIMEs (**Figure 1.1B**) are considered to be immunologically 'hot' tumors and are characterized by high infiltration of CTLs expressing PD-1 and leukocytes and tumor cells expressing the immune-dampening PD-1 ligand PD-L1. A subset of CRC, known as microsatellite instability high (MSI-H), bears a higher rate of nonsynonymous single-nucleotide polymorphisms, thus leading to increased numbers of neoepitopes and of tumor-infiltrating PD-1+CTLs, which have significantly higher responses to ICBs than do microsatellite instability low (MSI-L) or microsatellite stable (MSS) CRCs.

A subclass of I–I TIMEs, here termed TLS-TIMEs (**Figure 1.1C**), display histological evidence of tertiary lymphoid structures (TLSs), lymphoid aggregates whose cellular composition is similar to that in lymph nodes. TLSs are often[102] but not always correlated with a positive prognosis[103]. Similarly to lymph nodes, TLSs can contain a

substantial diversity of lymphocytes, including naive and activated conventional T cells, regulatory T (Treg) cells, B cells and dendritic cells (DCs) [104]. TLSs are generally present at the invasive tumor margin and in the stroma, and are thought to act as sites of lymphoid recruitment and immune activation that are typically formed in settings of enhanced inflammation, such as after administration of an autologous tumor vaccine[105] The ability to characterize a TLS thoroughly (for example, spatially, compositionally and functionally) is an important step in describing the TIME at a high resolution. For example, the TIME can be characterized in terms of not only the total number and type of cells present within a tissue but also the unique spatial collection of cells that may share a common program—in this case, a geographical feature established to recruit and activate adaptive immune cells. Spatial information paired with immunological composition and cellular status can help identify the presence of micro-niches within the TIME.

Broad classifications of immune context within a tumor microenvironment represent the first level of addressing how immunological composition and status (i.e., activated or suppressed) affect overall survival and dictate responsiveness to therapy. Beyond parsing the TIME with higher-resolution techniques, these classifications improve understanding of how mutational burden, oncogenes and distinct tumor types affect the establishment and maintenance of specific immunological compositions.

IV. INTERCONNECTIVITY OF TUMOR GENOTYPES AND PHENOTYPES IN THE TIME.

It remains to be understood how tumor-produced cytokines and chemokines, tumor oncogenes and mutation landscapes determine the composition of the TIME.

There are several examples strong enough to indicate relationships between both tumor genotype/phenotype and immunological composition, but these examples are not sufficiently strong for this understanding to be immediately applied toward therapeutic intervention (**Figure 1.2A**)

Tumor genotype contribution to cytokine production. Oncogene-driven expression of cytokines critical for the recruitment and phenotype of immune cells, particularly cells of the myeloid lineage, has been reported. In human melanoma, BRAFV600E, a mutated and highly oncogenic form of the MAPK family member BRAF, and STAT3, a potent transcriptional regulator often linked to oncogenic signaling, have been shown to drive expression of IL-6, IL-10 and VEGF, cytokines that promote a tolerogenic monocyte-derived DC phenotype *in vitro*, a process that would theoretically affect antitumor T cell function *in vivo* [106]

Multiple reports have demonstrated that KRASG12D-driven PDAC secretes high levels of the growth factor GM-CSF, which is associated with an increase in tumor-associated Gr-1+CD11b+ myeloid cells of reported immunosuppressive function[107,108]. Interestingly, genetic ablation or neutralization of GM-CSF in mice leads to decreased myeloid infiltration, improved CD8+ T cell infiltration into tumors and markedly smaller lesion size. These data demonstrate that an oncogene promotes the establishment of an immunosuppressive TIME that supports malignant development. Missing from these studies, however, is an assessment of the character of DC infiltration, because GM-CSF has been shown to induce the generation of CD11b+ DCs, a DC population ill-defined in the tumor[18].

Tumor-derived chemokines. Secretion of tumor-derived chemokines, driven by specific oncogenes, is another critical point of interaction between tumor genotype and recruited immune cells. Recent data in a BRAFV600E and Pten-deficient mouse model of melanoma suggest that constitutive tumor-intrinsic WNT/β-catenin signaling is associated with poor immune infiltration and ineffective antitumor T cells, largely because of a decrease in the recruitment and frequency of $CD103^+$ DCs.[109,110]. Transcriptional analysis of tumor cells and *in vitro* DC migration assays have revealed that constitutive WNT/β-catenin signaling leads to decreased production of Ccl4, a potent chemoattractant for a variety of myeloid cells including $CD103^+$ DCs, thus potentially explaining the decreased recruitment of $CD103^+$ DCs and the corresponding poor infiltration of $CD8^+$ T cells into the tumor microenvironment. Although the direct oncogenic determinant of expression is unclear, several studies in mice have reported that tumor-secreted CCL2 causes the recruitment of $CCR2^+$ classical monocytes to the tumor, where they differentiate into TAMs, a protumoral myeloid population[111].

Humoral Factors. There is also evidence for a role for humoral factors in regulating the TIME. Recent data from mice suggest that TIME-derived PTX3, a critical component regulating complement activation through interaction with factor H, plays an essential role in suppressing tumor growth by indirectly controlling monocyte recruitment and TAM phenotype[112]. Epigenetic profiling of human tumors has revealed hypermethylation of the PTX3 promoter, thus suggesting that human PTX3 may similarly affect the architecture of the TIME.

Paracrine feedback loops. Paracrine feedback loops of cytokines between specific immune infiltrates and tumor cells play critical roles in influencing tumor phenotype and ultimately metastasis. TAMs are prominent components of the TIME and are involved in cross-talk with tumor cells, thus resulting in tumorigenic reprogramming[113]. Tumors in both mice[114] and humans[115] have been found to secrete high levels of colony stimulating factor 1 (CSF-1), a potent chemoattractant, survival and differentiation factor for monocytes and macrophages[114], in addition to CCL2. T helper 2–[114] polarized $CD4^+$ T cells, through secretion of IL-4 and IL-13, have been shown to potentiate the ability of TAMs to secrete angiogenic growth factors, proteases and protumoral survival factors[81], including VEGF-A, MMP-9, EGF and uPA[114,116].

Modulating the stroma. In addition to tumor-intrinsic factors directly affecting immune cells within the TIME, tumor cells can elicit profound phenotypic changes in nonimmune stromal components that reside within the local tumor microenvironment and affect the TIME. Indeed, oncogenic BRAFV600E signaling in human melanoma cells has been shown to perturb T cell–mediated antitumor responses by modulating the phenotype of cancer-associated fibroblasts. BRAFV600E in melanoma drives production of IL-1α and IL-1β, thereby enhancing the ability of cancer-associated fibroblasts to suppress melanoma-specific CTLs, in part through COX-2 secretion and upregulation of the PD-1 ligands PD-L1 and PD-L2 [117]. Interestingly the loss of specific tumor suppressors in stromal cell types, has also been shown to influence the type and character of immune cells present within the TIME. For example, in a mouse model of chronic liver damage,

p53-deficient hepatic stellate cells, a stromal cell type, secrete factors that polarize TAMs toward a more protumorigenic M2-like phenotype often associated with immunosuppression[118]. Interestingly, that study has also revealed that natural killer cells, TAMs and resident Kupffer cells are less able to eliminate p53-deficient proliferating hepatic stellate cells *in vitro*, although the mechanism of dampened elimination of hepatic stellate cells is unclear.

The mutational landscape of the tumor and the TIME. Beyond the effects of tumor-derived cytokines, chemokines and nonimmune cells on the character of the TIME, the overall mutational landscape of tumor cells, a direct reflection of tumor immunogenicity, can dictate the extent and phenotype of immune infiltrate. A particularly strong example of this influence is in CRC (**Figure 1.2B**). As mentioned briefly in the previous section, CRC can be stratified through gene-expression-based subtyping into four consensus molecular subtypes (CMS1–4)[119]. For example, in CMS1 CRC, there are DNA mismatch-repair defects, as indicated by microsatellite instability or hypermutation rates. CMS1 tumors have been found to be deeply infiltrated with $CD8^+$ T cells and display global gene expression patterns consistent with a high number of T helper 1 (TH1) cells[96], as is indicative of an antitumor immune response. However, the antitumor response is likely to be moderated by the presence of immunosuppressive cell types, a protumor cytokine milieu and/or the expression of immune-checkpoint proteins including CTLA-4, PD-1, PD-L1 and IDO-1[120-122]. The expression of immune-checkpoint proteins by CMS1 CRC is notable, because those tumors show substantial responses to anti-PD-1 ICB, thus suggesting that the large mutational burden and high frequencies of

tumor-infiltrating $CD8^+$ CTLs and TH1 cells has opened up the potential for many T cell clones to become potently antitumor after tolerance is broken[123].

CMS4 CRC, characterized by tumor cells with a mesenchymal-like phenotype, is associated with poor prognosis and high expression of protumoral genes, including those associated with T helper 17 cells, the TGF-β pathway and the monocyte/macrophage lineage[121], on the basis of bulk tissue RNA expression. Hence, CMS4 CRC antitumor responses might be easily overwhelmed by a TIME skewed toward immunosuppression. CMS2 and CMS3 CRCs, tumors that are microsatellite stable, nonhypermutated and epithelial according to their gene expression, exhibit low-immune and low-inflammatory signatures and are typically PD-L1 negative. CMS2 and CMS3 CRCs have phenotypes suggestive of antigenically cold tumors, and in both cases the tumors have lower lymphocyte infiltration into the tumor than that observed in CMS1. CMS2–4 are thought to respond poorly to ICBs, partly as a result of low antigenic diversity and generally low tumor-infiltrating lymphocyte (TIL) numbers[121,123].

V. THE CONTRIBUTION OF SYSTEMIC FACTORS TO THE TIME

Understanding the spatiotemporal dynamics of the TIME necessitates dissecting the potential roles that systemic factors may have in predisposing certain TIMEs to be fostered. As the broad effects of factors such as exercise[124], age[125], diet[126], adiposity[127], the microbiome[128] and sex[129] on the immune system have become clearer, an understanding of how these factors directly affect the quality of the antitumor immune response has also emerged. Both these patient-intrinsic and tumor-dependent effects

intersect on many levels and will be important considerations in improving the efficacy of existing therapies or developing orthogonal immunotherapeutic approaches.

The systemic inflammatory state of an individual can affect the character of the TIME in premalignancies, thus leading to an occult tumor's eventual elimination or supporting progression to advanced disease. A recent study has found that patients with atherosclerosis treated with anti-IL-1β had lower incidence of lung cancer than did patients who had received placebo[130]. IL-1β has been shown to induce synthesis of COX-2, which in turn leads to high-level production of PGE2, a potent immunosuppressive molecule, in a subset of cancers. Aspirin, a COX inhibitor, has only very modest protective benefits when viewed across all cancers[131], although its use is associated with lower disease incidence in patient populations predisposed to develop specific types of cancer[132]. These findings may indicate key differences in the TIMEs of patient populations. Interestingly, COX inhibition may also have utility in cancer treatments, because it has been shown to synergize with anti-PD-1 therapy in established tumors [133].

As discussed above, tumors can make numerous cytokines and chemokines that attract and inform specific components of the immune system. Although these factors affect the local TIME itself, they can also become systemic, inducing broader changes in the tumor macroenvironment. Tumor cell production of the growth factors G-CSF[34] and GM-CSF, as well as of IL-6[134], can affect bone marrow myeloid progenitor expansion, thus leading to enhanced release of myeloid cells into circulation, and ultimately affect the number of circulating and tumor-infiltrating immunosuppressive myeloid cells and contribute to more severe disease and greater metastatic

burden[135,136]. Tumor-induced systemic factors can affect the bone marrow and in turn promote tumor infiltration of cancer-promoting immune components, including neutrophils[137], monocytes[138] and platelets[139].

Certain aspects that affect the tumor microenvironment predate tumor establishment. Both aging[140,141] and obesity[142] have been reported to produce a proinflammatory state and to lead to an increase in the number of suppressive immature myeloid cells in circulation. Moreover, sex hormones may lead to altered TIME responses in male as compared with female patients, because estrogen has been shown to activate the STAT3 pathway in human and mouse bone marrow myeloid progenitor cells, thereby leading to an increased presence of potentially suppressive myeloid cells in circulation[143]. In contrast, estrogen may also induce a more tolerogenic phenotype or subset in tumor DC populations[144], thus partially explaining the difference in tumor growth between male and female mice. There is an added uncertainty, at present, of the heterogeneity of the myeloid lineage as it exists in circulation and whether each of these features of patients may influence the exact same or different subpopulations of cells.

More clearly, the microbiome has been found to have an important role in determining DC functionality. Two recent studies have reported that responses to checkpoint blockade are dependent on the microbiomes of the mice studied[145,146]. Moreover, patients can be stratified according to their microbiomes, and this stratification is predictive of the response to anti-CTLA-4 therapy[146]. Both of these studies have hypothesized that this effect may be at least partly due to improvements in DC functionality either through improved maturation and cross-presentation leading to

improved $CD8^+$ T cell priming[145] or through improved $CD11b^+$ DC migration from the tumor and improved Th1 responses[146]. DC phenotype is also affected by the temperature of the animal being studied: placing mice under mild cold stress in laboratory conditions leads to increased tumor growth and reduced immune control[147], effects at least partly due to decreased DC functionality[148]. As such, the immune macroenvironment of a patient can dramatically affect the tumor microenvironment.

Tumor-derived factors, as well as those affecting myeloid cell production from the bone marrow, can also alter patient metabolic status, which in turn can influence antitumor immunity. Recent research has revealed that in the CT26 and KPC tumor models, tumor-derived IL-6 alters liver metabolism and consequently, in the context of caloric restriction, leads to increased corticosterone and suppressed antitumor immunity[149]. In this setting, tumor-derived factors alter systemic metabolic tone and consequently lead to alterations in the tumor microenvironment. Interestingly in other models, caloric restriction[149] or the administration of a fasting mimetic[150], both of which trigger autophagy, have led to improved antitumor immunity in mice. These fasting-related effects have been linked to potentiated responses to chemotherapy, partially as a result of increased TIL infiltration[151] loss of tumoral Treg cells[150].

These findings indicate that there may be more complexity to uncover regarding the effects of nutrition on tumor immunity and that the effects may be model dependent, in a manner analogous to the opposing effects of fasting on responses to bacterial and viral disease[152].These factors should thus be taken into account when considering potential orthogonal immunotherapeutic approaches as well as when deciding upon appropriate animal models for preclinical evaluation. The use of sex-matched, young

and lean mice in most animal studies may explain some of the failures of mouse studies to predict therapeutic responses in the more diverse human population. Indeed, given that population obesity rates are increasing and that most tumors develop in elderly patients, understanding these factors is likely to prove critical for understanding of the tumor microenvironment. Moreover, other factors such as housing temperature (although this factor may not affect patient treatment, because hospitals are kept relatively thermoneutral) may greatly affect the findings from experimental systems.

VI. FURTHER CHARACTERIZATION OF THE TIME

Major successes with ICB and the potential for substantial clinical effects are driving thousands of clinical trials. These successes include alternative ICB-like targets and drugs that modulate myeloid biology[153], which may be paired with nonimmunological drug approaches. Pharmaceutical companies and clinical investigators alike are well aware of the value of tracking biomarkers associated with tumor growth, but more attention must be paid to how the TIME of a specific patient is altered before, during and after a trial. Using high-dimensional techniques to characterize patients with improved granularity should reveal as much about human immunology in an *in vivo* setting as any experiment in a mouse could. Similarly to the cases of anti-CTLA-4 and anti-PD-1/PD-L1, breakthroughs will occur when basic-science discoveries are translated into actionable improvements in human disease. Therefore, the fastest route to demonstrable successes will depend on asking useful questions and using applicable animal models and valuable, innovative tools.

Because immunotherapeutic intervention is attempted in disparate tumor types, there is a growing need to identify the unifying features and critical differences that define distinct classes and subclasses of TIME, which relate to the likelihood of response to immunotherapeutics. For substantial progress to occur in this area, use of the highest-resolution methods will be critical to assess total cellular composition (for example, flow cytometry versus mass cytometry), functional status (for example, bulk RNA sequencing versus single-cell RNA sequencing) and cellular localization (for example, immunohistochemistry versus multidimensional immunohistochemistry) in parallel to define highly granular classes and subclasses of TIME. Major advances have already been made in stratifying patients according to tumor type. We believe that further stratification of patients on the basis of not only their tumor type but also their TIME type will yield better insight into overall survival and the likelihood of response to immunotherapeutics, and will provide vast datasets to help identify new druggable targets. This progress will be garnered by using the most cutting-edge techniques in multiparametric imaging[154], mass cytometry[155,156] and single-cell RNA sequencing[157]. Critical to this goal is that improved resolution of cellular composition and analysis of functional status and spatial distribution must be paired with relevant patient outcomes. In particular, by casting a wider unbiased net, it will be possible to detect subtle changes in rare populations while also appreciating prominent effector activation states *in situ*.

A major goal in moving into truly orthogonal pathways to treat cancers is to understand the fundamental conditions in which TIMEs are arrayed; these conditions almost certainly reflect genetic programs engaged by the tumors themselves, if not also by the tissue in which the tumor is located. Distinct collections of stroma, epithelium and

immune cell types present nearly countless ways to parse a TIME, but it is still unknown how many of these cellular combinations help permit the rapid cellular proliferation and disorganization associated with a growing tumor. To that end, parallel studies to characterize tissue-specific responses to pathogens, healing wounds, chronic viral infections and tolerance in the gut may provide powerful datasets for comparison with the classes of TIME, because they are all analyzed at this detail.

As immune–immune and immune–tumor interaction networks are better characterized, it will become possible to define classes of TIME and determine which cells, molecules and pathways are essential for suppressing antitumor immunity, and in what tumor contexts. In some cases, such definition may already be possible, because of the existence of failed, orphan, poorly efficacious drugs or drugs without an obvious direct application as immunotherapeutic agents. To advance immunotherapy, the state of thinking must be revamped in terms of the treatment goals (i.e., decreasing disease incidence versus combating advanced disease), and drugs that have had previous marginal success should be revisited. After paltry early clinical success, recent preclinical data in a mouse model of PDAC suggest that a combination of chemotherapy and anti-CD40 agonistic antibody unleashes a potent antitumor immune response; moreover, early data in humans show enhanced lymphocyte infiltration. Although investigations are still in their early days, drugs to normalize vasculature, alter metabolism and suppress individual components of the immune system may find new life in the clinic, either as single agents or in combination with ICB, for long-term use as prophylactic measures.

Translating clinical insights into improvements in mouse models is necessary to ensure that discoveries made at the bench can derive applicable and high-quality therapeutics. As classes of human TIME are elaborated (as described above), it is critical that parallel efforts take place to ascertain the best ways to generate reflective TIME in mouse models. Solid human tumors develop *in situ* and over long periods of time, characteristics not reflected in ectopic mouse tumor models, which very often grow in the subcutaneous space and are formed through bolus injection of thousands of highly malignant tumor cells. Ectopic mouse tumor models have been invaluable for preclinical validation of countless therapeutics but have fallen short of being good indicators of therapeutic efficacy in humans. Although genetically engineered mouse models of cancer have brought immuno-oncology research a step closer toward recapitulating the stepwise progression of human disease, the resultant spontaneous tumors still leave something to be desired. The discovery of CRISPR–Cas9 now allows for rapid and parallel introduction of numerous mutations or engineered constructs into a single mouse[158,159], thus changing how genetically engineered mouse models can be created, with less of an emphasis on severe oncogenic drivers and more of an emphasis on tunable oncogenic induction and mutational landscapes more similar to those in human disease.

Furthermore, major advances in the development of humanized mouse models have made xenografts with matching patient tumor and immune compartments possible, thereby enabling studies in which a patient's own adoptively transferred TILs can be used to recapitulate the exhaustion or the introduction of targeted gene reporter loci to visualize intravital tumor immune interactions. Although these models have

downsides, being able to implant human tumor tissue with a native mutational landscape into a partially reconstituted human immune repertoire represents major progress. Even if mouse models fail to ever fully recapitulate human disease, it is important to understand the minutiae that make the most difference in dictating therapeutic response versus nonresponse. Distilling a disease into a few critical parameters is challenging, but understanding what cell types can be modulated and when may enable the next biggest improvements in immunotherapy.

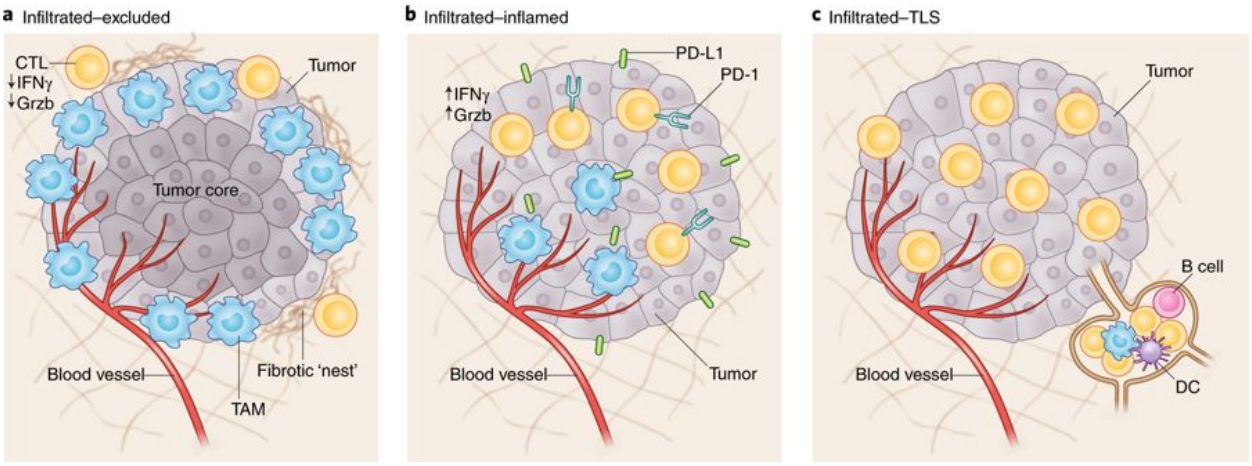

Figure 1.1 General classes of TIME.

Three classes of TIME are displayed. (**A**) I–E TIMEs are characterized by the exclusion of CTLs from the tumor core. CTLs in I–E TIMEs are instead present along the tumor periphery, where they can be found in contact with Ly6Clo F4/80+ tumor-associated macrophages or 'stuck' in fibrotic nests. (**B**) In comparison, I–I TIMEs are defined by an abundance of PD-L1 expression on tumor and myeloid cells and highly activated CTLs characterized by expression of Grzb, IFNγ and PD-1. In some subsets of I–I TIME, tumor cells will have defects in DNA mismatch repair (MSI-H), thus resulting in an increased number of neoepitopes. (**C**) TLS-TIMEs have histological evidence of containing TLSs, aggregates of immune cells with a composition similar to that in lymph nodes, including B cells, dendritic cells and Treg cells.

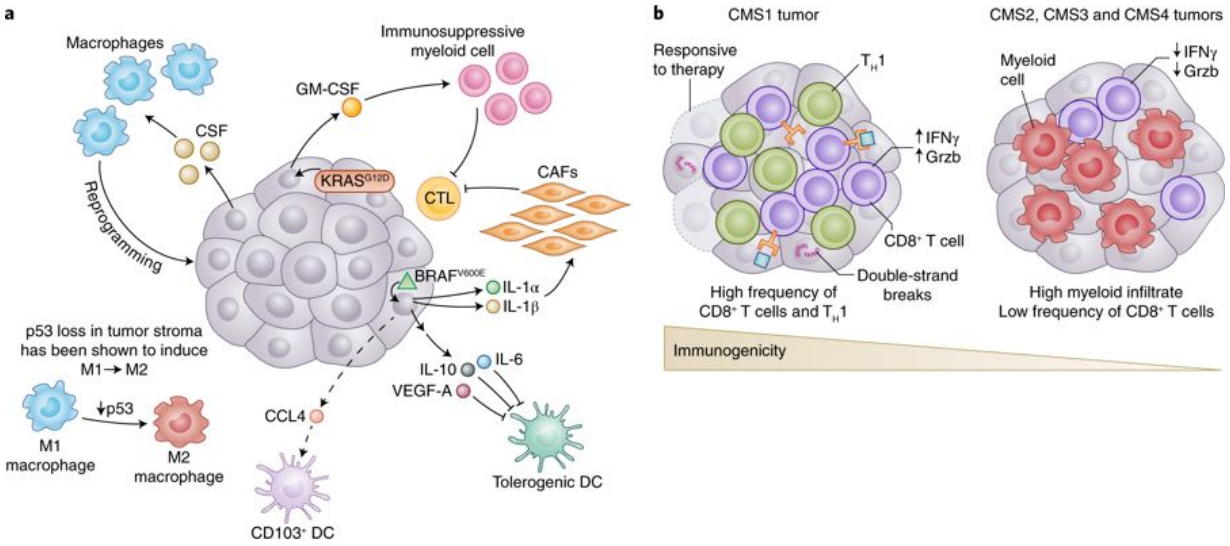

Figure 1.2 How tumor genotypes and phenotypes shape the TIME.

(**A**) Tumors are known to establish protumoral and immunosuppressive environments to support their growth and promote immune evasion. Central to building an immunosuppressive TIME are oncogenes and aberrant signaling pathways that lead to the production of cytokines and chemokines with potent effects. The tumor shown is representative of a spectrum of cancer types. In melanoma, $BRAF^{V600E}$ (green triangle) has been shown to induce constitutive WNT/β-catenin signaling, which in turn decreases production of CCL4, a chemokine important for the recruitment of $CD103^{+}$ DCs. Additionally, $BRAF^{V600E}$ has been shown to induce expression of factors such as IL-10 and IL-1α, which can induce tolerogenic forms of DC and cancer-associated fibroblasts (CAFs), respectively. Oncogenic $KRAS^{G12D}$ in PDAC leads to the secretion of GM-CSF, corresponding to increased development of $CD11b^{+}$ myeloid cells with reported immunosuppressive function. Deficiency in p53 in hepatic stellate cells, a stromal population, leads to production of factors that polarize TAMs from the immunoactivating M1 phenotype to the immunosuppressive M2 phenotype. Interestingly, many tumors have been shown to secrete high levels of the

monocyte/macrophage-promoting cytokine CSF-1. (**B**) The mutational landscape of tumors can profoundly affect the quality and character of the TIME. In CRC, there are four consensus molecular subtypes (CMS1–4). CMS1 is defined by defects in DNA mismatch repair leading to microsatellite instability or hypermutation rates. Because of the abundance of possible neoepitopes, CTL infiltration is generally high, and CTLs display gene expression patterns indicative of an ongoing immune response. Patients with CMS1 tumors have generally more favorable outcomes with checkpoint-blockade treatment than do patients with CMS2–4. Although there are differences in the histological and immunological character of CMS2, 3 and 4 CRC subtypes, they are generally less immune infiltrated, as is suggestive of antigenically cold tumors.

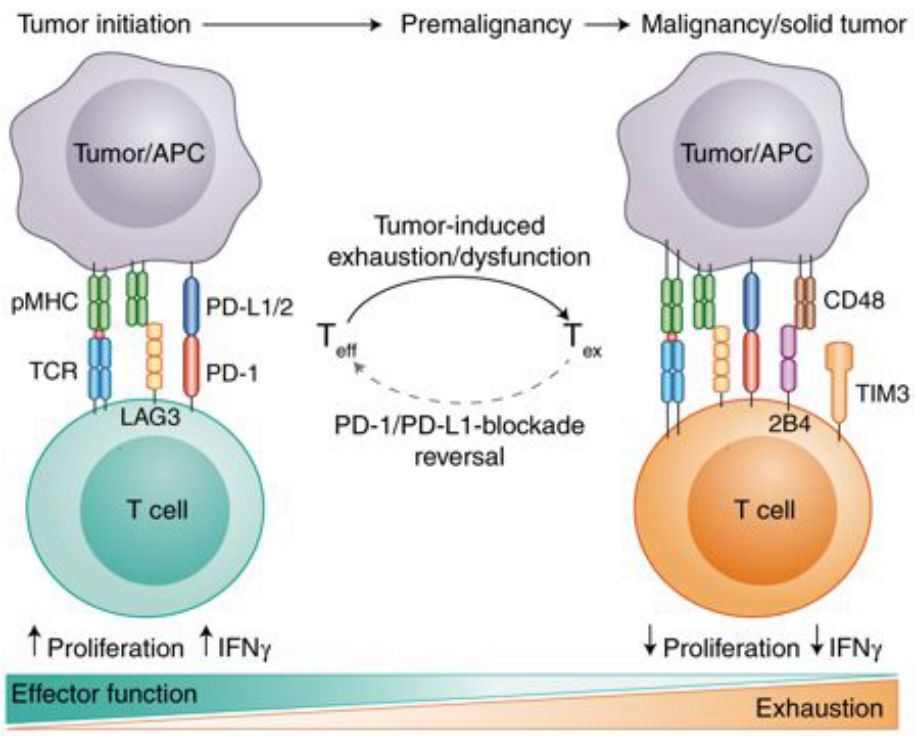

Figure 1.3 T cell exhaustion within the TME.

A major contributing factor in the failure to immunologically reject tumors stems from induction of T cell exhaustion, a state in which T cells become less responsive to antigens and are ineffective at providing T cell help or eliminating appropriate targets. Recent evidence suggests that T cell exhaustion occurs rapidly after oncogenic initiation, possibly because of chronic antigen exposure on tumor cells. As a T cell transitions from effector (Teff) to exhausted (Tex), there is increased expression of exhaustion-associated molecules such as LAG3, 2B4 and TIM3, and downregulation of effector cytokines such as IFNγ. From a therapeutic standpoint, epigenetic evidence suggests that there are types of T cell exhaustion that are irreversible, thus potentially explaining why some patients are completely unresponsive to some forms of ICB. APC,

antigen-presenting cell; pMHC, peptide-bound major histocompatibility complex; TCR, T cell receptor.

CHAPTER 2: UNLEASHING TYPE-2 DENDRITIC CELLS TO DRIVE PROTECTIVE ANTITUMOR CD4+ T CELL IMMUNITY

I. INTRODUCTION

Adaptive T cell responses are critical for controlling tumor growth through production of inflammatory cytokines and direct cytolytic targeting. Recent therapeutic advances that block inhibitory T cell checkpoint molecules like CTLA-4 or PD-1/PD-L1 have demonstrated clinical success, but in only a subset of cancer patients [160-163]. Recent evidence suggests that tumors often promote the generation of dysfunctional and exhausted T cells with deficient effector capacity reminiscent of exhaustion observed following chronic viral infection [67]. T cell exhaustion is enforced at the chromatin level such that many T cells in the tumor microenvironment (TME) are likely not able to be rescued by immune checkpoint blockades (ICB) [65,66]. Thus, in those patients with poor T cell infiltration or irreversibly exhausted T cells, additional steps, such as improving *de novo* priming of effector T cells, may be necessary to engage effective antitumor immunity [65,164].

While $CD8^+$ T cells are considered a primary immunotherapeutic target due to their classic role in tumor cell cytolysis, $CD4^+$ T_{conv} are emerging as an important contributor to antitumor responses. In immunogenic settings, effector $CD4^+$ T_{conv} augment immunity through licensing of dendritic cells (DC) [165] and stimulating pro-inflammatory myeloid cell programs [166]. $CD4^+$ T_{conv} have also been documented to improve the quality of effector $CD8^+$ T cell responses to apoptotic cell antigens (a common source of tumor antigen) and contribute to T cell memory programming and

maintenance [167]. Intriguingly, $CD4^+$ T_{conv} have been described as having direct antitumor cytolytic function[168,169] and HLA-DR expression on human tumor cells (MHC-II in mouse) has been identified as a biomarker for anti-PD-1/PD-L1 responsiveness [170]. Notably, effective anti-CTLA-4 therapy results in a systemically circulating population of $ICOS^{hi}$ $PD\text{-}1^{lo}$ $CD4^+$ T helper 1-like (T_h1-like) effector $CD4^+$ T_{conv} critical for an antitumor response [171]. Conversely, presence of a $PD\text{-}1^{hi}$ $CD4^+$ T_{conv} phenotype, correlated with extensive tumor burden and likely T cell exhaustion, has been shown to be a negative prognostic indicator for checkpoint blockade [172]. As such, the processes that contributes to antitumor $CD4^+$ T_{conv} activation and differentiation merit further investigation.

Generation of newly activated antitumor T cell clones typically requires their activation in secondary lymphoid organs such as the tumor-draining lymph node (tdLN), followed by subsequent infiltration into the tumor mass [40]. Initiation of an adaptive T cell response is driven by one or more types of innate myeloid antigen-presenting cells (APC) such as conventional dendritic cells (cDC) that present tumor antigen, co-stimulatory molecules, and cytokines to cognate antigen-specific T cells. Given the shortcomings in endogenously-generated antitumor T cell responses, there has long been therapeutic interest to improve cDC numbers and functionality as a means to boost T cell effector potential. Approaches such as cellular vaccines or administration of cDC growth factors, however, remain susceptible to endogenous immunosuppressive cells such as T_{reg} [83] which can potently suppress cDC [173], although given the complexity of cDC populations, it is currently unclear if specific populations of cDC are selectively impacted.

Diverse in nature, cDC can be broadly divided into cDC1 and cDC2 populations that arise through distinct pre-DC lineages [39] and can be either resident to the LN, or migrate in from peripheral tissues bearing antigen [37]. Importantly, cDC1 and cDC2 often take on specialized roles in $CD8^+$ T cell and $CD4^+$ T_{conv} priming processes through their differential use of antigen processing and presentation pathways [174], production of effector cytokines [37], and spatial localization within the LN [175]. cDC1 have been identified as critical for directing $CD8^+$ T cell immunity to various pathogens [176,177] and in mediating spontaneous antitumor $CD8^+$ T cell responses [18,47,48,50,109]. In contrast, cDC2 contain substantial heterogeneity and they preferentially initiate $CD4^+$ T_{conv} responses in a variety of immunological models [178,179]. While the division of labor between cDC1 and cDC2 in engaging $CD8^+$ T cells and $CD4^+$ T_{conv}, respectively, is an established phenomenon, this may depend on the tissue type and each may have multiple capabilities to tolerize or activate respective cells types, depending on the nature of the immune challenge. On the whole, the specific cDC roles in eliciting antitumor $CD4^+$ T_{conv} immunity remains unresolved.

We therefore applied single-cell RNA-sequencing (scRNA-seq) to myeloid populations from tdLNs in mouse and human to understand the true diversity and function of cell types present, how they differ with cancer, and how the variance might affect the nature of the $CD4^+$ T_{conv} that are available for tumor efficacy. Key in this was to understand how therapeutic intervention might alter the outcome of $CD4^+$ T_{conv} priming. Additionally, we sought to understand whether human cancer biology paralled the mouse and assembled cohorts of patient biopies to determine how $CD4^+$ T_{conv} phenotype and cDC composition were connected.

II. RESULTS

Myeloid heterogeneity at single cell resolution

To comprehensively study the myeloid populations capable of priming anti-tumor $CD4^+$ T_{conv}, we queried myeloid heterogeneity in the tdLN by sorting non-lymphocyte ($CD90.2^-$ $B220^-$ $NK1.1^-$) myeloid cells ($CD11c^+$ or $CD11b^+$) from the tdLN of B16-F10 tumor-bearing mice. We performed scRNA-seq using the 10X Genomics Chromium platform paired with deep sequencing. Analysis of 4133 tdLN myeloid cells yielded 10 high quality and unique population clusters (**Figure 2.1A, 2.8A)**.

To rigorously identify the myeloid populations and determine how they related to those previously described in other settings, we generated gene signatures of cell populations expected to be present in the LN from samples available from the Immunological Genome Project (ImmGen) database [180] and plotted expression of these signatures on the tdLN *t*-SNE plot. This allowed us to assign cellular identities to each cluster (**Figure 2.1B** and **Table 2.1**), apart from clusters 8 and 9, as they appeared to be lymphocyte contaminates and were excluded from further analysis (data not shown).

We then utilized gene overlays of individual canonical myeloid markers to further explore the cluster identities. *Ccr7* and *Itgax* demarcarcated migratory (clusters 0, 1, 2, 4 and 6) and resident (clusters 3, 5 and 7) DCs, consistent with our assignments and the known biology (**Figure S2.8B**). DC clusters (0-4, 6-7) were further confirmed using canonical genes *Zbtb46* and *Flt3* (**Figure S2.8C**), whereas monocytes and T cell zone macrophages (TZ Macrophages), which are unable to prime $CD4^+$ T_{conv} [181], both occupied cluster 5, but localized to opposite sides of the cluster (**Figure S2.8D**).

We performed differential expression (DE) analysis for each myeloid cluster versus all other clusters and generated heatmaps for the top 10 most differentially expressed genes (**Figure 2.1C** and **Table 2.2**). In addition to highlighting key genes that contributed to the unbiased segregation of these populations, a number of markers also validated previous reports of specialized cellular functions such as production of *Il12b* in mCD103$^+$ cDC1[46] or *Ccl17* in CD11b$^+$ cDC2 and mLC [182]. Moreover, there was a general pattern of shared transcriptional identity within resident and migratory populations, which was further elucidated by performing DE analysis between migratory (clusters 0, 1, 2, 4 and 6) and resident (clusters 3 and 7) DC populations (**Figure S2.8E** and **Table 2.3**). Expression was largely uniform within migratory and resident DC, with enrichment of genes previously associated with migratory populations such as *Socs2* or *Fscn1* [46]*.*

Populations identified through unbiased clustering largely mirrored those identified using ImmGen-based criteria. However, of specific note, and in contrast to migratory cDC1, the canonical signature for migratory cDC2 applied to multiple clusters in our unbiased analysis. This indicated substantial and unresolved heterogeneity within this class of cDC. DE analysis between migratory CD11b$^+$ cDC2 clusters 0 and 4 identified the gene *Cd9*, a surface molecule, to be expressed specifically on cluster 0 (**Figure 2.1D** and **Table 2.4**). We determined that surface expression of CD9 parsed the two CD11b$^+$ cDC2 populations and with further investigation we found that expression was concordant with a previously identified molecule that distinguished cDC2 subsets, CD301b [183]. Within the migratory CD11b$^+$ cDC2 gate, CD9$^-$ cells were CD301b$^-$ (mCD301b$^-$), whereas CD9$^+$ cells were found to be CD301b$^+$ (mCD301b$^+$) (**Figure 2.1D**

and S2.8F). Due to the robustness of staining and parity with existing literature, CD301b was thus used for subsequent parsing of $CD11b^+$ cDC2 populations.

CD301b expression is often attributed to cells of monocyte/macrophage lineage and so we assessed expression of other monocyte/macrophage-related molecules on $mCD301b^-$ and $mCD301b^+$. While both $mCD301b^-$ and $mCD301b^+$ cells expressed CD135/FLT3 and SIRPα, consistent with cDC2 assignment [46], $mCD301b^+$ expressed higher surface levels of markers generally associated with cells of a monocyte/macrophage lineage [21], including CD14 (which we find later useful for parsing human cDC2 populations), CD16/32 (FcgRIII/II), CD200R and CD206 (**Figure S2.8G**). Despite these markers being associated with cells of macrophage lineage, $CD11b^+$ cDC2 are phenotypically DC, based on expression of *Zbtb46* [184,185] (**Figure S2.8H**).

With the assistance of unbiased scRNA-seq on bulk myeloid cells from the tdLN, we were able to derive a flow cytometry panel that encompasses this heterogeneity (**Figure 2.1E**). With this comprehensive delineation of major myeloid populations within the tdLN, we next sought to identify the exact APC(s) responsible for anti-tumor $CD4^+$ T_{conv} priming by using the markers to track, isolate or genetically deplete distinct populations.

Requisite Migration of tdLN Populations

Previous work has highlighted the importance of CD103$^+$ cDC1 migration to the tdLN for productive antitumor CD8$^+$ T cell responses [47]. Less is known, however, about CD11b$^+$ cDC2 migration from the tumor and we sought to identify whether these two cDC2 populations were tumor-originating and tumor-antigen bearing. Consistent with our scRNA-seq analysis, populations identified as migratory were found to express surface CCR7 within the tdLN (**Figure S2.8I**), consistent with previous migration from a peripheral tissue.

We then assessed the levels of tumor antigen within myeloid cells of tdLN from B16-ZsGreen (B16^{ZsGr}) tumor-bearing animals (**Figure 2.1F**) and found that mCD103$^+$, mCD301b$^-$ and mCD301b$^+$ were the most dominant ZsGreen$^+$ migratory populations, while resident populations generally had lower and heterogeneous levels of uptake, consistent with previous findings [47]. Notably, CD301b$^-$ and CD301b$^+$ cDC2 are also present within the TME with fractions of both populations expressing CCR7 (**Figure S2.8J**), indicating their migratory capacity and providing confirmation of the abundant ZsGreen tumor antigen detected in these populations within the tdLN. We then generated B16-mCherry-OVA (B16^{ChOVA}) tumor-bearing *Ccr7-/-* mice, and confirmed that these lacked normal frequencies of all migratory DC in the tdLN (**Figure S2.9A**). Furthermore, in this context, adoptively transferred CD4$^+$ OT-II T cells were nearly completely unable to initiate proliferation (**Figure S2.9B**). This confirmed that migratory DC populations were critical but did not identify which cell population(s) could directly present antigens to drive proliferation nor how these populations would induce CD4$^+$ T_{conv} differentiation.

De novo priming of CD4$^+$ T_{conv} by cDC2 in the tdLN

Using mice bearing B16^{ChOVA} tumors, we sorted each of the identified tdLN myeloid populations, each of which contained *in vivo* acquired and processed tumor antigen, and co-cultured them *ex vivo* with naïve CD4$^+$ OT-II T cells. This demonstrated that migratory CD11b$^+$ cDC2, whether they be mCD301b$^-$ or mCD301b$^+$, supported CD4$^+$ OT-II T cell expansion based on absolute cell number (**Figure 2.2A**) and frequency of cells undergoing cell division (**Figure 2.2B**). Importantly, despite similar antigen loading (**Figure 2.1F**), rCD11b$^+$ induced little proliferation of OT-II cells. Addition of exogenous OT-II OVA peptide ($OVA_{323-339}$) resulted in comparable activation and proliferation across myeloid populations, indicating that other populations are viable and otherwise capable of engaging CD4$^+$ T_{conv}, but likely simply do not process and present tumor antigen on MHC-II, restricting their ability to prime CD4$^+$ T_{conv} (**Figure 2.2C, 2.2D**).

To extend this study *in vivo*, we next tested whether CD11b$^+$ cDC2 were required for initiating CD4$^+$ T_{conv} priming within the tdLN. Mice lacking *Irf4* in DC have been shown to lack LN cDC2 [179], however use of *Irf4$^{flox/flox}$Itgax^{Cre}* resulted in consistent spontaneous germline deficiency (data not shown), complicating our efforts to delete *Irf4* specifically in the myeloid compartment. We instead used globally deficient *Irf4$^{\Delta/\Delta}$* (*Irf4$^{flox/flox}$ActB^{Cre}*) B16^{ChOVA}-tumor-bearing animals, with adoptively transferred wild-type OT-II T cells, wherein we observed a reduction of all migratory cDC2 populations in the tdLN (**Figure 2.2E**). Transferred OT-II cells in *Irf4$^{\Delta/\Delta}$ mice* failed to proliferate as assessed by dye dilution and similarly failed to accumulate in the tdLN (**Figure 2.2F**). In contrast, in *Xcr1^{DTR}* mice, depletion of mCD103$^+$ and rCD8α^+ did not impact OT-II

proliferation (**Figure 2.9C, 2.9D**). By exploiting differential expression of *Cx3cr1* in rCD11b$^+$ (**Table 2.2**), we generated *Cx3cr1*$^{lsl\text{-}DTR}$*CD11c*^{Cre} animals that allowed for specific depletion of rCD11b$^+$ following DT administration **(Figure S2.9E**). Consistent with our *in vitro* findings, depletion of rCD11b$^+$ did not reduce OT-II proliferation (**Figure 2.9F**). Both *in vitro and in vivo*, migratory CD11b$^+$ cDC2, but not other cDC populations, were found to be the primary inducers of antitumoral CD4$^+$ T_{conv} priming.

Tolerogenic CD4$^+$ T_{conv} priming in the tdLN

In our tumor-bearing mice, effective anti-tumor immunity is not occurring despite evident initiation of CD4$^+$ T_{conv} priming and we hypothesized that CD4$^+$ T_{conv} differentiation by the identified cDC2 might not be generating effector differentiation. To examine this, we directly compared *in vivo* activation and differentiation of adoptively transferred OT-II T cells in the context of anti-tumor priming (tdLN^{B16ChOVA}) with tolerance-inducing priming via injection of adjuvant-free antigen (endoOVA) and with robust effector CD4$^+$ T_{conv} priming via infection by an influenza virus (X31^{pOVA}). We found that CD69 expression on OT-II at day 3, representing a marker of the strength of T cell activation [186] and/or exposure to inflammatory cytokines [187,188], was similar in tdLN^{B16ChOVA} and tolerizing endoOVA and much lower as compared to inflammatory priming with X31^{pOVA} (**Figure 2.2G**). Correspondingly, other markers of activation observed in robust X31^{pOVA} activation, namely CD44 upregulation and CD62L downregulation, were not observed to the same extent on the tdLN^{B16ChOVA} OT-II T cells, which were largely similar to those primed by endoOVA (**Figure 2.2H, 2.2I**).

Finally, we found minimal downstream differentiation toward a protective ICOS^{hi} PD-1^{lo} T_h1 surface phenotype in both tdLN^{B16ChOVA} and endoOVA conditions when examined day 7 post-transfer, compared to X31 ^{pOVA} (**Figure 2.2J**). This also coincided with little to no cytokine production, notably IFNγ, following restimulation (**Figure 2.2K)**. While we found that cDC2 initiate CD4$^+$ T_{conv} priming in the tdLN, such defective effector T_{conv} differentiation predicts that therapeutic improvement of CD4$^+$ T_{conv} priming might either function through alterations in cDC2 phenotype, or via the licensing of other cell types to become APCs for CD4$^+$ T_{conv}.

Concommittant expansion of T_{reg} and CD11b$^+$ cDC2 in the TME

While examining the expansion of cDC2 in the TME of tumors with variable proportions of tumor cells secreting GM-CSF (B16$^{Gm\text{-}csf}$) [18], we found the surprising result that CD4$^+$ T_{conv} numbers did not rise appreciably with the induced increase in CD11b$^+$ cDC2 (considering both CD301b$^-$ and CD301b$^+$ cDC2 subsets) (**Figure 2.3A, 2.10A).** Given that these populations clearly express epitopes on MHC-II to CD4$^+$ T cells (**Figure 2.2**), we hypothesized that T_{reg} may prefentially expand in response to CD11b$^+$ cDC2 and may act as a feedback mechanism to suppress CD11b$^+$ cDC2 function and thus effective antitumor CD4$^+$ T_{conv} priming. Analyzing the same mice for T_{reg} proportion we found, indeed, a positive correlation between T_{reg} frequencies in the TME and cDC2 number. Given previous data suggesting that general DC may be altered or deleted by T_{reg} [173], we sought to test whether T_{reg} might be restricting the trafficking and/or phenotype of CD11b$^+$ cDC2, thereby generating poorly differentiated CD4$^+$ T_{conv}.

Therapeutic benefits of T_{reg} depletion rely on *de novo* $CD4^+$ T_{conv} priming

Diptheria Toxin treatment of *Foxp3*^{DTR} mice (Kim et al., 2007) led to robust acute T_{reg} depletion and potent tumor rejection which required $CD4^+$ T_{conv} as previously described [87] (**Figure 2.3B, 2.3C and 2.10B**). To examine the role of of tdLN $CD4^+$ T_{conv} priming specifically, we tested whether rejection depended on reactivation of $CD4^+$ T_{conv} already present in the TME or expansion and infiltration of recently activated $CD4^+$ T_{conv}. For this, we employed the use of the S1PR antagonist, FTY720, to block $CD4^+$ T_{conv} egress from the tdLN [189]. While FTY720 treatment had little effect on tumor growth in progressing tumors, FTY720/DT-treated *Foxp3*^{DTR} mice were unable to reject tumors in contrast to their DT-treated *Foxp3*^{DTR} controls (**Figure 2.3D**), demonstrating $CD4^+$ T_{conv} tdLN priming and egress is required for tumor rejection following T_{reg} depletion.

T_{reg} depletion induces enhancement of both $CD11b^+$ cDC2 and $CD4^+$ T_{conv}

Transfer of $CD4^+$ OT-II into B16^{ChOVA} tumor-bearing T_{reg}-depleted animals led to greatly enhanced proliferation and expansion of OT-II in the tdLN at day 3 post-transfer compared to control (**Figure 2.3E**)**.** Enhanced $CD4^+$ T_{conv} proliferation led us to hypothesize that T_{reg} depletion relieved suppression of the $CD11b^+$ cDC2/$CD4^+$ T_{conv} axis in the TME and tdLN. To test this, we first examined antigen trafficking to the tdLN following T_{reg} depletion in B16^{ZsGr} tumor-bearing control and *Foxp3*^{DTR} mice. Following T_{reg} depletion, ZsGreen$^+$ mCD301b$^-$ and mCD301b$^+$ were greatly increased in absolute number in the tdLN, while other migratory populations were only weakly increased or unchanged (**Figure 2.3F**). This rise depended upon chemokine-mediated tumor to tdLN trafficking as treating mice with pertussis toxin (PTX), which blocks $G\alpha_i$ signaling,

blocked the rise in cDC2 in the T_{reg} deplete condition to a similar degree as the non-depleted controls (**Figure 2.10C**). By analyzing changes in the abundance of $CD11b^+$ cDC2 in the tdLN over time following T_{reg} depletion (**Figure 2.3G**), we were also able to determine that the wave of enhanced $CD11b^+$ cDC2 migration temporally coincided with increases in the poorly-upregulated activation markers identified in **Figure 2** (CD69 and CD44 (**Figure 2.3H**) consistent with a model in which a new wave of cDC2 carried the capacity to upregulate the quality of priming.

In order to test whether APC populations that trafficked to the tdLN in the absence of T_{reg} were capable of priming $CD4^+$ T_{conv}, we co-cultured each APC isolated from *Foxp3*^{DTR} tdLN with $CD4^+$ OT-II *in vitro* and measured their proliferation. This demonstrated that $mCD301b^-$ and $mCD301b^+$ remained the only cells capable of supporting T cell division and accumulation (**Figure 2.4A, 2.4B**), while other cells were still only able to prime CD4 T cells if provided exogenous antigen (**Figure 2.11A**). Furthermore, by crossing *Xcr1*^{DTR} with *Foxp3*^{DTR}, we were able to genetically exclude that neither $mCD103^+$ nor $rCD8\alpha^+$ were now required for improved $CD4^+$ T_{conv} priming and tumor rejection following T_{reg} depletion (**Fig 2.11B , 2.11C**).

To then determine whether $CD11b^+$ cDC2 generated in the absence of T_{reg}, enhanced the quality of the priming reaction, we measured augmentation of CD69 expression on divided OT-II co-cultured with $CD11b^+$ cDC2 *in vitro* (**Figure 2.4C**), and on divided OT-II transferred *in vivo* (**Figure 2.11D).** In both settings we found that, similar to $CD4^+$ T_{conv} response in influenza (**Figure 2**), primed OT-II exhibited increased expression of CD69 compared to control tdLN conditions.

To directly measure the change in phenotype of CD11b^{+} cDC2 in the absence of T_{reg}, we examined transcriptional changes in bulk myeloid cells from *Foxp3^{DTR}* tdLN with scRNA-seq. This confirmed normal representation of myeloid populations within the *Foxp3^{DTR}* tdLN (**Figure S4E**) and comparable UMI within each cluster (**Figure S4F**). When tdLN and *Foxp3^{DTR}* tdLN data was aggregated, myeloid cells from both samples co-clustered, indicating that the transcripts defining basic cellular identity remain similar to one another following T_{reg} depletion (**Figure S4G**). However, when we performed DE analysis on mCD301b^{-} and mCD301b^{+} cells between tdLN and *Foxp3^{DTR}* tdLN conditions, we found pronounced increases in costimulatory genes (*Cd80*, *Cd86*), genes involved in T cell chemoattraction (*Ccl17, Ccl22*) and genes expressed in response to pro-inflammatory cytokines (*Stat1, Stat4*) (**Figure 4D** and **Supplementary Table 5**). The increase in expression of both *Cd80* and *Cd86* was also verified by flow cytometry (**Figure 4E**), confirming not only our transcriptional data, but also the hypothesis that T_{reg} regulate mCD301b$^{-/+}$ functional phenotype.

We next assessed whether enhanced CD11b^{+} cDC2 functionality coincided with improved CD4^{+} T cell differentiation *in vivo*. We observed profound increases in CD44^{+} ICOS^{hi} PD-1^{lo} T_h1-like cells in the tdLN following T_{reg} depletion, similar to the cells found following X31^{pOVA} (**Figure 2, Figure 4F**). Changes in the tdLN coincided with increases in effector CD4^{+} T_{conv} populations within the TME as well (**Figure 4G**).

To confim that the increase in T_h1-like cells in the tumor was due to enhanced *de novo* priming and differentiation, we again treated tumor-bearing control and *Foxp3^{DTR}* mice with DT and FTY720 and analyzed immune composition in both tdLN and TME. In the tdLN, FTY720 treatment had minimal impact in control mice but led to significant

increases of T_h1-like cells in *Foxp3*^{DTR} tdLN. (**Figure 4H**). In contrast, the proportion of T_h1-like CD4$^+$ T_{conv} dropped precipitously in the TME of *Foxp3*^{DTR} mice following FTY720 treatment (**Figure 4I**), indicating that the increased T_h1-like CD4$^+$ T_{conv} observed in the TME was due to enhanced *de novo* priming and subsequent tumor infiltration.

GVAX/anti-CTLA-4 therapy function together to induce expansion and functional enhancement of CD11b$^+$ cDC2

We hypothesized that combination GVAX (irradiated B16$^{Gm\text{-}csf}$) and anti-CTLA-4 therapy potentiates CD4$^+$ T_{conv} immunity through concurrent expansion of CD11b$^+$ cDC2 and release of their suppression through T_{reg} depletion at the vaccine site. To assess this, we compared the immune composition of the vaccine site between BVAX (irradiated B16-F10) +/- anti-CTLA-4 and GVAX +/- anti-CTLA-4. In either GVAX condition, we observed significant increases of both CD11b$^+$ cDC2 subsets (**Figure 5A**), but anti-CTLA-4 treatment led to a reduction in T_{reg} and expansion of CD4$^+$ $T_{conv.}$ (**Figure 5B**). We found that GVAX/anti-CTLA-4 functionally enhances CD11b$^+$ cDC2 as expression of both CD80 and CD86 on mCD301b$^-$ within the vaccine-draining LN (vaxLN) were most improved following combination GVAX/anti-CTLA-4, whereas mCD301b$^+$ benefitted primarily from GVAX alone (**Figure 5C**), indicating that perhaps T_{reg} more specifically suppress CD301b$^-$ cDC2. When we compared tumor growth between BVAX +/- anti-CTLA-4 and GVAX +/- anti-CTLA-4 we observed that BVAX alone or in combination with anti-CTLA-4 was ineffective at inducing robust antitumor immunity. In contrast, GVAX combined with anti-CTLA-4 lead to a profound reduction in

tumor growth rates during the course of the experiment (**Figure 5D**). To assess CD11b$^+$ cDC2 depedency for CD4$^+$ T_{conv} priming against tumor vaccine antigen, we analyzed cDC composition in the vaccine site and vaxLN of control and *Irf4*$^{\Delta/\Delta}$ mice treated with anti-CTLA-4 and a combination of GVAX and irradiated B16^{ChOVA}. Similar to tumor-bearing animals, loss of *Irf4* greatly reduced the presence of CD11b$^+$ cDC2 in either site (**Figure 5E**), which corresponded to a near complete loss of CD4$^+$ OT-II proliferation in the vaxLN (**Figure 5F**). Taken together, these data along with our prior findings indicate that CD11b$^+$ cDC2 are active targets of T_{reg}-mediated suppression and are central to the initiation of CD4$^+$ T_{conv} antitumor immunity following therapeutic intervention.

scRNA-seq of the human tdLN reveals similar heterogeneity within cDC2 subset between mouse and human.

Recent scRNA-seq on normal human blood has highlighted heterogeneity within human cDC2 (here defined by CD1c$^+$/BDCA-1$^+$) [54], although the existence of these populations within the human tdLN has not been assessed in an unbiased manner. To determine whether human tdLN had similar populations and heterogeneity to that of mouse and human blood, we performed scRNA-seq on myeloid populations isolated from a patient's melanoma-draining LN. Following removal of non-APC cellular contaminants, we observed 7 unique clusters from 1,710 input cells (**Figure 6A**). Using DE and gene overlays, we were able to establish expressing cDC1 (hereby referred to as BDCA-3$^+$ cDC1) occupied cluster 5 and CD1C expressing cDC2 (hereby referred to as BDCA-1$^+$ cDC2) occupied cluster 0. The panel of genes expressed on cluster 0 and 5 were very similar to those identified previously for BDCA-1$^+$ cDC2 and BDCA-3$^+$ cDC1

[54], respectively, serving as confirmation of our initial identification (**Figure 6B, S5A, Supplementary Table 6**). To assess additional hetereogeneity within BDCA-1$^+$ cDC2, we reclustered BDCA-1$^+$ cDC2/cluster 0 and identified 3 populations (**Figure 6C**) that were transcriptionally distinct based on DE analysis (**Figure 6D, 6E and Supplementary Table 7**). Cluster 0.2 expressed high levels of CD1E, SLAMF7 and HLA-DQB2, genes that had been identified on a subset of blood cDC2 previously [54]. Cluster 0.3, similar to mCD301b$^+$ cDC2 in mouse, expressed genes often associated with cells of a monocyte/macrophage lineage, including CD14, VCAN and S100A8 and like cluster 0.2, resembled a previously identified cDC2 population [54]. Cluster 0.1 was unique in that it was enriched for genes associated with cell motility (CORO1A, CRIP1, SEPT6, ANXA6) and may represent cellular status opposed to a *bona fide* distinct cellular population (**Figure 6D**). We found that in addition to their presence within the human tdLN, CD14$^-$ BDCA-1$^+$ cDC2 and CD14$^+$ BDCA-1$^+$ cDC2 were present within the TME of a human head and neck squamous cell carcinoma (HNSC) tumor and both expressed CCR7, indicating their migratory potential (**Figure 6F**). While previously identified in blood, our data suggest that cDC2 subsets in human tdLN or TME have similar characteristics to mouse cDC2 subsets, though it remains a possibility that further heterogeneity still exists within this compartment in humans, particularly across individuals.

Parsing the predictive nature of BDCA-1$^+$ cDC2 in the human TME

The results of our mouse models have specific predictions about the functional outcomes based on intratumoral cellular abundance. Data from **Figure 3** and **Figure 5**

predict that CD4$^+$ T_{conv} quantity and quality will vary with intatumoral cDC2 and T_{reg} density. To assess this, we obtained 32 primary tumors from the head and neck region, a tumor type known to be rich in T_{reg} [190], and analyzed their immune composition with two independent flow cytometry panels (**Figure 6F, S6A**). In plots of BDCA-1$^+$ cDC2 and T_{reg} frequencies, we found three distinct patient TME with varied abundance of BDCA-1$^+$ cDC2 or T_{reg} (**Figure 7A**). As predicted from the mouse models, patient TME with low representation of BDCA-1$^+$ cDC2 demonstrated the lowest level of CD4$^+$ T_{conv} infiltration (**Figure 7B**). Consistent with T_{reg} suppressing CD4$^+$ T_{conv} immunity through BDCA-1$^+$ cDC2, patients that were BDCA-1$^+$ cDC2^{HIGH}/Treg^{LOW} had greater CD4$^+$ T_{conv} infiltration than patients with BDCA-1$^+$ cDC2^{HIGH}/T_{reg}^{HIGH}. To ensure that differences in CD4$^+$ T_{conv} were not merely due to a proportional shift, we analyzed CD8$^+$ T cell frequencies which we found to vary independently to either T_{reg} or CD4$^+$ T_{conv} frequency (**Figure S6B**).

Beyond total numbers, our model predicts improvements in ICOS^{hi} PD-1^{lo}CD4$^+$ T_{conv} phenotype would align with specific densities of BDCA-1$^+$ cDC2 and $T_{reg.}$ Patients whose biopsies (TME) were low for both BDCA-1$^+$ cDC2 and T_{reg} had CD4$^+$ T_{conv} that lacked ICOS but expressed high levels of PD-1 while CD4$^+$ T_{conv} from tumors with high BDCA-1$^+$ cDC2 and high T_{reg} had high PD-1 as well, though expressed intermediate amounts of ICOS, perhaps reflective of cells seen previously [172] (**Figure 7C)**. In contrast, CD4$^+$ T_{conv} from TME with abundant BDCA-1$^+$ DC and low T_{reg} frequencies had significantly higher surface expression of ICOS, paired with decreased PD-1 (**Figure 7C, S6C, S6D**). While cancer staging at the time of analysis was fairly similar across classes of TME (**Figure 7D**), progression-free survival was significantly better in

patients whose TME had abundant in BDCA-1$^+$ cDC2 and low T_{reg} than either of the other two TME classes (**Figure 7E**). Together these data suggest that the content of immune infiltrate informs not only the quality of an immune response (PD-1^{lo}ICOS$^+$ CD4$^+$ T_{conv}) but also the capacity of antitumor immunity (progression-free survival).

The presence of high BDCA-3$^+$ cDC1 and NK cells within the melanoma (SKCM) TME has been described as a general prognostic indicator of anti-PD-1 responsiveness [191], presumably due to their profoundly better ability to prime CD8$^+$ T cells. However, in that study, we also identified patients with higher densities of CD4$^+$ T_{conv} amongst responders and these did not have higher densities of cDC1. We reasoned that perhaps those responders were primed for CD4$^+$ T_{conv} immunity and that this might instead rely upon cDC2. To thus assess whether BDCA-1$^+$ cDC2 could also contribute to anti-PD-1 responsiveness, we re-gated flow cytometry data from patient biopsies to reflect the recent heterogeneity identified within BDCA-1$^+$ cDC2. The frequency of BDCA-3$^+$ cDC1 and BDCA-1$^+$ cDC2 (both CD14$^{-/+}$) of HLA-DR were plotted (**Figure 7F**). Non-responder TME were generally lower for DC of both subtypes (**Figure S6E**). Responder TME were then divided based on the abundance of either BDCA-3$^+$ cDC1 or BDCA-1$^+$ cDC2. We found that responders high for BDCA-1$^+$ cDC2, compared to responders high for BDCA-3$^+$ cDC1 had a significantly lower proportion of CD8$^+$ T cells but significantly higher CD4$^+$ T_{conv} within their TME (**Figure 7G**), promoting the hypothesis that these patients have improved CD4$^+$ T_{conv} activity even with lower overall CD8$^+$ T cell abundance. We reasoned that BDCA-1$^+$ cDC2 abundance alone may predict CD4$^+$ T_{conv} quantity in melanoma (SKCM), as proportions of T_{reg} were significantly lower than in HNSC. (**Figure 7H**). These data suggest that classes of human TME can be divided based on

the abundance of BDCA-1$^+$ cDC2 and that this can be an indicator for both CD4$^+$ T_{conv} quality and represent patients likely to respond to ICB.

III. DISCUSSION

Here, we define the cell type(s) necessary for *de novo* priming of new antitumor $CD4^+$ T_{conv}. A fundamental conclusion is that MHC-II presentation of peptides to prime new $CD4^+$ T_{conv} is heavily biased to $CD11b^+$ cDC2, with the distinction between tumor control and tumor tolerance being determined by the phenotype of these cells. $CD4^+$ T_{conv} priming in tdLN most resembles that of non-inflamed lymph nodes, where $CD4^+$ $T_{conv\ are}$ generated with a depressed activation state, with little or no evidence of the $CD44^+PD\text{-}1^{lo}ICOS^+$ phenotype (**Figure 2**). While the TME may futher drive exhaustion, this conclusion suggests that efficacy of immunotherapies for $CD4^+$ T_{conv} will rely on modulation of this defective step of priming. Indeed, given the apparent irreversibility of certain forms of exhaustion [65], it is possible that the efficacy of ICB is linked to ongoing *de novo* lymph node priming rather than only blockade of checkpoint ligands in the tumor.

Our scRNA-seq and functional data demonstrate that two distinct populations of IRF4-dependent $CD11b^+$ cDC2 – for which we found homologs in human tdLN and TME – are required *in vivo* for initiating activation of antitumor $CD4^+$ T_{conv}. The complement of myeloid cells identified in mouse tdLN are consistent with previous reports [48,192,193], however, our approach assayed all populations in parallel allowing for unambiguous confirmation of $CD4^+$ T_{conv} stimulatory function. While our data suggest $mCD301b^-$ and $mCD301b^+$ play largely redundant roles in antitumor immunity, as each population was capable of supporting comparable OT-II proliferation *ex vivo* and collectively *in vivo* (Figure 2), we cannot exclude the possibility that these cell populations have disparate functions in other tumor models or following different treatments. cDC2 have been

previously associated with $CD4^+$ T_{conv} priming, with $CD301b^+$ cDC2 being shown to specifically induce T_h2 responses to adjuvant [194] and a second report suggesting that pan-cDC2 population in tumor was demonstrated to induce T_h17 differentiation primarily *in vitro* [55]. However, our findings specifically document suboptimal triggering of early activation (e.g. CD69, CD44 levels) as well as poor induction of differentiation in OT-II from tdLN and non-inflammed LN compared to inflammatory conditions such as influenza or Treg-depletion (**Figure 2**). Previous work has identified an IFNγ-dependent homeostatic 200 gene program associated with poor DC:T cell priming, some of which are co-opted in tumors [195]. We also found expression of some of these genes in tdLN mDC (e.g. *Socs2, Fscn1)* (**Figure 1**) and were able to further define a functional readout for phenotypic defects in $CD11b^+$ cDC2. Whether expression of these genes is associated with defects in $CD4^+$ T_{conv} differentiation is unclear, although these data support a homeostatic phenotypic dampening of cDC function, in particular cDC2, that can be reverted during specific inflammatory settings.

Therapeutic depletion of T_{reg} enhanced cDC2 migration and reverted phenotypic dysfunction, which in turn allowed productive antitumor $CD4^+$ T_{conv} priming to occur in the tdLN. Previous studies have demonstrated reactivated $CD4^+$ T_{conv} immunity following T_{reg}-depletion [87,196], although the mechanism through which reactivation occured was unclear. While we cannot preclude the possibility that T_{reg} suppress $CD4^+$ T_{conv} directly [197] or impact DC more generally [89,173], our data demonstrates a potetently immunosuppressive relationship between T_{reg} and $CD11b^+$ cDC2. Expansion of $CD11b^+$ cDC2, in either the TME (**Figure 3**) or GVAX site (**Figure 5**), induces concurrent increases in T_{reg} which likely represents that cDC2 produced under these conditions

undergo continued suppression, opposing their ability to drive productive effector $CD4^+$ T_{conv}. This is consistent with data from others showing T_{reg} require MHC-II on DC to expand in the periphery [198].

Phenotypically enhanced $CD11b^+$ cDC2 were better able to support $CD4^+$ T_{conv} priming and support improved differentiation to a PD-1^{lo} $ICOS^+$ T_h1-like phenotype (**Figure 3**, **Figure 4**). Although $CD103^+$ cDC1 have been shown to induce T_h1 immunity in specific inflammatory settings [199], they were dispensible for tumor rejection following T_{reg} depletion, supporting our data demonstrating that $CD11b^+$ cDC2 are uniquely able to initiate productive antitumor $CD4^+$ T_{conv} priming in the absence of T_{reg} (**Figure 4**). Efficacious anti-CTLA-4 treatment in both mouse and human is associated with the generation of PD-$1^{lo}$$ICOS^+$ T_h1-like systemically [171,200], although the site of this population's initial emergence was previously undefined. We found that antitumor PD-$1^{lo}$$ICOS^+$ $CD4^+$ T_{conv} arise in tdLN during *de novo* priming and additionally that infiltration of these tdLN-derived antitumor $CD4^+$ T_{conv}, as opposed to via local reactivation in the TME, was the dominant mechanism through which tumor rejection occurred (**Figure 3**, **Figure 4**). Together, this inserts cDC2 as the mechanistic intermediate between certain therapeutic interventions and enhanced $CD4^+$ T_{conv} priming and also highlights the importance of enhancing cDC2 phenotype in patients in order to improve distal priming for more effective immunotherapy.

In human HNSC TME, we found a remarkable concordance with our T_{reg} depletion data whereby heterogeneity in T_{reg} and cDC2 abundance parsed subsets of patients with distinct phenotypes and, in particular, the relationship between BDCA-1^+ cDC2 and T_{reg} informed both the quantity and character of $CD4^+$ T_{conv}. This parallel with

our data in mouse strongly suggests that a similar mechanism of T_{reg}-mediated suppression exists in human. The use of T_{reg} alone as a prognostic indicator has varying levels of predictive power [201] and this may in part be due to the fact tha low T_{reg} abundance fails to differentiate cohorts that have or do not have requisite cDC2 populations for $CD4^+$ T_{conv} priming. Our pairing of T_{reg} abundance with the additional parameter (BDCA-1^+ cDC2) unmasks hetereogeneity of TME, allowing for significant predictions of immune response quality and disease-free survival (**Figure 7**). Looking forward, this suggests that BDCA-1^+ DC abundance is a biomarker for a primed microenvironment for response to ICB or to novel therapies targeting T_{reg} suppression of cDC2. Indeed, a human TME dataset of anti-PD-1 responder/non-responders demonstrated that while BDCA-3^+ cDC1 cellularity is largely associated with anti-PD-1 responsiveness [191], some patients were surprisingly BDCA-3^+ cDC1 low, but contained higher proportions of BDCA-1^+ cDC2 and $CD4^+$ T_{conv}, suggesting that at least in some TME, such as those with tumor cells that express MHC-II [170], $CD4^+$ T_{conv} may be capable of playing a preeminent role in successful antitumor responses.

Taken together, our work highlights $CD11b^+$ cDC2/BDCA-1^+ cDC2 as a target of T_{reg} suppression and as a necessary population for directing antitumor $CD4^+$ T_{conv} immunity. Furthermore, cDC2 abundance in the human TME may act as a biomarker for not only $CD4^+$ T_{conv} quality but also as a contributing indicator for responsiveness to ICB. Classifying TME based on immune infiltrate has predictive power [202] and thus recent [156,203,204] and future efforts to characterize disparate TME with unbiased high-dimensional techniques will undoubtable prove invaluable for identifying unique classes

of patient TME that are profoundly immunosuppressed or poised for therapeutic response.

IV. MATERIALS AND METHODS

See **Table 2.8** for a list of reagents, biological samples and software used in these experiments.

Human Tumor Samples

The human head and neck tumor set consisted of a total of 32 tumors removed from the head and neck region, agnostic to location. The anti-PD-1 responder/non-responder melanoma tumor set was published previously [205]. All patients consented for tissue collection under a UCSF IRB approved protocol (UCSF IRB# 13-12246 and 14-15342). Samples were obtained after surgical excision with biopsies taken by the Pathology Department to confirm the presence of tumor cells. Patients were selected without regard to prior treatment. Freshly resected samples were placed in ice-cold PBS or Leibovitz's L-15 medium in a 50 mL conical tube and immediately transported to the laboratory for evaluation. Patient samples were coded and flow analysis was scored by separate individuals prior to data agglomeration. All samples were processed and analyzed by flow cytometry, but only those with at least 1,000 live $CD45^+$ cell events were included in the analysis.

Mice

All mice were treated in accordance with the regulatory standards of the National Institutes of Health and American Association of Laboratory Animal Care and were approved by the UCSF Institution of Animal Care and Use Committee. The following mice were purchased for acute use or maintained under specific pathogen-free conditions at the University of California, San Francisco Animal Barrier Facility. We

attempted to use *Irf4*$^{flox/flox}$;*CD11c-Cre* but discovered independent breeding cages were producing germline *Irf4* globally deficient pups, complicating our findings (data not shown).

Tumor cell lines, tumor cell injections and tumor growth experiments

B16-F10 (ATCC, CRL-6475) was purchased. B16-ChOVA (B16^{ChOVA}), a derivative of B16-F10, was created through transduction of B16-F10 with an mCherry-OVA (ChOVA) fusion construct identical to that used in previous studies in our lab [47,206]. B78^{ChOVA}, derived from the parental B78 subline of B16, was generated in our laboratory and described previously [18]. B16-ZsGreen (B16^{ZsGr}) was previously generated in our laboratory as described [14]. B16^{GM-CSF} (GVAX) [207] were acquired from the laboratory of Dr. Lawrence Fong at UC San Francisco. Adherent cell lines were cultured at 37°C in 5% CO_2 in DMEM (Invitrogen), 10% FCS (Benchmark), Pen/Strep/Glut (Invitrogen).

For tumor cell injection, adherent tumor cells were lifted using 0.05% Trypsin-EDTA (Thermo Fisher Scientific) and washed 3X with DPBS (Thermo Fisher Scientific). $1.0x10^5$ – $2.5x10^5$ tumor cells were resuspended in DPBS and mixed 1:1 with Matrigel GFR (Corning) for a final injection volume of 50 μL. Mice anesthetized with isoflurane (Henry Schein) were shaved on their flank and injected subcutaneously either unilaterally or bilaterally depending on the experimental setup.

For tumor measurements, tumors were typically measured 3 times per week using electronic calipers. Tumor volume was calculated through the formula $V = 0.5(w^2$

x *l*). Mice were removed from the study and euthanized when tumors exceeded a volume of 1000 mm^3.

Single Cell RNA Sequencing (scRNA-Seq)

For mouse scRNA-seq, live $CD90.2^-$ $B220^-$ $Ly6G^-$ $NK1.1^-CD11b^+$ and/or $CD11c^+$ cells were sorted from inguinal and axillary LN with a BD FACSAria Fusion. For human scRNA-seq, live $CD3^-CD19/20^-CD56^-$ cells were sorted from a melanoma-draining LN on a BD FACSAria Fusion. After sorting, cells were pelleted and resuspended at $1x10^3$ cells/μl in 0.04%BSA/PBA and loaded onto the Chromium Controller (10X Genomics). Samples were processed for single-cell encapsulation and cDNA library generation using the Chromium Single Cell 3' v2 Reagent Kits (10X Genomics). The library was subsequently sequenced on an Illumina HiSeq 4000 (Illumina).

Single Cell Data Processing

Sequencing data was processed using 10X Genomics Cell Ranger V1.2 pipeline. The Cell Ranger subroutine *mkfastq* converted raw, Illumina bcl files to fastqs which were then passed to Cell Ranger's *count,* which aligned all reads using the aligner STAR [208] against UCSC mm10 or GRCh38 genomes for mouse and human cells, respectively. After filtering reads with redundant unique molecular identifiers (UMI), *count* generated a final gene-cellular barcode matrix. Both *mkfastq* and *count* were run with default parameters.

Cellular Identification and Clustering

For each sample, the gene - barcode matrix was passed to the R (v. 3.4.3) software package Seurat [209] (http://satijalab.org/seurat) (v2.3.0) for all downstream analyses. We then filtered on cells that expressed a minimum of 200 genes and required that all genes be expressed in at least 3 cells. We also removed cells that contained > 5% reads associated with cell cycle genes [210,211]. Count data was then log2 transformed and scaled using each cell's proportion of cell cycle genes as a nuisance factor (implemented in Seurat's *ScaleData* function) to correct for any remaining cell cycle effect in downstream clustering and differential expression analyses. For each sample, principal component (PC) analysis was performed on a set of highly variable genes defined by Seurat's *FindVariableGenes* function. Genes associated with the resulting PCs (chosen by visual inspection of scree plots) were then used for graph-based cluster identification and subsequent dimensionality reduction using t-distributed stochastic neighbor embedding (tSNE). Cluster-based marker identification and differential expression were performed using Seurat's *FindAllMarkers* for all between-cluster comparisons.

ImmGen Signature Generation

To generate *a priori* signatures for the myeloid cell types that we expected to find in the mouse tdLN sample, we downloaded microarray based transcriptional profiles from the Immunological Genome Project data Phase 1[180] (GSE15907). See **Supplementary Table 1** for the specific samples used.

For each ImmGen population, we performed DE analysis comparing samples from the population of interest to the aggregate of the remaining 6 groups using the R

package *limma* [212]. We ordered the top 20 genes with the smallest FDR values [213] by fold change (excluding any genes that were downregulated in the group of interest) and then cross referenced the resulting list with the single cell expression matrix from each sample. This left genes that were both highly differentially expressed in the IMMGEN profiles and expressed in our single cell data sets of interest. The top 10 genes (or fewer if less than 10 genes remained) by fold change were then median normalized and aggregated to create a single "signature gene" for each cell type. These signature genes were 0-1 scaled and plotted in the context of the *t*-SNE dimensionality reduction to show cellular location.

Sequencing Sample Aggregation

In order to generate pairwise aggregations between samples and control for potential batch effects, we used Seurat's Canonical Correlation Analysis (CCA) functionality. All post-filtered cells from each of the single sample analyses were used in the aggregate. CCA was performed on the union of the 2000 genes with highest dispersions from each dataset. The number of canonical correlation vectors (CCVs) used in downstream clustering and *t*-SNE analyses was chosen by visual inspection of heatmaps of genes associated with those top CCVs. Results were robust to moderate changes in this final number of CCVs.

Mouse Tissue Digestion and Flow Staining

Tumor and LN tissues were harvested and enzymatically digested with 0.2 mg/ml DNAse I (Sigma-Aldrich), 100 U/ml Collagenase I (Worthington Biochemical), and 500

U/ml Collagenase Type IV (Worthington Biochemical) for 30-45 minutes at 37 °C. TdLN included inguinal and axillary LN. Tumor samples were subjected to consistent agitation during this time and LN samples were rapidly pipetted at the half-point time. Samples were filtered to generate a single-cell suspension and washed with stain media (PBS, 2% FCS).

Cells harvested from these tissues or *in vitro* culture were washed with PBS and stained with Zombie NIR fixable viability dye (BioLegend) for 30 minutes at 4°C to distinguish live and dead cells. Cells were then washed with stain media and non-specific binding was blocked with anti-CD16/32 (BioXCell), and 2% rat serum (Invitrogen) and 2% Armenian hamster serum (Innovative Research). Cell surface proteins were then stained on ice for 30 minutes. Cells were washed again and re-suspended with stain media prior to collection and analysis on a BD Fortesssa or LSR-II flow cytometer. When applicable, black latex beads were added to the sample for quantification of absolute cell number. For intracellular stains, cells were fixed and permeabilized with the FoxP3/Transcription Factor Staining Buffer Set (Thermo Fisher Scientific) after surface marker staining. Intracellular antibodies were stained in permeabilization buffer with 2% rat serum for at least 30 minutes at room temperature.

Human Tissue Digestion and Flow Staining

Tumor or LN tissue was thoroughly chopped with surgical scissors and transferred to GentleMACs C Tubes (Miltenyi Biotec) containing 20 uL/mL Liberase TL (5 mg/ml, Roche) and 50 U/ml DNAse I (Roche) in RPMI 1640 per 0.3 g tissue. GentleMACs C Tubes were then installed onto the GentleMACs Octo Dissociator

(Miltenyi Biotec) and incubated according to the manufacturer's instructions. Samples were then quenched with 10 mL of sort buffer (PBS/2% FCS/2mM EDTA), filtered through 100 um filters and spun down. Red blood cell lysis was performed with 175 mM ammonium chloride.

Cells were then incubated with Human FcX (Biolegend) to prevent non-specific antibody binding. Cells were then washed in DPBS and incubated with Zombie Aqua Fixable Viability Dye (Biolegend). Following viability dye, cells were washed with sort buffer and incubated with cell surface antibodies for 30 minutes on ice and subsequently fixed in either Fixation Buffer (BD Biosciences) or in Foxp3/Transcription Factor Staining Buffer Set (ThermoFisher Scientific) if intracellular staining was required.

APC-T cell *In Vitro* Co-Culture Assays

APC populations were double-sorted (yield followed by purity) from tdLN using a BD FACSAria Fusion and co-cultured with $2x10^4$ isolated eFluor670-labeled OT-II T cells at a 1:5 ratio in complete RPMI (Pen/Strep, NEAA, NaPyr, 2-ME, 10% FCS) in 96-well V-bottom plates. Cells were harvested for analysis 3 days later. OVA peptide 323-339 (GenScript) was added to wells at 1 μg/ml as a positive control.

Mouse T cell Isolation and *In Vivo* Adoptive T Cell Transfer

Inguinal, axillary, brachial, superficial cervical and mesenteric LN were isolated from $CD45.1^+$ OT-II mice. LN were smashed through 100 um filters and subsequently

spun down and counted. $CD4^+$ T cells were then isolated using EasySep CD4 negative-selection kits (STEMCELL Technologies).

$1x10^5$ isolated $CD45.1^+$ $CD4^+$ OT-II T cells were either transferred immediately in cases of PMA/Ionomycin restimulation experiments or labeled with Cell Proliferation Dye eFluor670 (Thermo Fisher Scientific) and $1.0\text{-}5.0x10^5$ cells were adoptively transferred to $CD45.2^+$ mice. LN were harvested for proliferation analysis at day 3 post-transfer and for PMA/ionomycin re-stimulation at day 7 post-transfer. *XCR1*^{DTR} and *Cx3cr1*^{iDTR} mice were treated with 500 ng of DT every other day beginning the day prior to OT-II transfer through the experimental end point. *Foxp3*^{DTR} mice were injected with DT for two days prior to OT-II transfer and then the day following OT-II transfer.

T Cell Cytokine Analysis

For cytokine analysis of endogenous or adoptively transferred T cells, cells from either LN or tumors were used for re-stimulation. Single cell suspensions were incubated with 50 ng/ml PMA (Sigma-Aldrich), 500 ng/ml ionomycin (Thermo Fisher Scientific), 3 µg/ml brefeldin A (Cayman Chemical Company), and 2µM monensin (Thermo Fisher Scientific) for 5-6 hours in complete RPMI and stained for surface and intracellular proteins using the Foxp3/Transcription Factor Staining Buffer Set (ThermoFisher Scientific).

In Vivo Treatments

For diphtheria toxin (DT), while treatment schedules varied depending upon mouse genetic strain or type of experiment, mice received 500 ng boluses of un-nicked

DT (List Biologics, 150) intraperitoneally. *Foxp3^{DTR}, XCR1^{DTR}* and *Cx3cr1^{iDTR}* mice were typically injected on days 9, 10 and 12 followed by flow cytometric analysis at day 14.

For comparisons of CD4$^+$ T_{conv} priming between steady-state, tumor-bearing and influenza-infected conditions, mice were injected subcutaneously with either 20 μg of endotoxin-free ovalbumin (Invivogen) in 50 μl of PBS or 2.0x10^5 B16ChOVA. Mice receiving influenza were infected intranasally with 1x10^5 PFU of X31-OT-II [214], prepared as previously described [215].CD45.1$^+$ OT-II$^+$ CD4$^+$ T cells were transferred intravenously 2 days after ovalbumin and X31-OT-II treatment and 14 days after B16^{ChOVA} injection.

To assess CD4/CD8 T cell dependency for tumor rejection following T_{reg} depletion or GVAX/anti-CTLA-4 treatment, mice were injected with 250 μg of isotype (Clone: LTF-2, BioXCell), anti-CD4 (Clone: GK1.5, BioXCell) or anti-CD8a (Clone: 2.43, BioXCell) was injected at days 10, 13 and 16 post-tumor injection for *Foxp3^{DTR}* and days 4, 7 and 10 for GVAX/anti-CTLA-4 treatment.

To assess the requirement of T cell LN egress, control or *Foxp3^{DTR}* mice were treated with 500 ng of DT on days 9, 10 and 12 post-tumor injection and with 200 μg FTY720 (Cayman Chemicals) every day beginning on day 8 post-tumor injection through the end of the experiment.

For GVAX/anti-CTLA-4 experiments, mice were injected with either 1x10^5 (tumor growth) or 2x10^5 B16-F10 (cellular analysis). On days 3, 6 and 9 post-tumor injection, mice were injected subcutaneously on their contralateral flank with either PBS or 1x10^6 50 Gy-irradiated GVAX cells and received either 250 μg anti-CTLA-4 (9H10, BioXCell) or Syrian hamster IgG isotype (BioXcell) on day 3, and 100 μg of antibody on days 6 and 9.

Statistical analysis and experimental design

Unless specifically noted, data displayed is from a representative experiment of ≥ 2 independent experiments. Experimental group assignment was determined by genotype or, if all wild-type mice, by random designation. Error bars represent mean ± S.E.M. calculated using Prism unless otherwise noted. Statistical analyses were performed using GraphPad Prism software. For pairwise comparisons, unpaired T tests were used unless otherwise noted. For statistical measures between more than two groups, one-way ANOVA would be performed unless otherwise noted. Comparisons found to be nonsignificant are not shown. Investigators were not blinded to group assignment during experimental procedures or analysis.

Figure 2.1

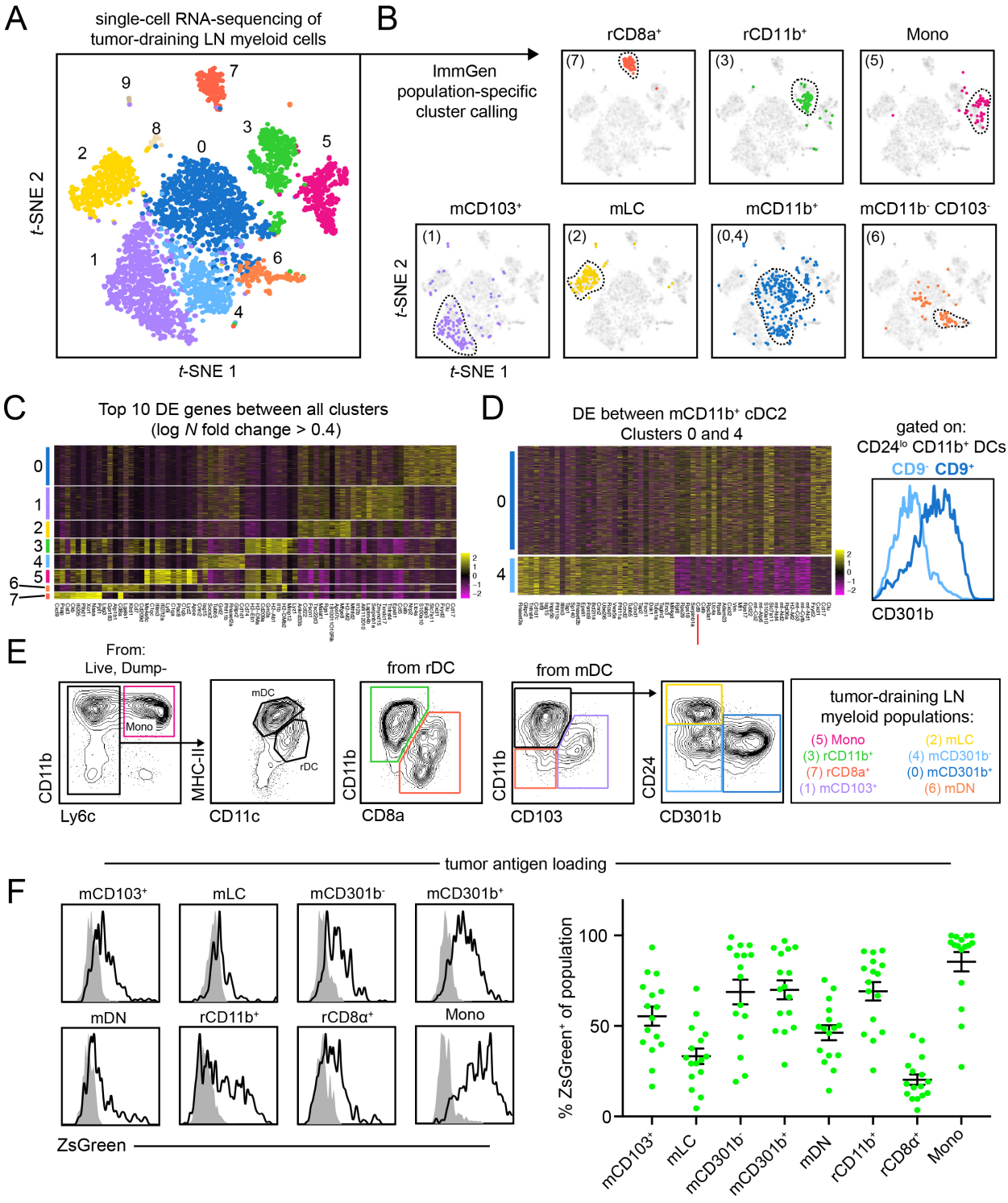
A
single-cell RNA-sequencing of tumor-draining LN myeloid cells
t-SNE 2
t-SNE 1
B
ImmGen population-specific cluster calling
rCD8a+
rCD11b+
Mono
mCD103+
mLC
mCD11b+
mCD11b- CD103-
C
Top 10 DE genes between all clusters (log N fold change > 0.4)
D
DE between mCD11b+ cDC2 Clusters 0 and 4
gated on: CD24lo CD11b+ DCs
CD9- CD9+
CD301b
E
From: Live, Dump-
Mono
mDC
rDC
CD11b
Ly6c
MHC-II
CD11c
from rDC
CD8a
from mDC
CD103
CD24
tumor-draining LN myeloid populations:
(5) Mono
(2) mLC
(3) rCD11b+
(4) mCD301b-
(7) rCD8a+
(0) mCD301b+
(1) mCD103+
(6) mDN
tumor antigen loading
F
mCD301b-
mCD301b+
mDN
ZsGreen
% ZsGreen+ of population

Figure 2.1 Unbiased scRNA-seq of myeloid cells in the tdLN reveals extensive heterogeneity.

(A) *t*-SNE display and graph-based clustering of CD90.2$^-$ B220$^-$ NK1.1$^-$ CD11b$^+$ and/or CD11c$^+$ myeloid cells sorted from B16F10 tdLN and processed for scRNA-seq. Each dot represents a single cell. **(B)** Expression of ImmGen population-specific gene signatures distributed across *t*-SNE plot of (A). **(C)** Heatmap displaying top 10 DE genes for each cluster when comparing clusters 0 through 7 (ranked by fold change) **(D) (left)** A heatmap displaying the top 30 DE genes between clusters 0 and 4, with *Cd9* highlighted by a red line. **(right)** A flow cytometry histogram displaying the differential surface expression of CD301b between CD9$^-$ and CD9$^+$ CD11b$^+$ CD24$^-$ DCs **(E)** Representative gating strategy used to identify myeloid populations in the tdLN **(F)** Representative flow cytometry histograms displaying levels of ZsGreen tumor antigen within myeloid populations in the tdLN **(left)**. Frequency of ZsGreen$^+$ cells within t dLN myeloid populations (**right**). Data pooled from two independent experiments.

Figure 2

Figure 2.2

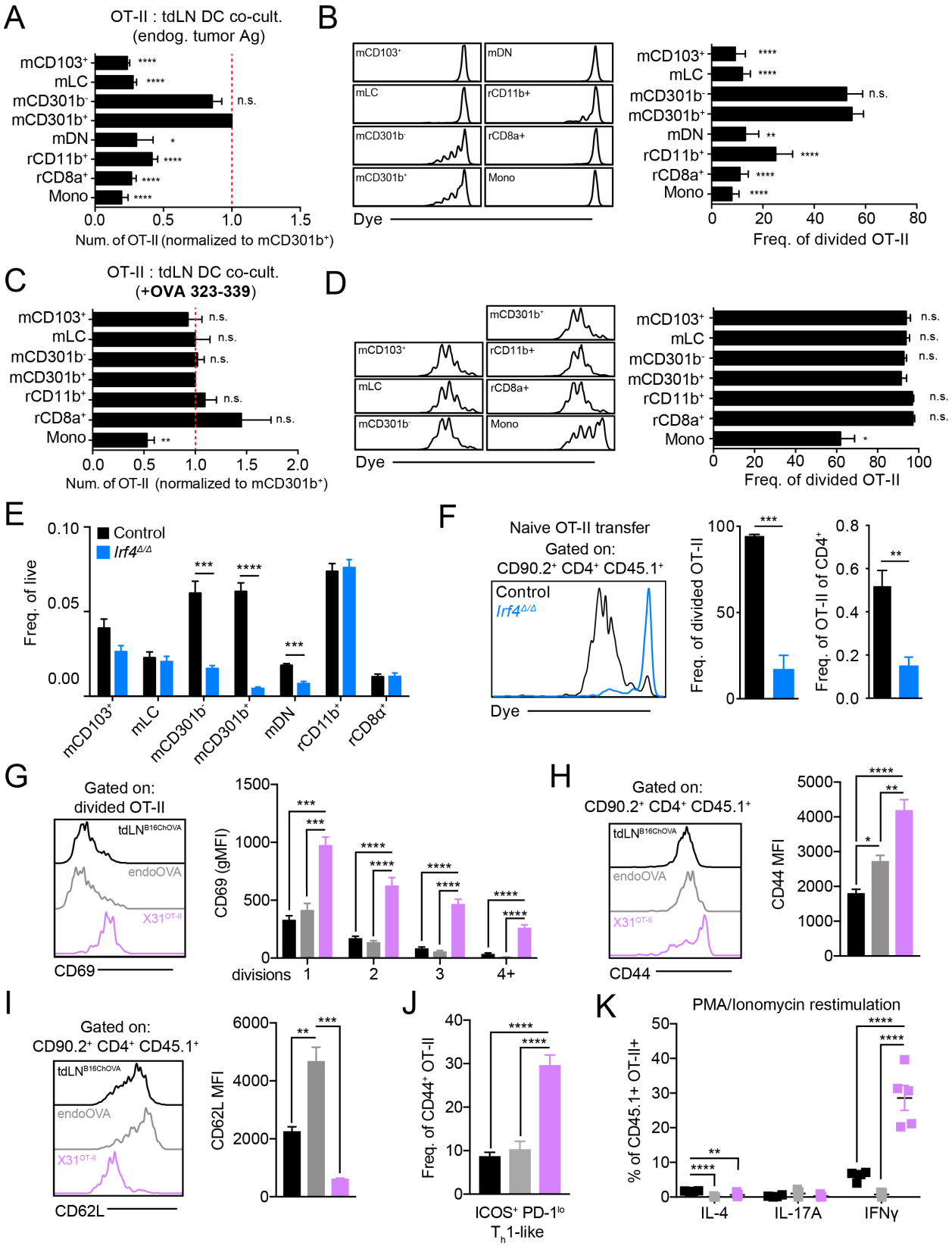
A
OT-II : tdLN DC co-cult.
(endog. tumor Ag)
mCD103+
mLC
mCD301b-
mCD301b+
mDN
rCD11b+
rCD8a+
Mono
n.s.
Num. of OT-II (normalized to mCD301b+)
B
Dye
Freq. of divided OT-II
C
OT-II : tdLN DC co-cult.
(+OVA 323-339)
Num. of OT-II (normalized to mCD301b+)
D
Dye
Freq. of divided OT-II
E
Control
Irf4Δ/Δ
Freq. of live
F
Naive OT-II transfer
Gated on:
CD90.2+ CD4+ CD45.1+
Control
Irf4Δ/Δ
Dye
Freq. of divided OT-II
Freq. of OT-II of CD4+
G
Gated on:
divided OT-II
tdLNB16ChOVA
endoOVA
X31OT-II
CD69
CD69 (gMFI)
divisions
H
Gated on:
CD90.2+ CD4+ CD45.1+
CD44
CD44 MFI
I
Gated on:
CD90.2+ CD4+ CD45.1+
CD62L
CD62L MFI
J
Freq. of CD44+ OT-II
ICOS+ PD-1lo
Th1-like
K
PMA/Ionomycin restimulation
% of CD45.1+ OT-II+
IL-4
IL-17A
IFNγ

Figure 2.2 mCD301b$^{-/+}$ cDC2 are uniquely able to induce anti-tumor CD4^{+} T_{conv} proliferation but fail to initiate CD4^{+} T_{conv} differentiation.

(**A-D**) Purified CD4^{+} OT-II T cells were co-cultured *ex vivo* with sorted APC populations from tdLN and analyzed at 3 days. **(A)** Absolute number of live OT-II T cells recovered from co-culture, normalized and statistically compared to mCD301b^{+} condition (t-test). **(B)** Histograms of OT-II T cell dye dilution **(left)**. Frequency of recovered OT-II T cells that had undergone division with statistical comparison to mCD301b^{+} condition (t-test) **(right)**. **(C)** Absolute number of live OT-II T cells recovered from co-culture containing exogenous OVA peptide (323-339), normalized and statistically compared to mCD301b^{+} condition (t-test). **(D)** Histograms of OT-II T cell dye dilution **(left)**. Frequency of recovered OT-II T cells that had undergone division with statistical comparison to mCD301b^{+} condition (t-test) **(right)**. **(E)** Frequency of tdLN DC populations in control or *Irf4*$^{-/-}$ tumor-bearing mice. **(F)** Purified CD45.1^{+} OT-II T cells were adoptively transferred to control or *Irf4*$^{-/-}$ B16^{ChOVA} tumor-bearing mice with tdLN harvested 3 days later to assess OT-II T cell dye dilution (**left**) and quantify the frequency of cells that had divided **(middle)** and their frequency of endogenous CD4^{+} T cells (**right**). (**G-K**) CD45.1^{+} CD4^{+} OT-II T cells were transferred to wild-type mice that were inoculated with B16^{chOVA} (tdLN^{B16ChOVA}), endoOVA, or X31^{pOVA} and draining LNs were harvested for analysis. (**G**) Cell surface CD69 levels on divided CD45.1^{+} CD4^{+} OT-II T cells (**left**) and quantification of MFI with each cell division as determined by dye dilution (**right**) 3 days following transfer. Surface CD44 (**H**) and CD62L (**I**) levels on transferred CD45.1^{+} CD4^{+} OT-II T cells (**left**) and quantification of MFI (**right**) 3 days following transfer. **(J)** Frequency of

transferred CD45.1^{+} CD4^{+} CD44^{+} OT-II T cells that are ICOS^{+}PD-1^{lo} T_h1-like. (**K**) Frequency of transferred CD45.1^{+} CD4^{+} CD44^{+} OT-II T cells that produce IL-4, IL-17A and IFNγ following PMA/Ionomycin restimulation with detection by intracellular antibody staining 7 days after transfer. Data are represented as average $\pm$ SEM unless explicitly specified. *P <0.05, **P<0.01, ***P<0.001, ****P<0.0001.

Figure 2.3

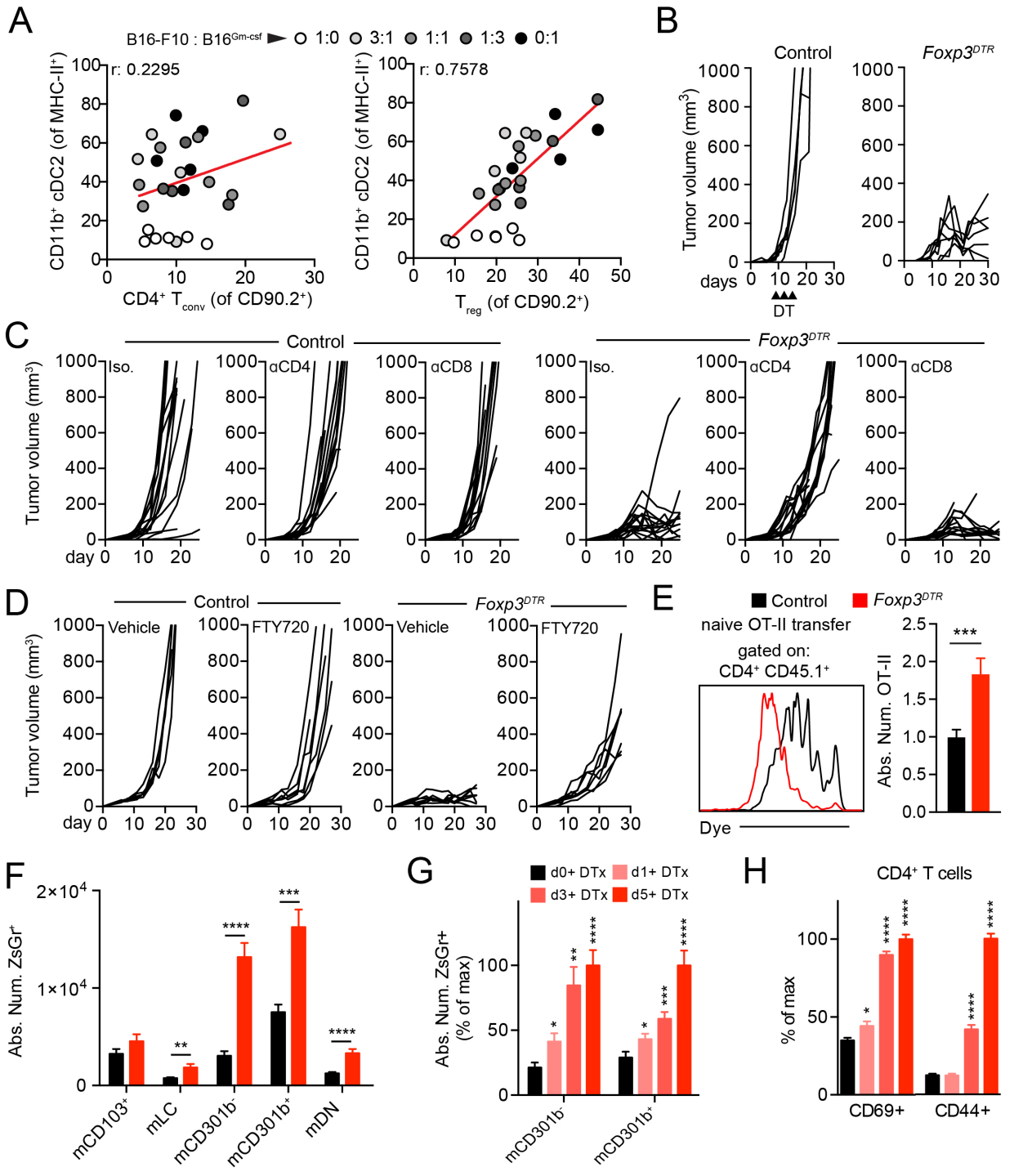
A
B16-F10 : B16Gm-csf
1:0
3:1
1:1
1:3
0:1
r: 0.2295
r: 0.7578
CD11b+ cDC2 (of MHC-II+)
CD4+ Tconv (of CD90.2+)
Treg (of CD90.2+)
B
Control
Foxp3DTR
Tumor volume (mm3)
days
DT
C
Control
Foxp3DTR
Iso.
αCD4
αCD8
Tumor volume (mm3)
day
D
Control
Foxp3DTR
Vehicle
FTY720
Tumor volume (mm3)
E
Control
Foxp3DTR
naive OT-II transfer
gated on:
CD4+ CD45.1+
Dye
Abs. Num. OT-II
F
Abs. Num. ZsGr+
mCD103+
mLC
mCD301b-
mCD301b+
mDN
G
d0+ DTx
d1+ DTx
d3+ DTx
d5+ DTx
Abs. Num. ZsGr+ (% of max)
mCD301b-
mCD301b+
H
CD4+ T cells
% of max
CD69+
CD44+

Figure 2.3 Regulatory T cell depletion enhances cDC2 migration to the tdLN and unleashes an anti-tumor $CD4^+$ T_{conv} response.

(A) Dot plot correlation of intratumoral $CD11b^+$ $CD301b^{-/+}$ cDC2 frequency within $MHC\text{-}II^+$ cells against $CD4^+$ T_{conv} within $CD90.2^+$ (**left**) or T_{reg} (**right**) within $CD90.2^+$. Dots colored according to ratio of B16-F10:$B16^{Gm\text{-}csf}$ cells in the tumor. Two pooled experiments displayed. **(B)** Tumor growth from control and *Foxp3*^{DTR} mice. Upward facing black arrowheads indicate DT treatment. Results depict tumor growth curves of individual mice. (**C**) Tumor growth from control or *Foxp3*^{DTR} mice injected with isotype/anti-CD4/anti-CD8 depleting antibodies. Results depict tumor growth curves of individual mice. Two pooled experiments displayed. **(D)** Tumor growth from control or *Foxp3*^{DTR} mice injected with with vehicle or FTY720. Results depict tumor growth curves of individual mice. Two pooled experiment displayed. **(E)** $CD45.1^+$ $CD4^+$ OT-II T cells were adoptively transferred into DT-treated control or *Foxp3*^{DTR} $B16^{ChOVA}$-tumor-bearing mice and recovered 3 days later for analysis of dye dilution (**left**) and quantification of absolute number of OT-II present within the tdLN (**right)**. Three pooled experiments displayed with normalization to control. (**F**) Control and *Foxp3*^{DTR} $B16^{ZsGreen}$ tumor-bearing mice were treated with DT and absolute number of $ZsGreen^+$ migratory DC in the tdLN were analyzed at day 5 post-DT. (**G**) Control and *Foxp3*^{DTR} $B16^{ZsGreen}$ tumor-bearing mice were treated with DT and absolute number of $ZsGreen^+$ $CD11b^+$ cDC2 in the tdLN were analyzed at day 0, 1, 3 and 5 post-DT. Data displayed as percent of maximum absolute number. Samples statistically compared to day 0 DT condition. (**H**) Control and *Foxp3*^{DTR} $B16^{ZsGreen}$ tumor-bearing mice were treated with DT and analyzed for the frequency of $CD4^+$ T_{conv} expressing CD69 and CD44 at day 0, 1, 3 and 5 post-

DT. Data displayed as frequency of maximum expression. Samples statistically compared to day 0 DT condition. Data are represented as average ± SEM. *P <0.05, **P<0.01, ***P<0.001, ****P<0.0001.

Figure 2.4

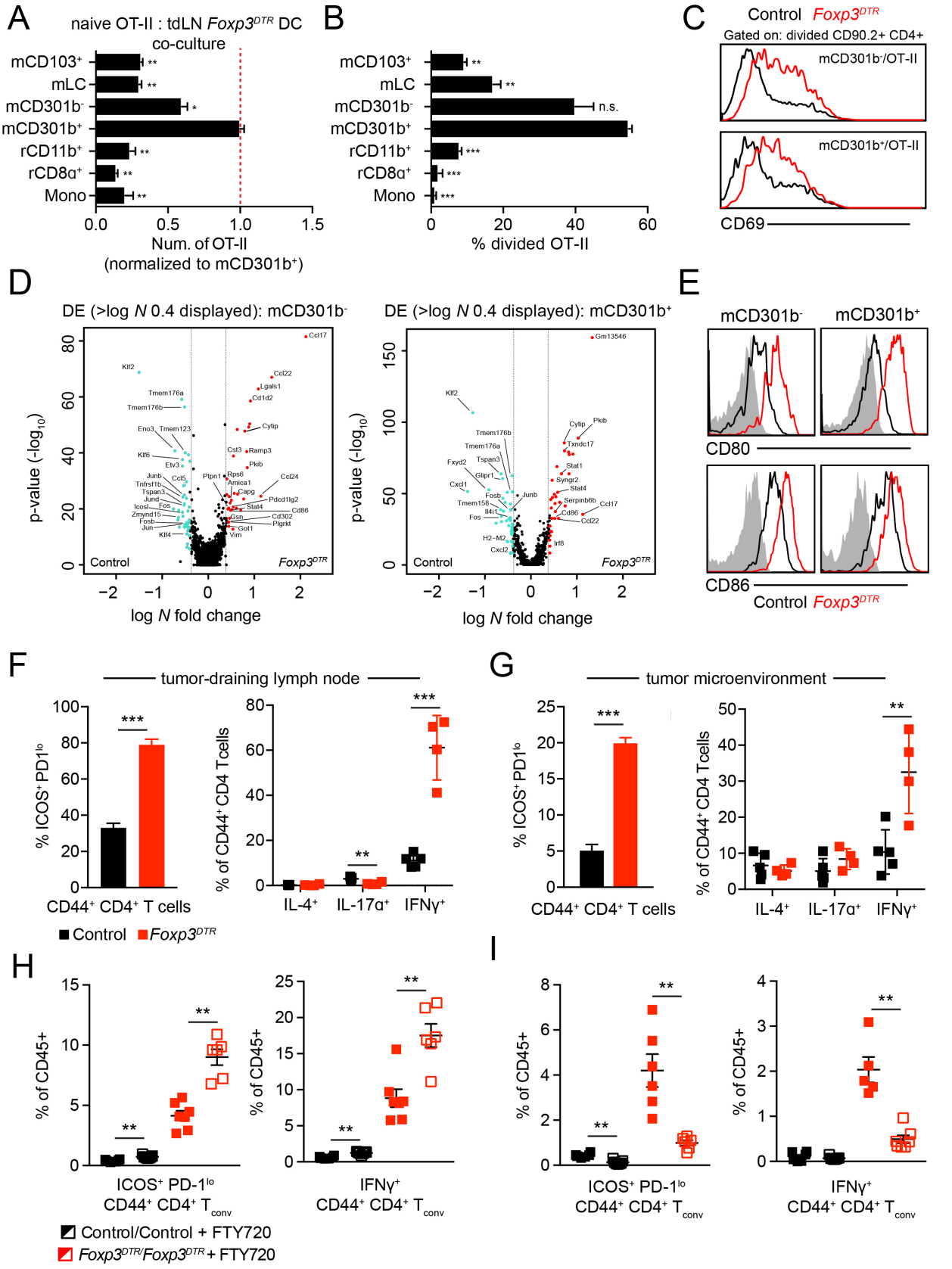
A
naive OT-II : tdLN Foxp3DTR DC co-culture
mCD103+
mLC
mCD301b-
mCD301b+
rCD11b+
rCD8α+
Mono
Num. of OT-II (normalized to mCD301b+)
B
% divided OT-II
n.s.
C
Control Foxp3DTR
Gated on: divided CD90.2+ CD4+
mCD301b-/OT-II
mCD301b+/OT-II
CD69
D
DE (>log N 0.4 displayed): mCD301b-
DE (>log N 0.4 displayed): mCD301b+
p-value (-log10)
log N fold change
Control
Foxp3DTR
E
mCD301b-
mCD301b+
CD80
CD86
Control Foxp3DTR
F
tumor-draining lymph node
% ICOS+ PD1lo
CD44+ CD4+ T cells
% of CD44+ CD4 Tcells
IL-4+
IL-17α+
IFNγ+
Control Foxp3DTR
G
tumor microenvironment
H
% of CD45+
ICOS+ PD-1lo CD44+ CD4+ Tconv
IFNγ+ CD44+ CD4+ Tconv
Control/Control + FTY720
Foxp3DTR/Foxp3DTR + FTY720
I

Figure 2.4 Regulatory T cell depletion enhances cDC2 function and $CD4^+$ T_{conv} differentiation.

(**A-C**) Purified $CD4^+$ OT-II T cells were co-cultured with tdLN APC populations sorted from tdLN of control or *Foxp3*^{DTR} B78chOVA-bearing animals and harvested 3 days after plating for analysis. **(A)** Absolute number of live OT-II T cells recovered, normalized and statistically compared to $mCD301b^+$ condition. **(B)** Frequency of recovered OT-II T cells that had undergone division, statistically compared to $mCD301b^+$ condition (t-test). (**C**) Cell surface CD69 levels on divided OT-II. (**D**) Volcano plots displaying DE expressed genes comparing control and Foxp3DTR tdLN $mCD301b^-$ (**left**) and $mCD301b^+$ (**right**). Log *N* fold cutoff of 0.4 used. Genes of interest labelled. (**E**) Cell surface levels of CD80 and CD86 on $mCD301b^-$ and $mCD301b^+$ in control and *Foxp3*^{DTR} tdLN. (**F**) Frequency of $CD44^+$ $CD4^+$ T_{conv} that are $ICOS^+$ PD-1^{lo} in control and *Foxp3*^{DTR} tdLN (**left**). Frequency of tdLN $CD44^+$ $CD4^+$ T_{conv} producing IL-4, IL-17A or IFNγ from control or *Foxp3*^{DTR} tumor-bearing mice following *ex vivo* restimulation (**right**). (**G**) Frequency of $CD44^+$ $CD4^+$ T_{conv} that are $ICOS^+$ PD-1^{lo} in control and *Foxp3*^{DTR} TME (**left**). Frequency of $CD44^+$ $CD4^+$ T_{conv} producing IL-4, IL-17A or IFNγ in control or *Foxp3*^{DTR} TME following *ex vivo* restimulation (**right**). (**H, I**) Control and *Foxp3*^{DTR} tumor-bearing mice were treated with FTY720 or vehicle and tdLN (H) or tumor (I) were harvested to quantify frequency of $CD45^+$ cells that are $CD44^+$ $CD4^+$ $ICOS^+$ PD-1^{lo} T_{conv} (**left**) and are IFNγ-producing $CD44^+$ $CD4^+$ T_{conv} following *ex vivo* restimulation (**right**). Representative experiment displayed. Data are represented as average ± SEM. *P <0.05, **P<0.01, ***P<0.001, ****P<0.0001

Figure 2.5

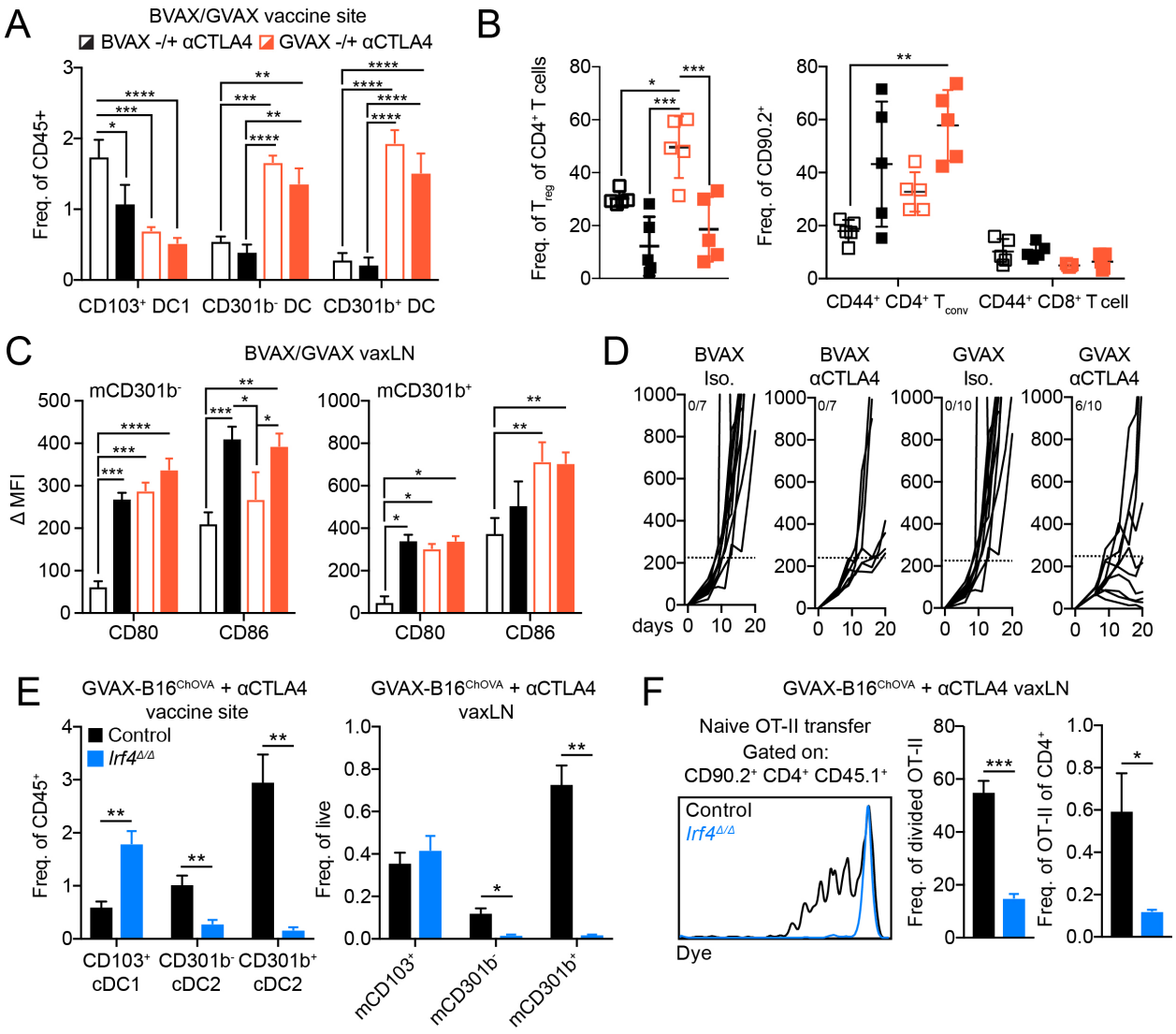
A
BVAX/GVAX vaccine site
BVAX -/+ αCTLA4
GVAX -/+ αCTLA4
Freq. of CD45+
CD103+ DC1
CD301b- DC
CD301b+ DC
B
Freq. of Treg of CD4+ T cells
Freq. of CD90.2+
CD44+ CD4+ Tconv
CD44+ CD8+ T cell
C
BVAX/GVAX vaxLN
mCD301b-
mCD301b+
Δ MFI
CD80
CD86
D
BVAX Iso.
BVAX αCTLA4
GVAX Iso.
GVAX αCTLA4
0/7
0/7
0/10
6/10
days
E
GVAX-B16ChOVA + αCTLA4 vaccine site
Control
Irf4Δ/Δ
Freq. of CD45+
CD103+ cDC1
CD301b- cDC2
CD301b+ cDC2
GVAX-B16ChOVA + αCTLA4 vaxLN
Freq. of live
mCD103+
mCD301b-
mCD301b+
F
GVAX-B16ChOVA + αCTLA4 vaxLN
Naive OT-II transfer
Gated on:
CD90.2+ CD4+ CD45.1+
Control
Irf4Δ/Δ
Dye
Freq. of divided OT-II
Freq. of OT-II of CD4+

Figure 2.5 GVAX/anti-CTLA-4 induces expansion and functional enhancement of CD11b$^+$ cDC2.

(**A**) DC frequency of CD45$^+$ cells within the vaccine site of mice treated with BVAX +/- αCTLA-4 or GVAX +/- αCTLA-4. (**B**) Frequency of T_{reg} amongst CD4$^+$ T cells (**left**) and frequency of CD44$^+$ CD4$^+$ T_{conv} or CD44$^+$ CD8$^+$ T cells amongst CD90.2$^+$ T cells within the vaccine site of mice treated with BVAX +/- αCTLA-4 or GVAX +/- αCTLA-4 (**right**). (**C**) Quantification of CD80 and CD86 ΔMFI on mCD301b$^-$ (**left**) or mCD301b$^+$ (**right**) within the vaxLN of mice treated with BVAX +/- αCTLA-4 or GVAX +/- αCTLA-4. (**D**) Tumor growth from mice treated with BVAX +/- αCTLA-4 or GVAX +/- αCTLA-4. Ratio represents number of mice with tumors that displayed profound response (< 250mm^3). Dotted line signifies 250 mm^3. Representative experiment displayed. (**E**) DC frequency of either CD45$^+$ or live cells within the vaccine site (left) or vaxLN (right) of control or *Irf4*$^{Δ/Δ}$ mice treated with GVAX-B16^{ChOVA} and anti-CTLA-4. (**F**) Purified CD45.1$^+$ OT-II T cells were adoptively transferred to control or *Irf4*$^{Δ/Δ}$ mice treated with GVAX-B16^{ChOVA} and anti-CTLA-4 and vavLN were harvested 3 days later to assess OT-II T cell dye dilution (**left**) and quantify the frequency of cells that had divided **(middle)** and their frequency of endogenous CD4$^+$ T cells (**right**). Data are represented as ± average SEM. *P <0.05, **P<0.01, ***P<0.001, ****P<0.0001.

Figure 2.6

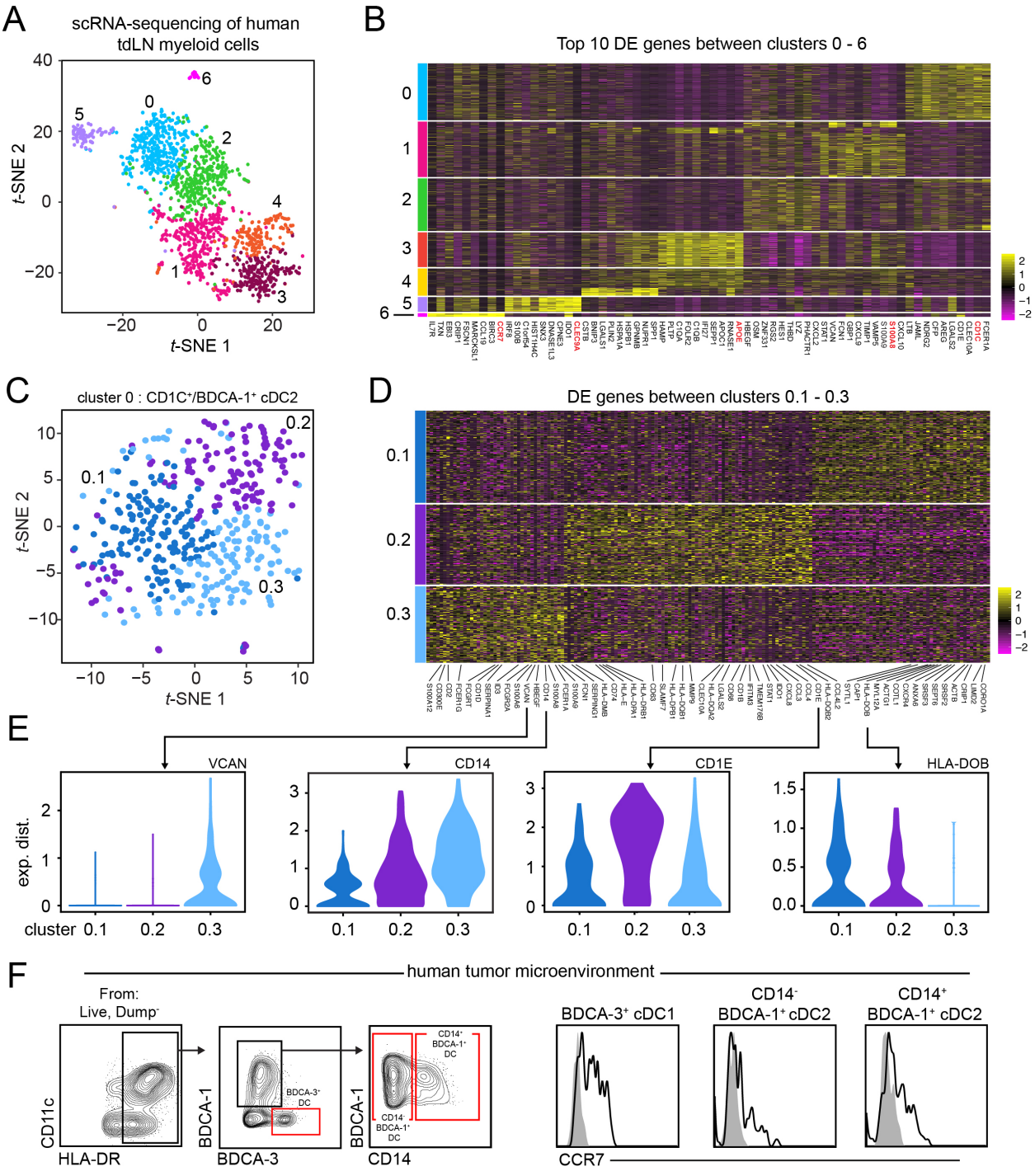
A
scRNA-sequencing of human tdLN myeloid cells
t-SNE 2
t-SNE 1
B
Top 10 DE genes between clusters 0 - 6
C
cluster 0 : CD1C+/BDCA-1+ cDC2
D
DE genes between clusters 0.1 - 0.3
E
VCAN
CD14
CD1E
HLA-DOB
exp. dist.
cluster 0.1 0.2 0.3
F
human tumor microenvironment
From:
Live, Dump-
CD11c
HLA-DR
BDCA-1
BDCA-3
BDCA-3+ DC
CD14+ BDCA-1+ DC
CD14-
BDCA-1+
DC
CD14
BDCA-3+ cDC1
CD14- BDCA-1+ cDC2
CD14+ BDCA-1+ cDC2
CCR7

Figure 2.6 scRNA-seq of the human tdLN reveals heterogeneity within BDCA-1$^+$ cDC2. **(A)** *t*-SNE display of CD45$^+$ CD3$^-$ CD19/20$^-$ CD56$^-$ myeloid cells sorted from a human melanoma tdLN and processed for scRNA-seq with pDC, neutrophil, NK cell, T cell and B cell contaminants removed from graph-based clustering analysis. (**B)** Heatmap displaying top 10 DE genes for each cluster when comparing clusters 0 through 6 (ranked by fold change). **(C)** *t*-SNE display and graph-based clustering of BDCA-1$^+$ cDC2 (cluster 0) from (A). **(D)** Heatmap displaying DE genes between clusters 0.1-0.3 with genes of interested labelled. **(E)** Violin plots displaying expression probability differences for denoted genes within clusters 0.1-0.3. (**F**) Gating strategy (**left**) in human TME to identify BDCA-3$^+$ cDC1, CD14$^-$ BDCA-1$^+$ cDC2, CD14$^+$ BDCA-1$^+$ cDC2. Cell surface expression of CCR7 on BDCA-3$^+$ cDC1, CD14$^-$ BDCA-1$^+$ cDC2, CD14$^+$ BDCA-1$^+$ cDC2 (**right**).

Figure 2.7

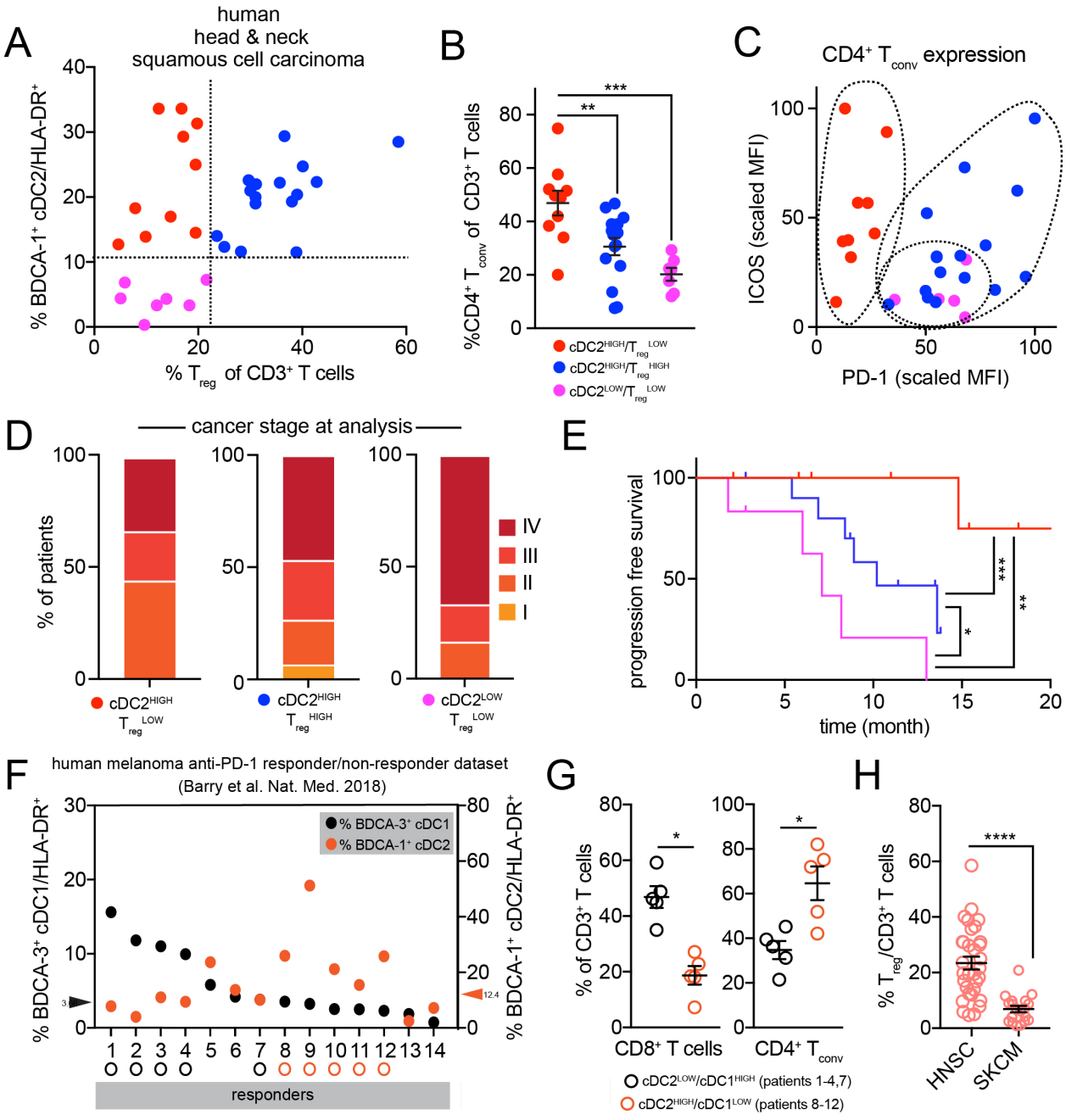
A
human
head & neck
squamous cell carcinoma
% BDCA-1+ cDC2/HLA-DR+
% Treg of CD3+ T cells
B
%CD4+ Tconv of CD3+ T cells
cDC2HIGH/TregLOW
cDC2HIGH/TregHIGH
cDC2LOW/TregLOW
C
CD4+ Tconv expression
ICOS (scaled MFI)
PD-1 (scaled MFI)
D
cancer stage at analysis
% of patients
IV
III
II
I
cDC2HIGH TregLOW
cDC2HIGH TregHIGH
cDC2LOW TregLOW
E
progression free survival
time (month)
F
human melanoma anti-PD-1 responder/non-responder dataset
(Barry et al. Nat. Med. 2018)
% BDCA-3+ cDC1/HLA-DR+
% BDCA-1+ cDC2/HLA-DR+
% BDCA-3+ cDC1
% BDCA-1+ cDC2
responders
G
% of CD3+ T cells
CD8+ T cells
CD4+ Tconv
cDC2LOW/cDC1HIGH (patients 1-4,7)
cDC2HIGH/cDC1LOW (patients 8-12)
H
% Treg/CD3+ T cells
HNSC
SKCM

Figure 2.7 BDCA-1$^+$ cDC2 proportion in the human TME impacts CD4$^+$ T_{conv} proportion and quality.

(**A**) Dot plot of BDCA-1$^+$ cDC2 frequency of HLA-DR$^+$ cells and T_{reg} frequency of CD3$^+$ T cells as quantified by flow cytometry in 32 human head and neck squamous cell carcinoma (HNSCC) tumor samples. Dotted lines represent demarcation of samples divided based on proportion of BDCA-1$^+$ cDC2 (CD14$^{-/+}$) and T_{reg}. (**B**) The frequency of CD4+ T cells (of CD3$^+$ T cells) within each type of TME identified in (A). (**C**) Surface expression of ICOS and PD-1 on CD4$^+$ T_{conv}, as a normalized geometric MFI, within each type of human TME identified in (A). (**D**) Percent of patients with a given stage of cancer at the time of flow cytometric analysis. (**E**) Progression-free survival since disease diagnosis. Mantel-Cox test performed between groups. (**F**) 19 human melanoma (SKCM) tumor samples (14 anti-PD-1 responder, 5 anti-PD-1 non-responders – see S6E) were parsed based on abundance of BDCA-3$^+$ cDC1 and plotted for proportions of both BDCA-3$^+$ cDC1 (black) and BDCA-1$^+$ cDC2 (orange). Responders were selected based on those high for either BDCA-3$^+$ cDC1 (above median split of 3.63) or BDCA-1$^+$ cDC2 (above median split of 12.4). (**G**) Frequency of CD3$^+$ T cells that are CD8$^+$ T cells (**left**) and CD4$^+$ T_{conv} (**right**) from the two groups identified in (F). (**H**) Proportions of T_{reg} amongst CD3$^+$ T cells in samples from HNSCC (A-E) and SKCM (includes anti-PD-1 responders and non-responders) (F, G). Data are represented as ± average SEM. *P <0.05, **P<0.01, ***P<0.001, ****P<0.0001.

Figure 2.8

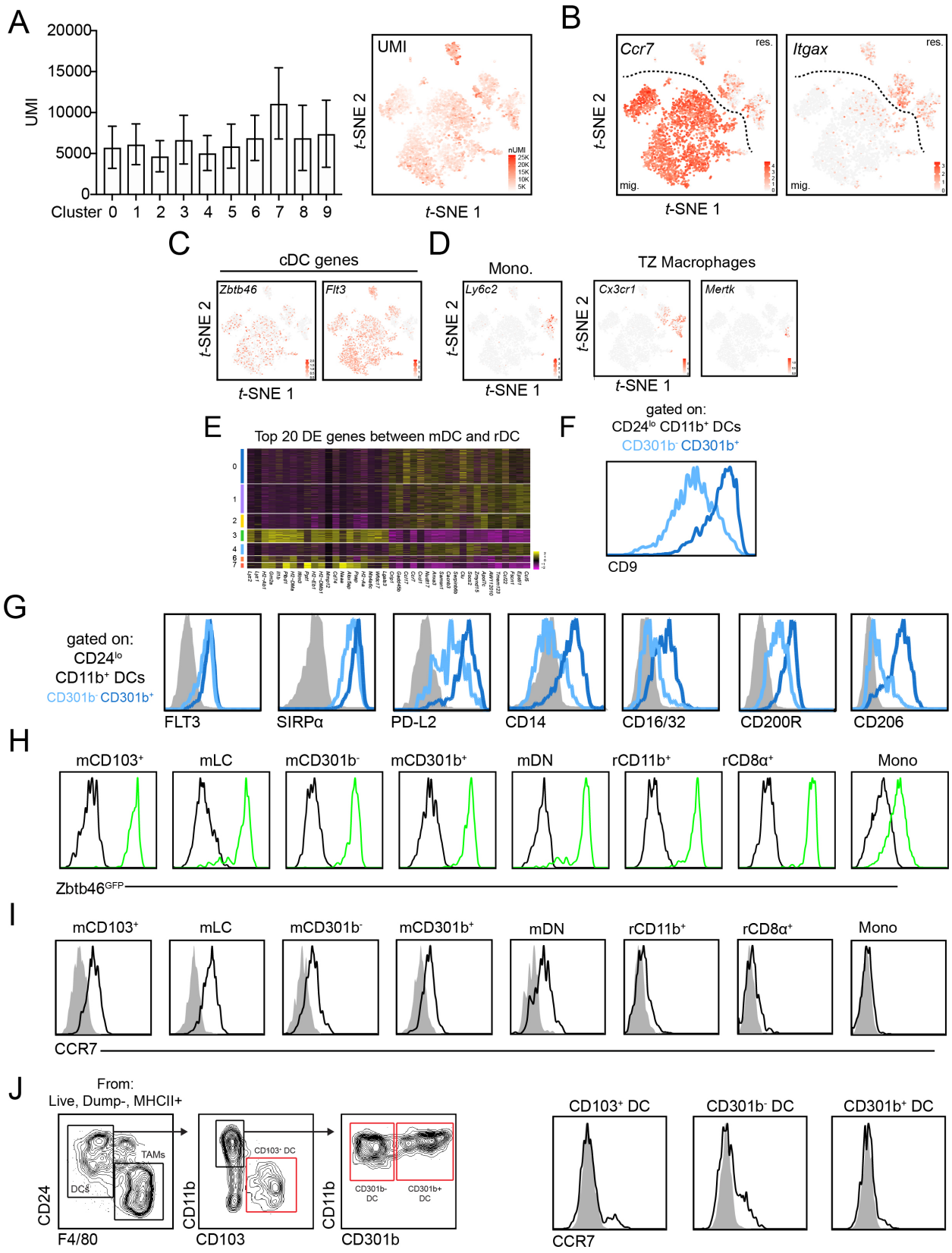
A
UMI
Cluster 0 1 2 3 4 5 6 7 8 9
UMI
t-SNE 2
t-SNE 1
B
Ccr7
Itgax
res.
mig.
t-SNE 2
t-SNE 1
C
cDC genes
Zbtb46
Flt3
t-SNE 2
t-SNE 1
D
Mono.
TZ Macrophages
Ly6c2
Cx3cr1
Mertk
t-SNE 2
t-SNE 1
E
Top 20 DE genes between mDC and rDC
F
gated on:
CD24lo CD11b+ DCs
CD301b- CD301b+
CD9
G
gated on:
CD24lo
CD11b+ DCs
CD301b- CD301b+
FLT3
SIRPα
PD-L2
CD14
CD16/32
CD200R
CD206
H
mCD103+
mLC
mCD301b-
mCD301b+
mDN
rCD11b+
rCD8α+
Mono
Zbtb46GFP
I
mCD103+
mLC
mCD301b-
mCD301b+
mDN
rCD11b+
rCD8α+
Mono
CCR7
J
From:
Live, Dump-, MHCII+
TAMs
DCs
CD24
F4/80
CD103+ DC
CD11b
CD103
CD301b- DC
CD301b+ DC
CD11b
CD301b
CD103+ DC
CD301b- DC
CD301b+ DC
CCR7

Figure 2.8 Unbiased scRNA-seq of myeloid cells in the tdLN reveals extensive heterogeneity, **relates to Figure 2.1**

(A) Average cell UMI across the 10 clusters present in the tdLN *t*-SNE (Figure 1A) with bars denoting standard deviation (**left**) and visual overlay of UMI count in each cell in the tdLN *t*-SNE (Figure 1A) (**right**)**. (B)** Gene expression overlay of *Ccr7* and *Itgax* plotted on the tdLN *t*-SNE. Scale bar indicates relative expression level. **(C)** Gene expression overlay of canonical cDC markers, *Zbtb46* and *Flt3* on the tdLN *t*-SNE. **(D)** Gene expression overlays of monocyte marker *Ly6c2* and T cell zone macrophage markers *Cx3cr1* and *Mertk* on the tdLN *t*-SNE**. (E)** Heatmap displaying top 20 DE genes for mDC and rDC when clusters 0, 1, 2, 4 and 6 are compared to clusters 3 and 7 (ranked by log N fold change). **(F)** Surface expression of CD9 on $CD301b^-$ and $CD301b^+$ $CD11b^+$ $CD24^{lo}$ DC populations. **(G)** Surface expression of denoted cell markers on $mCD301b^-$ and $mCD301b^+$. (**H**) GFP expression in myeloid populations detected in tdLNs from tumor-bearing $Zbtb46^{GFP}$ (green) and control (black) mice. **(I)** Surface levels of CCR7 on tdLN myeloid populations. **(J)** (left) Gating strategy of myeloid populations in mouse TME (**left**) and surface expression of CCR7 on tumor DC populations (**right**).

Figure 2.9

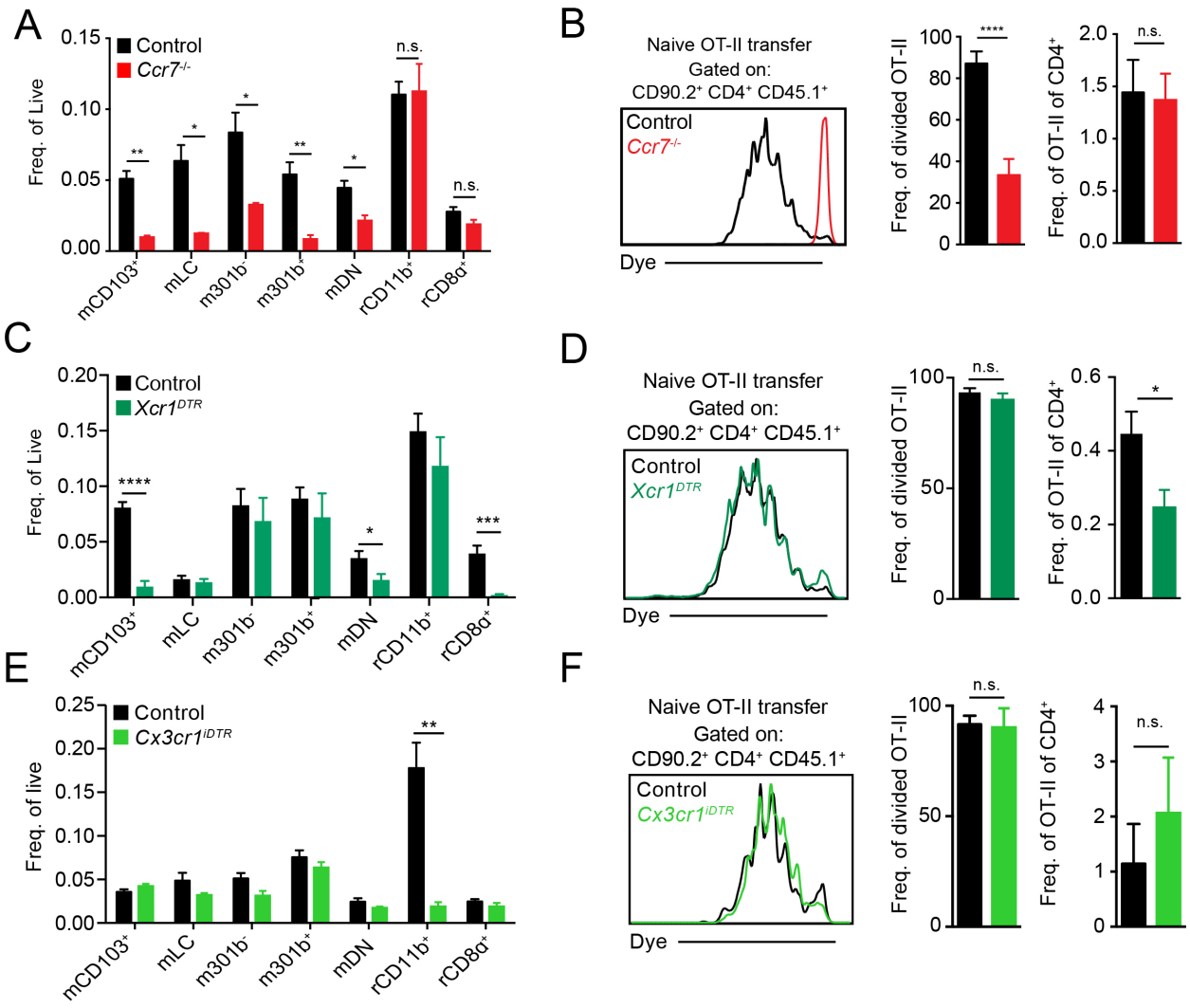
A
Control
Ccr7-/-
Freq. of Live
mCD103+
mLC
m301b-
m301b+
mDN
rCD11b+
rCD8α+
B
Naive OT-II transfer
Gated on:
CD90.2+ CD4+ CD45.1+
Control
Ccr7-/-
Dye
Freq. of divided OT-II
Freq. of OT-II of CD4+
C
Control
Xcr1DTR
Freq. of Live
D
Naive OT-II transfer
Gated on:
CD90.2+ CD4+ CD45.1+
Control
Xcr1DTR
Dye
Freq. of divided OT-II
Freq. of OT-II of CD4+
E
Control
Cx3cr1iDTR
Freq. of live
F
Naive OT-II transfer
Gated on:
CD90.2+ CD4+ CD45.1+
Control
Cx3cr1iDTR
Dye
Freq. of divided OT-II
Freq. of OT-II of CD4+

Figure 2.9 mCD301b$^{-/+}$ cDC2 are uniquely able to induce anti-tumor CD4^{+} T_{conv} proliferation but fail to initiate CD4^{+} T_{conv} differentiation, **relates to Figure 2.2**

(A) Frequency of tdLN DC populations in control or *Ccr7-/-* tumor-bearing mice. **(B)** Proliferation of CD45.1^{+} CD4^{+} OT-II T cells in tdLN that had been transferred to control or *Ccr7-/-* tumor-bearing mice 3 days prior as assessed by dye dilution (**left**), the frequency that had divided (**middle**), and their frequency of endogenous CD4^{+} T cells (**right**). **(C)** Frequency of tdLN DC populations in control or *Xcr1^{DTR}* tumor-bearing mice. **(D)** Proliferation of transferred CD45.1^{+} CD4^{+} OT-II T cells in tdLN of DT-treated control or *Xcr1^{DTR}* tumor-bearing mice with analysis of dye dilution (**left**), the frequency that had divided (**middle**), and their frequency of endogenous CD4^{+} T cells (**right**) 3 days post-transfer. **(E)** Frequency of tdLN DC populations in DT-treated control or *Cx3cr1^{iDTR}* tumor-bearing mice. **(F)** Proliferation of transferred CD45.1^{+} CD4^{+} OT-II T cells in tdLN of DT-treated control or *Cx3cr1^{iDTR}* tumor-bearing mice with analysis of dye dilution (**left**), the frequency that had divided (**middle**), and their frequency of endogenous CD4^{+} T cells (**right**) 3 days post-transfer. Data are represented as average ± SEM unless explicitly specified. *P <0.05, **P<0.01, ***P<0.001, ****P<0.0001.

Figure 2.10

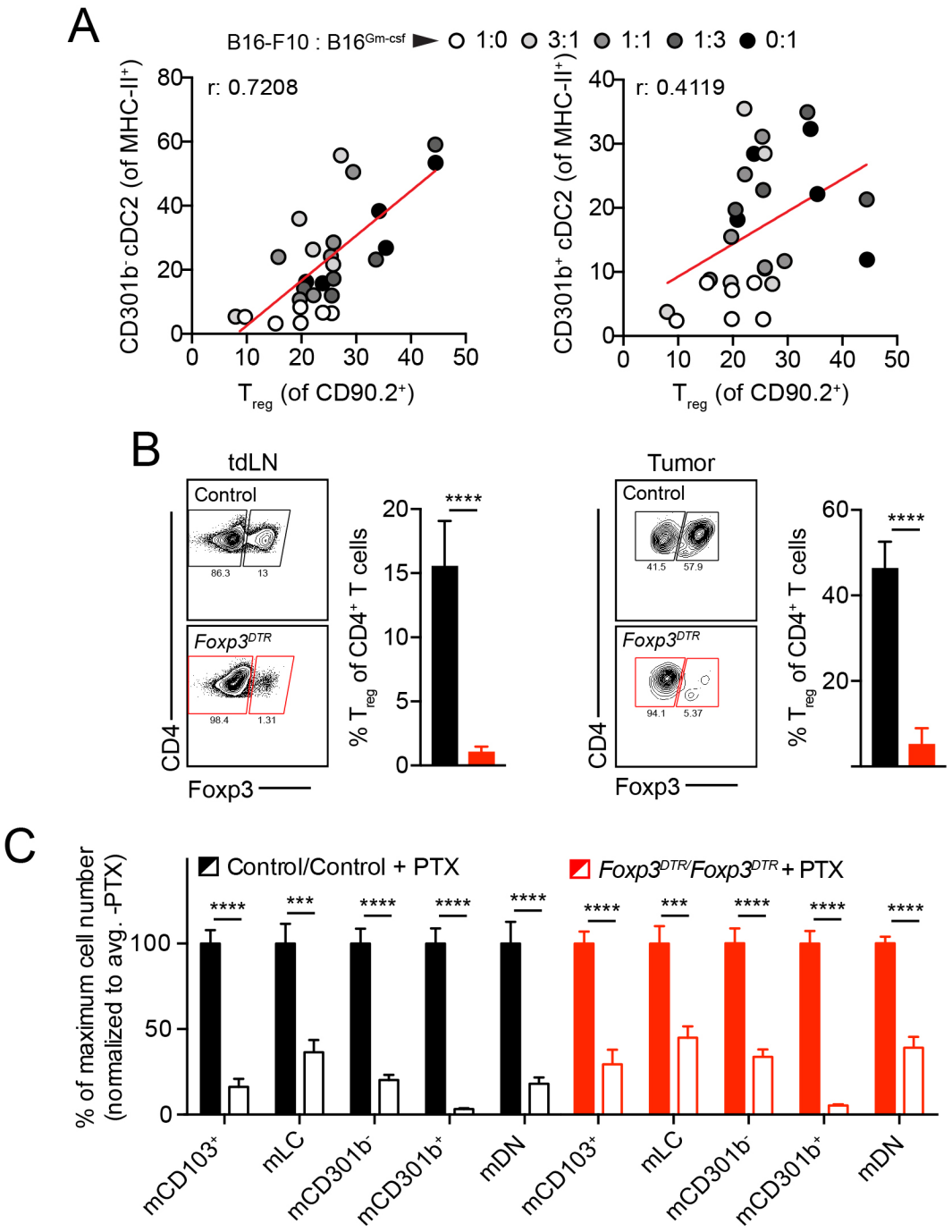
A
B16-F10 : B16Gm-csf
1:0
3:1
1:1
1:3
0:1
r: 0.7208
r: 0.4119
CD301b- cDC2 (of MHC-II+)
CD301b+ cDC2 (of MHC-II+)
Treg (of CD90.2+)
B
tdLN
Tumor
Control
Foxp3DTR
CD4
Foxp3
% Treg of CD4+ T cells
****
C
Control/Control + PTX
Foxp3DTR/Foxp3DTR + PTX
% of maximum cell number (nomalized to avg. -PTX)
***
mCD103+
mLC
mCD301b-
mCD301b+
mDN

Figure 2.10 Regulatory T cell depletion enhances cDC2 migration to the tdLN and unleashes an anti-tumor $CD4^+$ T_{conv} response, **relates to Figure 2.3.**

(A) Dot plot correlation of intratumoral $CD11b^+$ $CD301b^-$ cDC2 frequency within MHC-II^+ cells (**left**) or $CD11b^+$ $CD301b^-$ cDC2 within MHC-II^+ (**right**) and T_{reg} frequency within $CD90.2^+$ T cells. Best fit line shown. Pearson correlation performed for r value. Data pooled from two experiments. **(B)** Gating example of FoxP3 expression in $CD4^+$ T cells of DT-treated control and *Foxp3*^{DTR} mice and the frequency of $FoxP3^+$ T_{reg} within $CD4^+$ T cells in the tdLN (**left**) or tumor (**right**). Representative data of three independent experiments displayed. (**C**) Control and *Foxp3*^{DTR} B16-F10 tumor-bearing mice were treated with DT and PTX and absolute number of migratory DC in the tdLN were analyzed at day 5 post-DT. Samples normalized to their genetic -PTX condition. Representative data of two independent experiments displayed. Data are represented as ± SEM. *P <0.05, **P<0.01, ***P<0.001, ****P<0.0001.

Figure 2.11

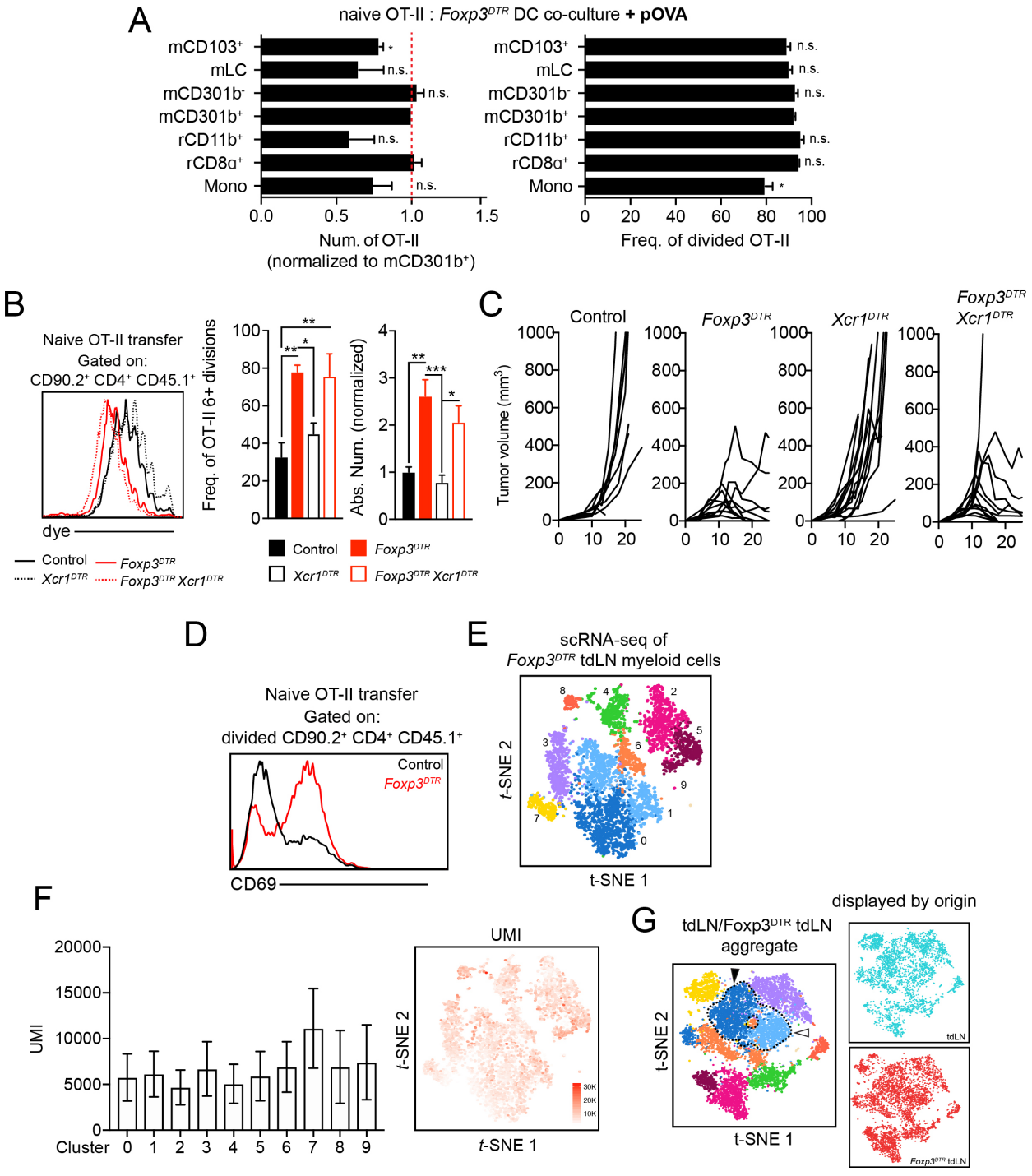
A
naive OT-II : Foxp3DTR DC co-culture + pOVA
mCD103+
mLC
mCD301b-
mCD301b+
rCD11b+
rCD8α+
Mono
n.s.
Num. of OT-II
(normalized to mCD301b+)
Freq. of divided OT-II
B
Naive OT-II transfer
Gated on:
CD90.2+ CD4+ CD45.1+
dye
Control
Foxp3DTR
Xcr1DTR
Foxp3DTR Xcr1DTR
Freq. of OT-II 6+ divisions
Abs. Num. (normalized)
C
Control
Foxp3DTR
Xcr1DTR
Foxp3DTR Xcr1DTR
Tumor volume (mm3)
D
Naive OT-II transfer
Gated on:
divided CD90.2+ CD4+ CD45.1+
CD69
E
scRNA-seq of
Foxp3DTR tdLN myeloid cells
t-SNE 1
t-SNE 2
F
UMI
Cluster
G
tdLN/Foxp3DTR tdLN
aggregate
displayed by origin
tdLN

Figure 2.11 Regulatory T cell depletion enhances cDC2 function and $CD4^+$ T_{conv} differentiation, **relates to Figure 2.4.**

(A) OT-II T cells were co-cultured with APC populations sorted from DT-treated *Foxp3^{DTR}* tdLN in media containing exogenous OVA peptide (323-339) and analyzed 3 days later for the absolute number of live (**left**) OT-II T cells recovered and the frequency of cells that had divided (**right**). Data was normalized and statistically compared to $mCD301b^+$ condition. (**B**) Proliferation of $CD45.1^+$ $CD4^+$ OT-II T cells in tdLN that had been transferred to control, *Foxp3^{DTR}*, *Xcr1^{DTR}*, or *Foxp3^{DTR}Xcr1^{DTR}* tumor-bearing mice 3 days prior as assessed by dye dilution (**left**). Frequency of OT-II that divided 6+ times (**middle**). The absolute number of transferred OT-II (**right**). (**C**) Tumor growth from control, *Foxp3^{DTR}, Xcr1^{DTR} and Foxp3^{DTR}Xcr1^{DTR}* mice. Results depict tumor growth curves of individual mice. **(D)** Cell surface CD69 levels on divided OT-II T cells 3 days after transfer into DT-treated control and *Foxp3^{DTR}* $B16^{ChOVA}$ tumor-bearing mice. Representative data of three independent experiments displayed. **(E)** *t*-SNE plot and graph-based clustering of $CD90.2^-$ $B220^-$ $NK1.1^-$ $CD11b^+$ and/or $CD11c^+$ myeloid cells sorted from a DT-treated *Foxp3^{DTR}* B16F10 tdLN and processed for scRNA-seq. Each dot represents a single cell. **(F)** Average cell UMI across the 10 clusters present in the primary *Foxp3^{DTR}* tdLN *t*-SNE from **S6E** (**left**) with bars denoting standard deviation, and visual overlay of UMI count of each cell within the primary *Foxp3^{DTR}* tdLN *t*-SNE from **S6E** (**right**)**. (G)** *t*-SNE display and graph-based clustering of aggregated control and Foxp3DTR tdLN sequenced cells (**left**). Cellular origin within the aggregated *t*-SNE highlighted (**top right, bottom right**).

Figure 2.12

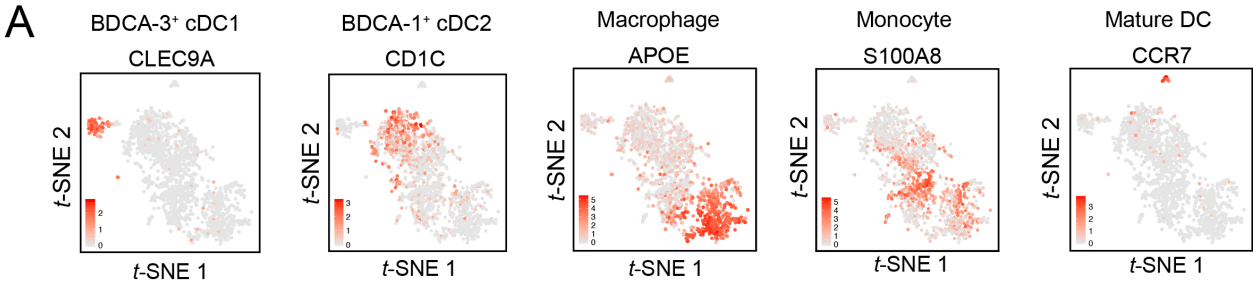

Figure 2.12 scRNA-seq of the human tdLN reveals heterogeneity within BDCA-1$^+$ cDC2, **relates to Figure 2.6.**

(A) Gene overlays of markers associated with various myeloid cell types on human tdLN *t*-SNE (Figure 6A).

Figure 2.13

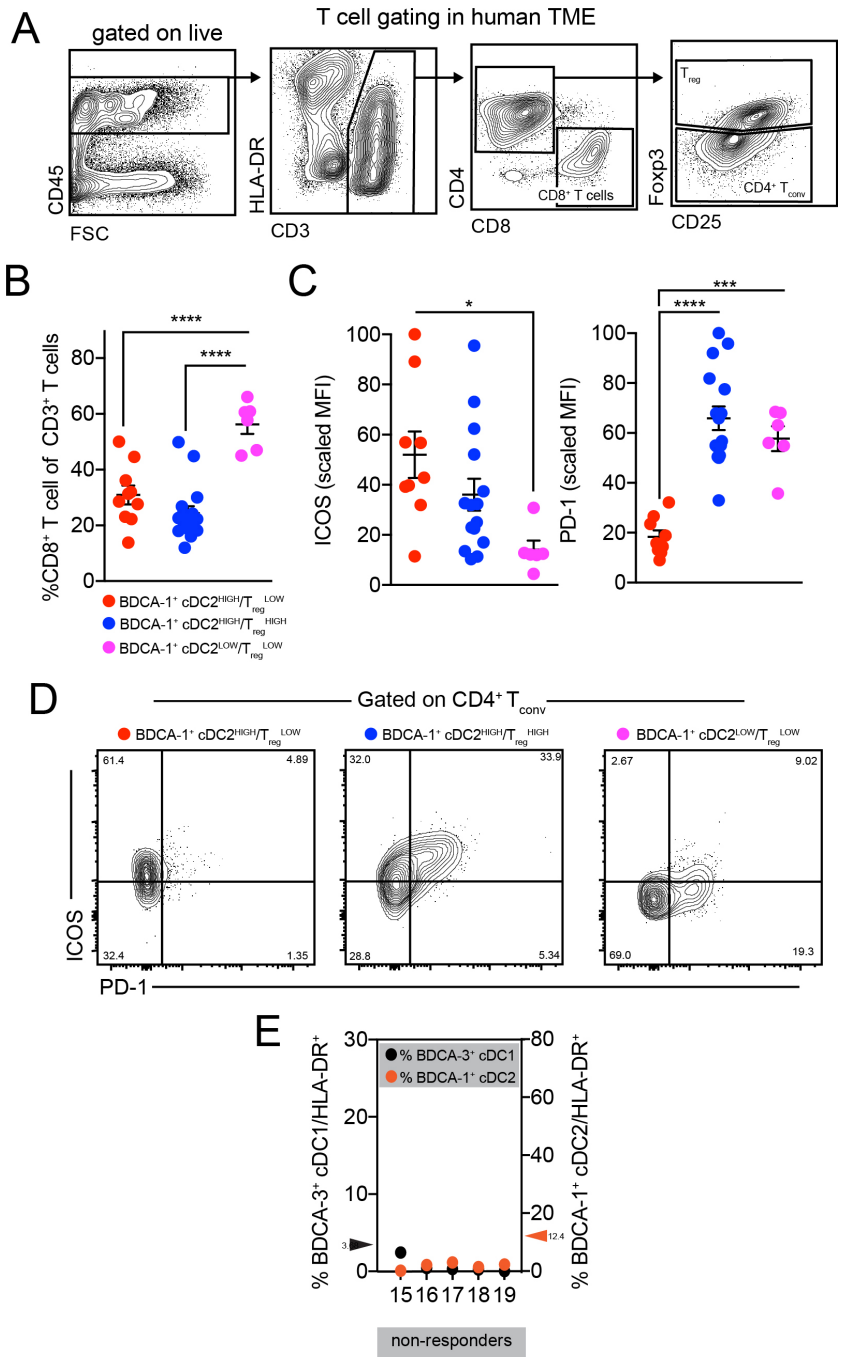
A
gated on live
T cell gating in human TME
CD45
FSC
HLA-DR
CD3
CD4
CD8
CD8+ T cells
Foxp3
CD25
Treg
CD4+ Tconv
B
%CD8+ T cell of CD3+ T cells
BDCA-1+ cDC2HIGH/Treg LOW
BDCA-1+ cDC2HIGH/Treg HIGH
BDCA-1+ cDC2LOW/Treg LOW
C
ICOS (scaled MFI)
PD-1 (scaled MFI)
D
Gated on CD4+ Tconv
ICOS
PD-1
61.4
4.89
32.4
1.35
32.0
33.9
28.8
5.34
2.67
9.02
69.0
19.3
E
% BDCA-3+ cDC1/HLA-DR+
% BDCA-1+ cDC2/HLA-DR+
% BDCA-3+ cDC1
% BDCA-1+ cDC2
non-responders

Figure 2.13 BDCA-1$^+$ cDC2 proportion in the human TME impacts CD4$^+$ T_{conv} proportion and quality, **relates to Figure 2.7**

(**A**) Gating strategy of human HNSC TME to identify T cell populations. (**B**) Frequency of CD8$^+$ T cells (of CD3$^+$ T cells) within each type of HNSC TME identified in Figure 7A. (**C**) Scaled ICOS (**left**) and PD-1 (**right**) MFI on CD4$^+$ T_{conv} within each type of HNSC TME identified in Figure 7A (**left**). (**D**) Representative example of ICOS and PD-1 expression on CD4$^+$ T_{conv} within each HNSC TME subset. (**E**) Frequency of BDCA-3$^+$ cDC1 (black) and BDCA-1+ cDC2 (orange) within HLA-DR$^+$ cells in human melanoma tumors from 5 anti-PD-1 non-responders.

Table 2.1

ImmGen population	sample name	replicates
DC.8+.SLN	rCD8a+	3
DC.4+.SLN	rCD11b+	3
DC.IIhilang-103-11blo.SLN	mDN	3
DC.IIhilang+103+11blo.SLN	mCD103+	3
DC.IIhilang+103-11b+.SLN	mLC	3
DC.IIhilang-103-11b+.SLN	mCD11b+	3
Mo.6C+II-.Bl	Mono	5
Mo.6C+II+.Bl		

	Gene	logFC	AveExpr	adj.P.Val	population
	Clec9a	6.0453	5.8463	2.3E-07	rCD8a+
*	Xcr1	5.2157	6.4971	3.4E-14	rCD8a+
*	Gcsam	4.5376	5.8064	2.3E-11	rCD8a+
	Cxcl9	4.4250	7.2124	2.3E-07	rCD8a+
*	Hepacam2	4.4128	5.5057	9.8E-11	rCD8a+
*	Tlr3	4.2569	5.7582	6.8E-14	rCD8a+
*	Snx22	3.1860	6.3865	7.8E-11	rCD8a+
*	Pdia5	3.1521	7.0875	1.8E-11	rCD8a+
*	Clnk	3.0847	5.8176	9.6E-13	rCD8a+
	Fam149a	2.7531	6.3720	1.8E-10	rCD8a+
*	Clec1a	2.7458	5.2666	4.2E-11	rCD8a+
*	Cxcr3	2.7181	7.3807	9.4E-12	rCD8a+
*	1700009J07Rik	2.6434	5.8070	9.4E-12	rCD8a+
	Itgae	2.4314	5.9630	1.3E-07	rCD8a+
	Notch4	2.1416	6.8418	6.2E-10	rCD8a+
	Dbn1	2.1235	6.8576	1.1E-08	rCD8a+
	Naga	1.8590	9.9249	9.2E-08	rCD8a+
	Ifnlr1	1.6591	6.2720	2.7E-07	rCD8a+
	Eefsec	1.6021	7.9756	1.1E-08	rCD8a+
	Arid3b	1.4773	6.9577	1.2E-07	rCD8a+
*	Mmp12	4.8078	6.0647	3.4E-13	rCD11b+
*	Mgl2	4.6375	5.7625	1.7E-08	rCD11b+
*	Cd4	3.6664	6.5537	6.1E-09	rCD11b+
	Rgl1	2.8025	6.9580	9.6E-06	rCD11b+
*	Klrb1b	2.6520	5.6951	5.2E-07	rCD11b+
	Egr2	2.6413	6.8819	6.3E-07	rCD11b+
*	Hr	2.2537	6.6558	9.2E-10	rCD11b+
	Cd209d	2.0825	5.3407	1.4E-04	rCD11b+
	Lphn3	1.8031	4.6999	8.3E-07	rCD11b+
*	Fcrls	1.5823	4.7863	5.0E-08	rCD11b+
	Slc2a3	1.4923	6.7267	2.9E-04	rCD11b+
	Ctnnd2	1.4801	6.6717	1.5E-05	rCD11b+
*	Clec4g	1.4722	5.5170	3.0E-06	rCD11b+
	Cyp4f37	1.1100	4.9626	2.1E-04	rCD11b+
*	Ggt5	1.0227	6.4149	4.2E-06	rCD11b+
	Dcstamp	0.9725	5.2880	1.4E-04	rCD11b+
	Cox6b2	0.8364	6.3361	2.2E-04	rCD11b+
	Stk25	-0.8156	8.4029	3.9E-04	rCD11b+
	Arid2	-0.9218	8.8855	1.9E-04	rCD11b+

	Gene	logFC	AveExpr	adj.P.Val	population
	Ermard	-1.0918	8.0013	4.6E-04	rCD11b+
*	Khdc1a	2.8835	3.9299	5.8E-07	mDN
*	Khdc1c	2.8771	5.9704	5.8E-07	mDN
*	Sned1	2.3779	7.3490	3.2E-04	mDN
*	Clmn	2.1187	5.4687	2.6E-04	mDN
	Khdc1b	1.8016	5.5040	6.0E-06	mDN
*	Gdpd1	1.3379	5.1630	2.2E-04	mDN
*	Efna5	1.3041	6.1494	2.8E-04	mDN
*	Gm15698	3.5437	5.8649	9.7E-06	mCD103+
*	Vmn2r90	3.0364	5.1163	2.5E-05	mCD103+
*	Slc27a3	2.7056	6.7149	3.6E-05	mCD103+
	Gltpd1	2.5726	7.4650	1.5E-04	mCD103+
	Arg2	2.3732	6.1897	1.7E-04	mCD103+
	Zdhhc14	2.1802	7.4723	3.2E-04	mCD103+
*	Arhgap8	1.9746	6.1339	2.4E-07	mCD103+
	Cd96	1.5481	5.2300	1.4E-04	mCD103+
*	Exoc3l4	1.5155	7.0362	1.1E-05	mCD103+
	Colq	1.3886	6.8375	3.2E-04	mCD103+
*	Mfsd4	1.3693	6.8100	2.5E-05	mCD103+
	2210409E12Rik	1.3382	6.6145	1.4E-04	mCD103+
	Erich5	1.3100	6.3656	1.1E-04	mCD103+
*	Slc18a1	1.2558	5.6380	8.9E-06	mCD103+
	Sprr4	1.0699	5.9662	1.5E-04	mCD103+
*	Sh3gl1	0.9942	8.6567	4.0E-05	mCD103+
	Adrm1	0.6508	8.8218	1.4E-04	mCD103+
	Adrm1	0.6500	8.7883	1.9E-04	mCD103+
*	1810011O10Rik	5.7479	4.8945	9.5E-16	mLC
*	Fam189a2	4.4585	6.1501	4.6E-11	mLC
	Fam115c	4.0949	5.7914	3.6E-12	mLC
	Npy1r	4.0426	5.4201	2.2E-07	mLC
	Atf7ip2	3.4395	5.1965	2.1E-06	mLC
*	Nbea	3.3415	5.3563	3.7E-12	mLC
*	Fam160a1	3.0305	6.3350	8.2E-11	mLC
	Tjp1	2.6631	5.3330	3.6E-10	mLC
*	Pcdh7	2.3367	5.5365	2.0E-08	mLC
	Pxdn	2.0861	5.8142	5.7E-08	mLC
	9330155M09Rik	2.0174	3.4478	2.0E-08	mLC
	Epb4.1l3	1.9747	5.6021	6.4E-07	mLC
	Map2	1.9451	5.4537	1.2E-07	mLC
	Fblim1	1.9175	6.1430	3.9E-07	mLC
	Apbb2	1.8244	6.4300	5.7E-07	mLC
*	Stxbp5l	1.6258	4.3168	2.4E-11	mLC
	Cadm2	1.5911	5.0181	3.9E-07	mLC
	Tmem45b	1.4376	5.5234	2.5E-06	mLC
	Agmo	1.3380	4.1082	2.5E-06	mLC
	Aldh1a2	4.7680	6.3960	1.3E-03	mCD11b+
	Gm5486	3.8271	5.5478	9.5E-04	mCD11b+
	Serpinb9b	3.1731	6.4721	9.5E-04	mCD11b+
	Cxcl13	3.0526	5.8987	3.0E-04	mCD11b+
*	Htra1	2.8685	5.7485	7.6E-05	mCD11b+
	Rai14	2.2526	6.4865	4.6E-04	mCD11b+
*	Car2	2.1700	6.1995	8.0E-05	mCD11b+

	Gene	logFC	AveExpr	adj.P.Val	population
*	Sod3	2.1562	5.5361	1.8E-05	mCD11b+
*	Grpr	2.0489	5.1700	9.6E-06	mCD11b+
*	AA467197	1.9255	5.6350	6.3E-05	mCD11b+
	Mucl1	1.8875	3.7911	2.1E-05	mCD11b+
	Depdc7	1.8215	6.1404	9.3E-04	mCD11b+
	Gm5622	1.7573	4.6778	8.1E-04	mCD11b+
	LOC102634703	1.7203	4.7592	4.3E-05	mCD11b+
	LOC101055806	1.6901	3.4570	1.8E-05	mCD11b+
	Gm10375	1.6646	3.9046	1.8E-05	mCD11b+
	LOC102634703	1.5880	4.6571	9.4E-05	mCD11b+
	Ms4a14	1.3324	3.9208	8.0E-04	mCD11b+
	Fabp4	1.2515	4.7717	4.6E-04	mCD11b+
	Gm10375	1.0393	3.8883	4.2E-04	mCD11b+
*	F13a1	7.0452	7.1382	1.4E-19	Mono
	Klra2	6.5515	5.4958	1.9E-13	Mono
	Chil3	6.0381	5.3666	1.6E-13	Mono
*	Serpinb10	5.9713	5.1624	3.2E-16	Mono
	Ms4a6d	5.5989	6.6334	2.6E-13	Mono
	Msr1	5.4280	5.4302	1.9E-13	Mono
*	Cd93	5.0419	6.4879	1.4E-19	Mono
*	Fcgr1	4.8002	7.2360	2.2E-18	Mono
*	Fgd4	4.4340	5.8459	8.1E-14	Mono
*	Arhgef37	4.2467	5.7495	1.6E-14	Mono
*	Thbd	3.6346	6.7092	3.4E-14	Mono
	Pde7b	3.3830	5.7471	8.3E-14	Mono
*	Rasgrp2	3.1460	6.7385	6.9E-15	Mono
	Oas3	2.8684	7.1183	1.7E-13	Mono
	C5ar1	2.8614	5.6460	1.8E-13	Mono
	Hip1	2.6104	6.9733	2.3E-13	Mono
	Siglec1	2.2416	6.8664	1.1E-13	Mono
	Nedd4	-4.2161	8.8719	1.8E-13	Mono
	Adam23	-6.4232	10.0104	7.1E-18	Mono

Table 2.1 – relates to Figure 2.1. ImmGen population specific gene signatures. (top) ImmGen sample ID, abbreviated sample name and replicates used in creation on ImmGen population specific gene signature. (bottom) DE was performed comparing one population to the aggregate of the 6 remaining populations. DE is ranked based on log fold change. An asterisk indicates gene was detected in scRNA-seq and thus used for gene signature overlay. See materials and methods for specific process through which DE signature was generated.

Table 2.2

gene	avg_logFC	pct.1	pct.2	p_val	p_val_adj	cluster
Ccl17	1.5851	0.584	0.198	5.10E-148	7.40E-144	0
Clu	1.2221	0.641	0.305	2.20E-119	3.30E-115	0
Fxyd2	1.0765	0.548	0.221	2.60E-114	3.80E-110	0
Cxcl1	0.9985	0.407	0.238	8.60E-37	1.30E-32	0
Slc7a11	0.932	0.566	0.186	2.20E-136	3.20E-132	0
Fabp5	0.8807	0.959	0.628	4.20E-205	6.10E-201	0
S100a10	0.7559	0.587	0.297	2.20E-89	3.20E-85	0
Ltc4s	0.7358	0.689	0.329	8.20E-117	1.20E-112	0
Nrp2	0.723	0.534	0.183	2.00E-124	2.80E-120	0
Cstb	0.7211	0.904	0.757	9.10E-122	1.30E-117	0
Ccl5	1.3933	0.999	0.979	2.10E-226	3.10E-222	1
Epsti1	1.3074	0.995	0.885	2.00E-269	2.90E-265	1
Tnfrsf4	1.1602	0.797	0.335	5.10E-192	7.40E-188	1
Txndc17	1.1027	0.947	0.745	1.40E-227	2.00E-223	1
Zmynd15	1.045	0.947	0.537	1.20E-227	1.80E-223	1
Serpinb1a	0.9627	0.574	0.279	2.40E-74	3.50E-70	1
Laptm4b	0.9457	0.614	0.105	5.00E-259	7.20E-255	1
AW112010	0.9084	0.99	0.859	2.00E-173	3.00E-169	1
Il12b	0.8985	0.386	0.118	2.80E-82	4.00E-78	1
Mthfd2	0.8587	0.825	0.509	1.50E-148	2.20E-144	1
H2-M2	1.4223	0.998	0.55	2.10E-204	3.00E-200	2
Mfge8	1.2891	0.826	0.356	7.10E-132	1.00E-127	2
Apol7c	0.9388	0.96	0.674	6.30E-98	9.10E-94	2
1810011O10Rik	0.8978	0.317	0.007	7.90E-216	1.20E-211	2
Rgs1	0.7823	0.966	0.875	2.00E-66	3.00E-62	2
Malat1	0.7443	1	0.999	6.60E-155	9.60E-151	2
Tsc22d3	0.695	0.593	0.343	2.00E-45	2.90E-41	2
Fscn1	0.6631	0.996	0.855	4.60E-75	6.70E-71	2
Ccl22	0.6486	0.87	0.607	1.70E-51	2.50E-47	2
Ankrd33b	0.6299	0.847	0.564	7.50E-57	1.10E-52	2
Lyz1	2.0233	0.312	0.114	4.30E-31	6.20E-27	3
Mmp12	1.8648	0.374	0.011	1.50E-238	2.20E-234	3
H2-DMb2	1.5699	0.89	0.234	2.60E-224	3.90E-220	3
Il1b	1.538	0.851	0.282	1.30E-156	1.90E-152	3
H2-Ab1	1.522	1	0.863	1.20E-170	1.70E-166	3
Gm2a	1.5003	0.94	0.289	2.60E-219	3.80E-215	3
Cd209a	1.4702	0.333	0.022	1.50E-158	2.20E-154	3
H2-DMa	1.3199	0.976	0.434	1.90E-177	2.80E-173	3
H2-Eb1	1.2644	1	0.889	7.10E-159	1.00E-154	3
Cd74	1.2485	1	0.995	1.40E-174	2.00E-170	3
Cd1d1	1.2515	0.608	0.133	1.20E-142	1.80E-138	4
Glipr2	1.1335	0.873	0.438	1.50E-116	2.20E-112	4
Rnaset2a	1.102	0.654	0.346	1.30E-62	1.90E-58	4
Phf11b	0.9192	0.804	0.417	2.90E-91	4.20E-87	4
Gnl2	0.8176	0.728	0.408	2.80E-59	4.00E-55	4
Tubb5	0.8088	0.99	0.862	1.10E-98	1.50E-94	4
Socs2	0.7804	0.972	0.668	3.60E-87	5.30E-83	4
Isg15	0.7668	0.565	0.261	9.60E-46	1.40E-41	4
Cnn2	0.7533	0.919	0.692	1.30E-74	1.80E-70	4
Fabp5	0.7444	0.954	0.693	1.30E-65	1.90E-61	4

gene	avg_logFC	pct.1	pct.2	p_val	p_val_adj	cluster
Apoe	3.2821	0.599	0.174	8.40E-121	1.20E-116	5
Lyz2	3.0937	0.987	0.488	4.20E-228	6.20E-224	5
C1qb	2.7224	0.398	0.043	4.00E-151	5.90E-147	5
Plac8	2.6962	0.804	0.168	4.90E-222	7.20E-218	5
C1qa	2.6874	0.357	0.044	1.80E-122	2.60E-118	5
Ly6i	2.5799	0.829	0.041	0.00E+00	0.00E+00	5
Ifi27l2a	2.3491	0.895	0.234	4.90E-241	7.10E-237	5
Ifitm3	2.274	0.934	0.257	2.50E-238	3.70E-234	5
C1qc	2.2405	0.36	0.025	4.00E-170	5.90E-166	5
Ms4a6c	2.0391	0.98	0.163	0.00E+00	0.00E+00	5
Cd209d	1.6266	0.276	0.022	1.50E-83	2.20E-79	6
H2-DMb2	1.5878	0.88	0.273	5.70E-100	8.30E-96	6
Cd7	1.4582	0.411	0.036	3.40E-116	5.00E-112	6
Klrd1	1.3021	0.448	0.093	1.10E-59	1.60E-55	6
Lgals1	1.1425	0.724	0.534	6.20E-18	9.00E-14	6
Cd8a	1.0849	0.453	0.081	5.80E-65	8.40E-61	6
Atp1b1	1.0457	0.333	0.014	2.40E-150	3.50E-146	6
Gpr183	1.0352	0.771	0.22	1.20E-78	1.80E-74	6
Lag3	1.0148	0.458	0.071	8.50E-79	1.20E-74	6
H2-DMa	1.0089	0.932	0.468	7.80E-58	1.10E-53	6
Ppt1	2.4819	0.989	0.219	1.20E-183	1.80E-179	7
Naaa	2.2571	0.949	0.105	1.20E-260	1.70E-256	7
Xcr1	1.7113	0.876	0.01	0.00E+00	0.00E+00	7
Plbd1	1.6669	0.989	0.245	8.30E-148	1.20E-143	7
Cd8a	1.6579	0.921	0.061	0.00E+00	0.00E+00	7
Ifi205	1.5409	0.899	0.044	0.00E+00	0.00E+00	7
Ckb	1.4272	0.865	0.109	3.20E-191	4.60E-187	7
Cst3	1.4052	1	0.993	4.10E-87	6.00E-83	7
Psap	1.3847	0.994	0.888	3.10E-86	4.50E-82	7
Cxcl9	1.3386	0.747	0.074	1.10E-183	1.60E-179	7

Table 2.2 – relates to Figure 2.1. Top 10 DE genes between all myeloid clusters in mouse tdLN scRNA-Seq

DE was performed where every cluster was compared to all remaining cells. The top 10 DE genes for each cluster was selected and displayed in the Figure 2.1C and Supplementary Table 2. DE parameters: logfc.threshold = 0.4, min.pct = 0.25.

Table 2.3

gene	avg_logFC	pct.1	pct.2	p_val	p_val_adj	up in cluster
Ccl5	2.4898	0.996	0.951	1.2E-237	1.8E-233	mig
Epsti1	2.1779	0.97	0.686	2.7E-238	3.9E-234	mig
Fscn1	2.1234	0.985	0.556	1.2E-259	1.8E-255	mig
Ccl22	1.9804	0.764	0.271	1.1E-137	1.6E-133	mig
Tmem123	1.9144	0.995	0.681	6.1E-279	8.9E-275	mig
AW112010	1.8506	0.947	0.647	1.1E-211	1.6E-207	mig
Apol7c	1.7747	0.831	0.351	4.6E-146	6.8E-142	mig
Zmynd15	1.6995	0.766	0.21	1.4E-150	2.1E-146	mig
Socs2	1.5899	0.866	0.198	3.5E-205	5.1E-201	mig
Clu	1.5691	0.475	0.161	2.0E-55	2.9E-51	mig
Serpinb6b	1.5590	0.822	0.343	1.1E-146	1.6E-142	mig
Cacnb3	1.5470	0.88	0.218	5.6E-212	8.1E-208	mig
Samsn1	1.5230	0.961	0.4	2.8E-242	4.0E-238	mig
Anxa3	1.5110	0.957	0.366	1.1E-228	1.6E-224	mig
Nudt17	1.5007	0.859	0.239	1.8E-198	2.6E-194	mig
Cxcl1	1.4360	0.344	0.106	2.7E-35	3.9E-31	mig
Ccr7	1.4348	0.975	0.576	3.5E-196	5.0E-192	mig
Ccl17	1.4054	0.381	0.074	2.9E-50	4.2E-46	mig
Gadd45b	1.3783	0.922	0.533	8.3E-184	1.2E-179	mig
Crip1	1.3775	0.997	0.923	4.7E-211	6.8E-207	mig
Lgals3	-1.3272	0.455	0.849	1.7E-136	2.4E-132	res
Wfdc17	-1.3345	0.074	0.472	1.6E-155	2.3E-151	res
Ms4a6c	-1.3710	0.06	0.703	0.0E+00	0.0E+00	res
H2-Aa	-1.4673	0.925	1	6.2E-251	9.1E-247	res
Psap	-1.5084	0.866	0.965	1.2E-174	1.8E-170	res
Alox5ap	-1.5244	0.074	0.842	0.0E+00	0.0E+00	res
Naaa	-1.5248	0.034	0.518	2.1E-266	3.0E-262	res
Cd74	-1.5565	0.995	1	1.4E-271	2.0E-267	res
Mmp12	-1.5784	0.01	0.267	1.2E-151	1.7E-147	res
H2-DMb1	-1.5802	0.247	0.911	1.4E-299	2.1E-295	res
H2-Eb1	-1.6460	0.878	1	2.0E-264	3.0E-260	res
Ppt1	-1.6539	0.146	0.595	4.9E-152	7.1E-148	res
Ifitm3	-1.7392	0.172	0.697	5.9E-192	8.6E-188	res
H2-DMa	-1.7663	0.342	0.976	0.0E+00	0.0E+00	res
Plbd1	-1.8892	0.087	0.906	0.0E+00	0.0E+00	res
Il1b	-1.8961	0.195	0.77	1.1E-218	1.6E-214	res
Gm2a	-1.9321	0.171	0.951	0.0E+00	0.0E+00	res
H2-Ab1	-2.2566	0.841	1	5.8E-295	8.5E-291	res
Lyz1	-2.4575	0.059	0.274	3.1E-62	4.5E-58	res
Lyz2	-3.2636	0.419	0.844	1.6E-157	2.3E-153	res

Table 2.3 – relates to Figure 2.8. Top 20 DE genes between migratory and resident myeloid populations.

DE was performed where migratory clusters (0, 1, 2, 4, 6) were compared to resident clusters (3, 5, 7). The top 20 DE genes for each group was selected and displayed in

Supplementary Figure 2.1E and Supplementary Table 3. DE parameters:

logfc.threshold = 0.4, min.pct = 0.25.

Table 2.4

gene	avg_logFC	pct.1	pct.2	p_val	p_val_adj	up in cluster
Clu	1.7317	0.641	0.229	1.1E-53	1.6E-49	0
Ccl17	1.6774	0.584	0.198	8.7E-42	1.3E-37	0
Cxcl1	1.3876	0.407	0.163	1.8E-21	2.7E-17	0
Fxyd2	1.1307	0.548	0.265	3.4E-30	4.9E-26	0
mt-Nd1	1.0185	0.957	0.626	4.8E-80	7.0E-76	0
mt-Cytb	0.9925	0.968	0.73	1.8E-82	2.6E-78	0
mt-Co3	0.9129	0.995	0.913	1.5E-90	2.2E-86	0
H2-M2	0.8723	0.663	0.44	5.1E-23	7.4E-19	0
Rpl36a	0.8535	0.974	0.758	2.6E-88	3.8E-84	0
mt-Nd2	0.8523	0.798	0.392	5.3E-56	7.7E-52	0
mt-Nd4	0.8232	0.923	0.598	9.7E-62	1.4E-57	0
Slc7a11	0.8232	0.566	0.232	5.8E-30	8.5E-26	0
S100a10	0.8161	0.587	0.242	1.4E-33	2.0E-29	0
mt-Atp6	0.7962	1	0.957	3.5E-78	5.0E-74	0
mt-Co2	0.7784	0.996	0.885	4.7E-77	6.8E-73	0
Ccl22	0.7737	0.8	0.578	5.0E-24	7.2E-20	0
Rps17	0.7590	0.952	0.725	5.9E-71	8.6E-67	0
Mt1	0.7568	0.657	0.379	1.4E-25	2.0E-21	0
Vim	0.7401	0.952	0.84	9.3E-40	1.4E-35	0
Cxcl2	0.7337	0.3	0.132	9.3E-12	1.4E-07	0
Adam23	0.7209	0.603	0.198	5.5E-42	8.0E-38	0
Rps8	0.7128	0.989	0.916	6.5E-81	9.5E-77	0
Ltc4s	0.7021	0.689	0.318	4.0E-38	5.9E-34	0
Rps3a1	0.6963	0.998	0.959	1.9E-102	2.8E-98	0
Cstb	0.6916	0.904	0.784	1.2E-40	1.8E-36	0
Cd9	0.6756	0.656	0.305	1.1E-34	1.6E-30	0
Serpinb1a	0.6680	0.463	0.244	1.7E-15	2.4E-11	0
Rps18	0.6561	1	0.985	3.0E-105	4.4E-101	0
Rps29	0.6548	0.999	0.969	1.6E-98	2.3E-94	0
Rpl6	0.6464	0.992	0.929	4.6E-91	6.8E-87	0
Mif4gd	-0.6031	0.316	0.603	4.7E-33	6.9E-29	4
Eno3	-0.6091	0.753	0.903	7.6E-34	1.1E-29	4
Tagln2	-0.6210	0.765	0.908	3.5E-30	5.2E-26	4
Tuba1a	-0.6211	0.868	0.957	9.5E-44	1.4E-39	4
Dok1	-0.6307	0.57	0.835	4.8E-44	6.9E-40	4
Fscn1	-0.6310	0.985	0.995	1.0E-55	1.5E-51	4
Tap2	-0.6369	0.439	0.707	2.7E-36	3.9E-32	4
Ccnd1	-0.6383	0.205	0.42	3.5E-21	5.1E-17	4
Tubb5	-0.6641	0.907	0.99	3.6E-63	5.2E-59	4
Ccnd2	-0.6779	0.065	0.321	8.3E-40	1.2E-35	4
Phf11a	-0.6810	0.162	0.483	2.0E-42	2.9E-38	4
Vwa5a	-0.6886	0.255	0.511	5.6E-31	8.2E-27	4
Rcsd1	-0.6916	0.574	0.858	1.0E-50	1.5E-46	4
Ube2l6	-0.6939	0.697	0.858	6.1E-41	8.8E-37	4
Cnn2	-0.7014	0.718	0.919	1.3E-54	1.8E-50	4
Bcl2l14	-0.7050	0.127	0.417	1.3E-39	1.9E-35	4
Psmb9	-0.7079	0.876	0.98	2.1E-80	3.1E-76	4
Epsti1	-0.7142	0.971	0.99	3.7E-63	5.4E-59	4
Rnaset2b	-0.7610	0.121	0.427	2.1E-44	3.1E-40	4
Sp140	-0.7645	0.339	0.646	5.7E-44	8.2E-40	4

gene	avg_logFC	pct.1	pct.2	p_val	p_val_adj	up in cluster
Tap1	-0.8232	0.425	0.786	2.1E-63	3.0E-59	4
Ifitm3	-0.8706	0.15	0.514	1.4E-55	2.0E-51	4
Phf11b	-0.9062	0.41	0.804	1.3E-69	1.9E-65	4
Inpp5b	-0.9081	0.134	0.557	2.0E-74	3.0E-70	4
Isg15	-0.9561	0.216	0.565	2.1E-45	3.0E-41	4
Irf8	-0.9921	0.59	0.837	1.4E-50	2.0E-46	4
Cd1d1	-1.0065	0.213	0.608	1.2E-58	1.7E-54	4
Tnfrsf4	-1.0591	0.382	0.789	4.4E-68	6.4E-64	4
Glipr2	-1.1852	0.491	0.873	8.3E-90	1.2E-85	4
Rnaset2a	-1.2969	0.25	0.654	1.4E-69	2.1E-65	4

Table 2.4 – relates to Figure 2.1. Top 30 DE genes between mCD11b$^+$ cDC2 cluster 0 and 4.

DE was performed where CD11b$^+$ cDC2 cluster 0 was compared CD11b$^+$ cDC2 cluster 4. The top 30 DE genes for each group was selected and displayed in Figure 2.1D and Supplementary Table 4. DE parameters: logfc.threshold = 0.4, min.pct = 0.25.

Table 2.5

gene	avg_logFC	pct.1	pct.2	p_val	p_val_adj	cluster
Klf2	1.5021	0.759	0.38	1.1E-73	1.7E-69	mCD301b- tdLN
Fos	0.7575	0.712	0.513	7.4E-25	1.1E-20	mCD301b- tdLN
Eno3	0.7260	0.894	0.727	1.3E-45	1.9E-41	mCD301b- tdLN
Dusp2	0.6617	0.514	0.264	5.2E-21	7.8E-17	mCD301b- tdLN
Zmynd15	0.6497	0.755	0.577	7.5E-22	1.1E-17	mCD301b- tdLN
Ccl5	0.6393	1	0.999	2.5E-24	3.7E-20	mCD301b- tdLN
Apol7c	0.6309	0.774	0.607	2.2E-18	3.2E-14	mCD301b- tdLN
Cxcl1	0.6066	0.2	0.121	4.8E-06	7.1E-02	mCD301b- tdLN
Tmem176a	0.5765	0.998	0.977	4.7E-64	7.1E-60	mCD301b- tdLN
Etv3	0.5638	0.858	0.738	3.1E-40	4.6E-36	mCD301b- tdLN
Icosl	0.5620	0.441	0.208	1.2E-23	1.7E-19	mCD301b- tdLN
Klf6	0.5600	0.988	0.984	1.8E-42	2.7E-38	mCD301b- tdLN
Zfp36	0.5552	0.875	0.805	3.5E-29	5.3E-25	mCD301b- tdLN
Gnl2	0.5491	0.698	0.539	3.3E-22	5.0E-18	mCD301b- tdLN
Serinc3	0.5376	0.413	0.147	3.4E-33	5.0E-29	mCD301b- tdLN
Jund	0.5271	0.814	0.731	3.1E-26	4.6E-22	mCD301b- tdLN
Junb	0.5216	0.958	0.941	7.3E-30	1.1E-25	mCD301b- tdLN
Ppp1r15a	0.5207	0.896	0.763	3.2E-33	4.9E-29	mCD301b- tdLN
Cited2	0.5201	0.441	0.344	2.0E-18	3.0E-14	mCD301b- tdLN
Tspan3	0.5197	0.941	0.908	1.2E-26	1.8E-22	mCD301b- tdLN
Tmem176b	0.5169	0.993	0.988	2.6E-61	3.9E-57	mCD301b- tdLN
Jun	0.5157	0.873	0.825	5.0E-19	7.4E-15	mCD301b- tdLN
H3f3b	0.5020	1	0.999	6.9E-45	1.0E-40	mCD301b- tdLN
Fosb	0.4781	0.351	0.179	8.5E-20	1.3E-15	mCD301b- tdLN
Tnfrsf1b	0.4753	0.509	0.366	1.1E-28	1.6E-24	mCD301b- tdLN
Tbc1d4	0.4734	0.976	0.949	1.7E-34	2.5E-30	mCD301b- tdLN
Klf4	0.4693	0.377	0.243	6.8E-16	1.0E-11	mCD301b- tdLN
Tubb2a	0.4654	0.686	0.545	6.4E-19	9.6E-15	mCD301b- tdLN
Hist1h2bc	0.4648	0.491	0.406	4.1E-11	6.2E-07	mCD301b- tdLN
Pmaip1	0.4590	0.767	0.65	4.7E-19	7.0E-15	mCD301b- tdLN
Pygl	0.4589	0.392	0.181	3.5E-19	5.2E-15	mCD301b- tdLN
Nabp1	0.4562	0.488	0.329	1.9E-18	2.8E-14	mCD301b- tdLN
Tmem158	0.4561	0.222	0.042	1.0E-19	1.6E-15	mCD301b- tdLN
Tubb2b	0.4545	0.368	0.185	2.3E-12	3.5E-08	mCD301b- tdLN
Phf11a	0.4448	0.446	0.272	5.5E-17	8.2E-13	mCD301b- tdLN
Birc2	0.4432	0.858	0.795	4.2E-24	6.3E-20	mCD301b- tdLN
Lmo4	0.4319	0.264	0.072	4.6E-20	6.9E-16	mCD301b- tdLN
Rgs1	0.4314	0.96	0.957	6.3E-18	9.4E-14	mCD301b- tdLN
Malat1	0.4304	1	0.999	3.9E-44	5.8E-40	mCD301b- tdLN
Mxd1	0.4213	0.835	0.78	5.9E-20	8.8E-16	mCD301b- tdLN
H2-Q4	0.4170	0.868	0.789	1.6E-25	2.4E-21	mCD301b- tdLN
Ndnl2	0.4162	0.575	0.478	5.5E-18	8.3E-14	mCD301b- tdLN
Dusp1	0.4157	0.955	0.922	3.2E-18	4.8E-14	mCD301b- tdLN
Nmrk1	0.4156	0.406	0.223	2.1E-20	3.1E-16	mCD301b- tdLN
Phf11b	0.4153	0.785	0.699	6.3E-21	9.5E-17	mCD301b- tdLN
Rrad	0.4094	0.257	0.23	2.3E-15	3.4E-11	mCD301b- tdLN
Atf3	0.4087	0.417	0.318	1.3E-10	1.9E-06	mCD301b- tdLN
Tmem123	0.4025	1	0.999	6.6E-42	9.9E-38	mCD301b- tdLN
Ucp2	0.3998	0.731	0.64	1.2E-20	1.8E-16	mCD301b- tdLN
Spint2	0.3996	0.96	0.948	6.9E-31	1.0E-26	mCD301b- tdLN

gene	avg_logFC	pct.1	pct.2	p_val	p_val_adj	cluster
Slc38a2	0.3961	0.514	0.367	4.2E-18	6.3E-14	mCD301b- tdLN
Frmd4a	0.3918	0.509	0.382	5.6E-17	8.4E-13	mCD301b- tdLN
Skil	0.3907	0.469	0.305	1.6E-14	2.4E-10	mCD301b- tdLN
Bhlhe40	0.3828	0.726	0.679	1.7E-20	2.5E-16	mCD301b- tdLN
Rcsd1	0.3722	0.88	0.776	6.1E-18	9.1E-14	mCD301b- tdLN
Apol10b	0.3713	0.262	0.159	2.9E-17	4.3E-13	mCD301b- tdLN
Stard7	0.3657	0.491	0.335	1.4E-17	2.1E-13	mCD301b- tdLN
Ccnd1	0.3644	0.42	0.329	7.6E-09	1.1E-04	mCD301b- tdLN
Rgs2	0.3644	0.314	0.195	7.5E-12	1.1E-07	mCD301b- tdLN
Epsti1	0.3626	1	0.991	8.3E-20	1.2E-15	mCD301b- tdLN
H3f3a	0.3606	0.995	0.988	4.7E-28	7.1E-24	mCD301b- tdLN
Tnfrsf4	0.3594	0.785	0.695	1.5E-09	2.3E-05	mCD301b- tdLN
Pim1	0.3571	0.913	0.909	4.0E-18	5.9E-14	mCD301b- tdLN
Btg2	0.3528	0.601	0.499	9.4E-11	1.4E-06	mCD301b- tdLN
Tnfaip3	0.3464	0.568	0.499	1.2E-17	1.8E-13	mCD301b- tdLN
Ostf1	0.3437	0.981	0.99	4.5E-24	6.7E-20	mCD301b- tdLN
Csrnp1	0.3423	0.41	0.327	4.0E-20	6.0E-16	mCD301b- tdLN
Chka	0.3382	0.42	0.319	4.0E-11	6.0E-07	mCD301b- tdLN
Ankrd35	0.3377	0.368	0.253	2.1E-13	3.1E-09	mCD301b- tdLN
Plxnc1	0.3377	0.58	0.481	1.2E-18	1.8E-14	mCD301b- tdLN
Cd83	0.3376	0.91	0.922	3.6E-17	5.4E-13	mCD301b- tdLN
Tmem19	0.3331	0.521	0.445	9.4E-17	1.4E-12	mCD301b- tdLN
Fam53b	0.3309	0.524	0.389	9.2E-11	1.4E-06	mCD301b- tdLN
Kmt2e	0.3293	0.448	0.371	1.8E-18	2.7E-14	mCD301b- tdLN
Arhgap22	0.3276	0.597	0.53	2.8E-16	4.2E-12	mCD301b- tdLN
Kctd12	0.3263	0.311	0.207	8.2E-13	1.2E-08	mCD301b- tdLN
H2-K1	0.3241	1	1	4.0E-39	6.0E-35	mCD301b- tdLN
Zfp36l1	0.3220	0.955	0.942	6.1E-15	9.1E-11	mCD301b- tdLN
H2-D1	0.3212	1	1	4.9E-51	7.4E-47	mCD301b- tdLN
Creg1	0.3166	0.526	0.426	1.3E-11	1.9E-07	mCD301b- tdLN
Htra2	0.3142	0.764	0.74	1.4E-21	2.1E-17	mCD301b- tdLN
Il1b	0.3135	0.241	0.179	3.0E-04	1.0E+00	mCD301b- tdLN
Sec11c	0.3121	0.842	0.803	4.7E-14	7.0E-10	mCD301b- tdLN
Nfkbia	0.3119	0.995	0.996	4.2E-15	6.3E-11	mCD301b- tdLN
H2-Eb2	0.3097	0.283	0.165	1.6E-10	2.4E-06	mCD301b- tdLN
Bmp2k	0.3095	0.71	0.678	1.4E-16	2.1E-12	mCD301b- tdLN
Man1a	0.3085	0.363	0.23	5.0E-12	7.5E-08	mCD301b- tdLN
Rap2b	0.3055	0.783	0.73	2.4E-14	3.6E-10	mCD301b- tdLN
Laptm5	0.3046	0.767	0.718	4.0E-13	6.0E-09	mCD301b- tdLN
Cers6	0.3042	0.439	0.376	2.6E-16	3.9E-12	mCD301b- tdLN
Relb	0.3033	0.976	0.98	2.1E-20	3.1E-16	mCD301b- tdLN
Rassf4	0.3025	0.559	0.481	1.5E-13	2.2E-09	mCD301b- tdLN
Glipr1	0.3014	0.443	0.312	2.8E-10	4.2E-06	mCD301b- tdLN
Mthfsl	0.2972	0.71	0.636	2.8E-12	4.2E-08	mCD301b- tdLN
Ccl17	2.1187	0.798	0.248	2.4E-86	3.5E-82	mCD301b- DTR
Ccl22	1.3770	0.941	0.63	6.7E-72	1.0E-67	mCD301b- DTR
Ccl24	1.1418	0.202	0.002	2.2E-29	3.2E-25	mCD301b- DTR
Lgals1	1.0860	0.854	0.465	1.0E-67	1.5E-63	mCD301b- DTR
Cd1d2	0.9156	0.526	0.066	1.9E-63	2.8E-59	mCD301b- DTR
AA467197	0.8983	0.769	0.349	3.1E-55	4.6E-51	mCD301b- DTR
Gm13546	0.8761	0.539	0.12	3.8E-54	5.6E-50	mCD301b- DTR
Pkib	0.8452	0.432	0.087	1.6E-39	2.3E-35	mCD301b- DTR

gene	avg_logFC	pct.1	pct.2	p_val	p_val_adj	cluster
Ramp3	0.8316	0.705	0.321	2.1E-45	3.2E-41	mCD301b- DTR
Cytip	0.7920	0.84	0.465	1.0E-52	1.5E-48	mCD301b- DTR
S100a10	0.7663	0.61	0.29	2.0E-28	3.0E-24	mCD301b- DTR
Ccnd2	0.7045	0.607	0.323	2.5E-24	3.8E-20	mCD301b- DTR
Capg	0.6362	0.519	0.196	4.6E-30	6.9E-26	mCD301b- DTR
Rps27l	0.6274	0.994	0.95	2.7E-53	4.0E-49	mCD301b- DTR
Fabp5	0.6111	0.978	0.955	3.7E-25	5.6E-21	mCD301b- DTR
Slc27a3	0.5627	0.311	0.042	2.1E-30	3.1E-26	mCD301b- DTR
Cst3	0.5446	1	0.995	9.8E-44	1.5E-39	mCD301b- DTR
Tnip3	0.5392	0.512	0.193	1.3E-25	2.0E-21	mCD301b- DTR
Vim	0.5335	0.952	0.856	1.4E-17	2.2E-13	mCD301b- DTR
Stat4	0.5055	0.595	0.283	1.7E-24	2.5E-20	mCD301b- DTR
Amica1	0.4985	0.353	0.075	5.1E-28	7.6E-24	mCD301b- DTR
Cd86	0.4835	0.809	0.517	2.1E-24	3.2E-20	mCD301b- DTR
Cnn3	0.4734	0.473	0.165	6.1E-27	9.1E-23	mCD301b- DTR
Gsn	0.4592	0.366	0.108	1.5E-21	2.3E-17	mCD301b- DTR
H2afy	0.4539	0.772	0.436	2.9E-29	4.3E-25	mCD301b- DTR
Got1	0.4445	0.409	0.156	1.3E-18	1.9E-14	mCD301b- DTR
Ptpn1	0.4438	0.639	0.349	5.5E-25	8.2E-21	mCD301b- DTR
Cd302	0.4429	0.406	0.151	3.8E-20	5.7E-16	mCD301b- DTR
Pdcd1lg2	0.4404	0.506	0.191	4.6E-25	6.9E-21	mCD301b- DTR
Plgrkt	0.4396	0.676	0.41	3.1E-20	4.7E-16	mCD301b- DTR
Serpinb6b	0.4262	0.981	0.908	9.2E-25	1.4E-20	mCD301b- DTR
Rps6	0.4028	0.997	0.988	1.2E-35	1.8E-31	mCD301b- DTR
Tyms	0.4027	0.353	0.064	6.3E-30	9.4E-26	mCD301b- DTR
Serpinb1a	0.3920	0.403	0.283	2.6E-04	1.0E+00	mCD301b- DTR
Glipr2	0.3903	0.965	0.875	9.9E-20	1.5E-15	mCD301b- DTR
Stat1	0.3889	0.788	0.517	7.3E-21	1.1E-16	mCD301b- DTR
Tspo	0.3887	0.994	0.969	2.7E-27	4.0E-23	mCD301b- DTR
Mkrn1	0.3865	0.675	0.382	1.9E-21	2.8E-17	mCD301b- DTR
Gapdh	0.3813	0.951	0.844	1.3E-18	1.9E-14	mCD301b- DTR
Coro1a	0.3805	0.837	0.632	5.2E-16	7.8E-12	mCD301b- DTR
Fkbp1a	0.3764	0.611	0.344	8.2E-19	1.2E-14	mCD301b- DTR
Selm	0.3737	0.665	0.491	5.7E-08	8.6E-04	mCD301b- DTR
Myl12a	0.3625	0.961	0.92	8.6E-17	1.3E-12	mCD301b- DTR
Rps11	0.3612	1	0.998	5.1E-55	7.7E-51	mCD301b- DTR
Rps4x	0.3597	0.997	0.96	1.4E-29	2.0E-25	mCD301b- DTR
H2-DMa	0.3597	0.655	0.429	3.1E-12	4.6E-08	mCD301b- DTR
Psma6	0.3591	0.866	0.71	8.4E-18	1.3E-13	mCD301b- DTR
Txn1	0.3563	0.978	0.917	2.3E-16	3.5E-12	mCD301b- DTR
Nostrin	0.3558	0.772	0.524	2.7E-17	4.0E-13	mCD301b- DTR
Acot7	0.3555	0.458	0.205	8.2E-17	1.2E-12	mCD301b- DTR
Lyz2	0.3503	0.608	0.384	7.0E-13	1.0E-08	mCD301b- DTR
Syngr2	0.3494	0.991	0.965	1.6E-21	2.4E-17	mCD301b- DTR
Actg1	0.3483	1	1	1.2E-36	1.9E-32	mCD301b- DTR
Lcp1	0.3477	0.829	0.653	1.1E-13	1.7E-09	mCD301b- DTR
Rpl12	0.3447	0.873	0.684	4.1E-17	6.1E-13	mCD301b- DTR
Rab8b	0.3442	0.738	0.493	4.7E-16	7.0E-12	mCD301b- DTR
Lactb	0.3440	0.764	0.542	7.4E-15	1.1E-10	mCD301b- DTR
Ehd1	0.3408	0.506	0.267	3.9E-14	5.9E-10	mCD301b- DTR
Procr	0.3356	0.382	0.16	3.9E-14	5.9E-10	mCD301b- DTR
Lgals3	0.3335	0.655	0.453	1.9E-11	2.9E-07	mCD301b- DTR

gene	avg_logFC	pct.1	pct.2	p_val	p_val_adj	cluster
Cd9	0.3330	0.587	0.354	7.9E-13	1.2E-08	mCD301b- DTR
Slc25a3	0.3318	0.876	0.703	2.0E-17	3.0E-13	mCD301b- DTR
Rpl10a	0.3314	0.939	0.854	1.4E-14	2.0E-10	mCD301b- DTR
Clta	0.3307	0.962	0.87	6.9E-18	1.0E-13	mCD301b- DTR
S100a6	0.3307	0.962	0.875	3.1E-15	4.7E-11	mCD301b- DTR
Serpina3g	0.3298	0.543	0.302	2.5E-14	3.7E-10	mCD301b- DTR
Eno1	0.3287	0.519	0.271	1.3E-15	2.0E-11	mCD301b- DTR
Tnfaip8	0.3280	0.682	0.448	4.7E-14	7.0E-10	mCD301b- DTR
Lrrc58	0.3278	0.91	0.764	3.3E-16	4.9E-12	mCD301b- DTR
Gpx1	0.3258	0.835	0.608	3.4E-16	5.0E-12	mCD301b- DTR
Zbp1	0.3254	0.457	0.219	6.9E-15	1.0E-10	mCD301b- DTR
Gdi2	0.3244	0.883	0.708	3.9E-17	5.8E-13	mCD301b- DTR
Cfl1	0.3232	0.994	0.955	1.3E-19	1.9E-15	mCD301b- DTR
Srgn	0.3225	1	0.991	4.9E-25	7.3E-21	mCD301b- DTR
Rab14	0.3221	0.832	0.59	1.6E-18	2.4E-14	mCD301b- DTR
Glrx	0.3215	0.62	0.389	1.0E-12	1.5E-08	mCD301b- DTR
Eva1b	0.3184	0.592	0.356	1.7E-13	2.5E-09	mCD301b- DTR
Cd80	0.3120	0.402	0.203	7.1E-12	1.1E-07	mCD301b- DTR
Prps1	0.3090	0.289	0.101	2.3E-17	3.4E-13	mCD301b- DTR
Tspan13	0.3078	0.658	0.432	1.4E-12	2.1E-08	mCD301b- DTR
Rpl10	0.3076	1	0.976	3.5E-28	5.3E-24	mCD301b- DTR
Rps8	0.3045	0.965	0.915	5.8E-15	8.7E-11	mCD301b- DTR
Rps17	0.3029	0.883	0.731	4.5E-13	6.8E-09	mCD301b- DTR
Arpc1b	0.3010	0.996	0.965	1.1E-23	1.7E-19	mCD301b- DTR
Cxcl1	1.3860	0.437	0.162	3.8E-56	5.6E-52	mCD301b+ tdLN
Klf2	1.2722	0.785	0.406	3.3E-111	4.9E-107	mCD301b+ tdLN
Fxyd2	0.9176	0.577	0.294	2.1E-57	3.2E-53	mCD301b+ tdLN
Clu	0.7647	0.684	0.513	5.9E-34	8.8E-30	mCD301b+ tdLN
Tmem158	0.6672	0.346	0.109	2.0E-43	3.0E-39	mCD301b+ tdLN
Tspan3	0.6556	0.938	0.836	2.0E-68	3.0E-64	mCD301b+ tdLN
Fos	0.6494	0.842	0.683	1.2E-38	1.8E-34	mCD301b+ tdLN
Dusp2	0.6481	0.526	0.277	6.3E-35	9.5E-31	mCD301b+ tdLN
Glipr1	0.6254	0.692	0.414	4.6E-65	6.8E-61	mCD301b+ tdLN
Apol7c	0.6138	0.87	0.698	2.6E-51	3.9E-47	mCD301b+ tdLN
Fosb	0.6039	0.535	0.291	1.8E-42	2.7E-38	mCD301b+ tdLN
Eno3	0.5701	0.714	0.526	1.2E-48	1.7E-44	mCD301b+ tdLN
Atf3	0.5360	0.635	0.394	1.0E-35	1.5E-31	mCD301b+ tdLN
Mfge8	0.5262	0.431	0.279	3.0E-21	4.5E-17	mCD301b+ tdLN
Ppp1r15a	0.5217	0.854	0.753	1.1E-55	1.6E-51	mCD301b+ tdLN
H2-M2	0.5135	0.669	0.598	5.0E-21	7.5E-17	mCD301b+ tdLN
Gnl2	0.4904	0.525	0.31	4.1E-32	6.1E-28	mCD301b+ tdLN
Bhlhe40	0.4848	0.715	0.574	2.5E-37	3.7E-33	mCD301b+ tdLN
Creg1	0.4590	0.608	0.4	1.8E-36	2.6E-32	mCD301b+ tdLN
Il4i1	0.4543	0.863	0.837	6.1E-38	9.0E-34	mCD301b+ tdLN
Cxcl2	0.4524	0.314	0.17	6.4E-13	9.6E-09	mCD301b+ tdLN
Etv3	0.4512	0.914	0.805	2.4E-47	3.5E-43	mCD301b+ tdLN
Tnfaip3	0.4505	0.69	0.539	8.9E-36	1.3E-31	mCD301b+ tdLN
Hspa1a	0.4471	0.264	0.137	2.8E-13	4.3E-09	mCD301b+ tdLN
Rap2b	0.4451	0.769	0.657	1.5E-43	2.2E-39	mCD301b+ tdLN
Junb	0.4414	0.954	0.939	4.1E-43	6.1E-39	mCD301b+ tdLN
Tubb2a	0.4342	0.521	0.338	1.8E-28	2.7E-24	mCD301b+ tdLN
Lmo4	0.4320	0.382	0.199	8.2E-27	1.2E-22	mCD301b+ tdLN

gene	avg_logFC	pct.1	pct.2	p_val	p_val_adj	cluster
Ier2	0.4314	0.545	0.37	3.2E-21	4.7E-17	mCD301b+ tdLN
M1ap	0.4239	0.388	0.205	6.9E-26	1.0E-21	mCD301b+ tdLN
Ehf	0.4237	0.371	0.163	2.5E-28	3.7E-24	mCD301b+ tdLN
Cdc42ep3	0.4220	0.732	0.674	3.2E-31	4.8E-27	mCD301b+ tdLN
Tmem176b	0.4191	0.981	0.962	3.6E-67	5.4E-63	mCD301b+ tdLN
Pvr	0.4168	0.468	0.265	6.4E-30	9.6E-26	mCD301b+ tdLN
2610528A11Rik	0.4156	0.138	0.046	3.7E-13	5.6E-09	mCD301b+ tdLN
Evi2a	0.4144	0.326	0.129	3.2E-33	4.8E-29	mCD301b+ tdLN
Tmem176a	0.4122	0.971	0.936	6.0E-56	8.9E-52	mCD301b+ tdLN
Rgs2	0.4069	0.388	0.217	2.9E-20	4.3E-16	mCD301b+ tdLN
Jund	0.4031	0.874	0.818	3.7E-33	5.5E-29	mCD301b+ tdLN
Cited2	0.4021	0.479	0.353	8.3E-18	1.2E-13	mCD301b+ tdLN
Skil	0.4015	0.532	0.352	6.1E-28	9.2E-24	mCD301b+ tdLN
Cd44	0.3958	0.767	0.662	2.3E-29	3.4E-25	mCD301b+ tdLN
Jun	0.3954	0.776	0.715	2.4E-16	3.6E-12	mCD301b+ tdLN
Hist1h1c	0.3933	0.532	0.412	3.4E-18	5.1E-14	mCD301b+ tdLN
Egr1	0.3927	0.229	0.069	5.3E-23	8.0E-19	mCD301b+ tdLN
Gpr183	0.3881	0.311	0.171	3.7E-15	5.5E-11	mCD301b+ tdLN
Nfkbia	0.3849	0.99	0.988	4.8E-28	7.1E-24	mCD301b+ tdLN
Klf4	0.3773	0.435	0.271	1.1E-17	1.7E-13	mCD301b+ tdLN
Tubb6	0.3725	0.4	0.267	6.5E-25	9.8E-21	mCD301b+ tdLN
Nfkbiz	0.3702	0.593	0.469	7.8E-23	1.2E-18	mCD301b+ tdLN
Rrad	0.3659	0.349	0.242	1.1E-10	1.7E-06	mCD301b+ tdLN
Klf6	0.3643	0.957	0.941	1.6E-25	2.4E-21	mCD301b+ tdLN
Ccl9	0.3629	0.275	0.154	1.1E-11	1.7E-07	mCD301b+ tdLN
Hist1h2bc	0.3625	0.632	0.506	8.0E-14	1.2E-09	mCD301b+ tdLN
Ucp2	0.3613	0.793	0.714	1.1E-35	1.6E-31	mCD301b+ tdLN
Cd83	0.3581	0.875	0.867	2.4E-28	3.6E-24	mCD301b+ tdLN
Mycbp2	0.3573	0.706	0.565	2.4E-26	3.6E-22	mCD301b+ tdLN
Sat1	0.3566	0.915	0.861	2.0E-30	3.0E-26	mCD301b+ tdLN
Gm10116	0.3564	0.594	0.449	8.6E-31	1.3E-26	mCD301b+ tdLN
Rhob	0.3546	0.328	0.149	4.8E-23	7.2E-19	mCD301b+ tdLN
Ftl1	0.3539	0.999	1	1.4E-43	2.1E-39	mCD301b+ tdLN
Pmaip1	0.3498	0.803	0.689	3.2E-19	4.8E-15	mCD301b+ tdLN
Basp1	0.3408	0.864	0.812	3.2E-29	4.8E-25	mCD301b+ tdLN
Zfp36	0.3382	0.903	0.857	8.4E-25	1.3E-20	mCD301b+ tdLN
Fgl2	0.3321	0.408	0.286	2.0E-15	3.0E-11	mCD301b+ tdLN
Lmna	0.3315	0.391	0.25	5.1E-21	7.6E-17	mCD301b+ tdLN
Vcam1	0.3265	0.286	0.136	3.8E-19	5.7E-15	mCD301b+ tdLN
Tnf	0.3255	0.208	0.081	4.7E-18	7.1E-14	mCD301b+ tdLN
Zeb2	0.3235	0.455	0.328	9.8E-20	1.5E-15	mCD301b+ tdLN
Galnt12	0.3229	0.421	0.255	1.4E-22	2.2E-18	mCD301b+ tdLN
Birc2	0.3175	0.834	0.787	4.8E-25	7.1E-21	mCD301b+ tdLN
Ostf1	0.3163	0.942	0.942	6.3E-32	9.4E-28	mCD301b+ tdLN
Brk1	0.3143	0.926	0.912	2.8E-29	4.2E-25	mCD301b+ tdLN
Adm	0.3135	0.215	0.091	6.0E-20	9.0E-16	mCD301b+ tdLN
Vrk2	0.3076	0.411	0.274	1.8E-19	2.8E-15	mCD301b+ tdLN
Anxa3	0.3066	0.976	0.968	3.1E-37	4.6E-33	mCD301b+ tdLN
Dkkl1	0.3040	0.229	0.071	4.0E-25	6.0E-21	mCD301b+ tdLN
Adgre4	0.3017	0.159	0.016	1.6E-32	2.4E-28	mCD301b+ tdLN
Il1b	0.3017	0.27	0.227	1.6E-04	1.0E+00	mCD301b+ tdLN
Ptgs2	0.3012	0.325	0.198	2.7E-09	4.0E-05	mCD301b+ tdLN

gene	avg_logFC	pct.1	pct.2	p_val	p_val_adj	cluster
Rps3a1	0.3010	0.998	1	2.2E-53	3.3E-49	mCD301b+ tdLN
Tmem123	0.3001	0.998	0.995	7.0E-34	1.1E-29	mCD301b+ tdLN
Gm13546	1.3265	0.653	0.11	8.2E-164	1.2E-159	mCD301b+ DTR
Ccl17	1.1178	0.792	0.637	4.2E-40	6.3E-36	mCD301b+ DTR
Pkib	1.0191	0.449	0.063	1.1E-93	1.7E-89	mCD301b+ DTR
Ramp3	0.9060	0.509	0.12	2.4E-82	3.6E-78	mCD301b+ DTR
Cst3	0.8259	0.999	0.999	6.0E-82	8.9E-78	mCD301b+ DTR
Gyg	0.8185	0.829	0.58	1.6E-68	2.4E-64	mCD301b+ DTR
Glipr2	0.8113	0.788	0.505	9.8E-84	1.5E-79	mCD301b+ DTR
AA467197	0.7371	0.486	0.212	7.1E-46	1.1E-41	mCD301b+ DTR
Txndc17	0.7205	0.947	0.816	1.7E-84	2.5E-80	mCD301b+ DTR
Cytip	0.7171	0.893	0.61	3.7E-90	5.6E-86	mCD301b+ DTR
Stat1	0.6552	0.706	0.367	1.3E-68	1.9E-64	mCD301b+ DTR
Bcl2l14	0.6154	0.421	0.137	1.9E-48	2.8E-44	mCD301b+ DTR
Ccl22	0.5922	0.922	0.778	2.6E-37	3.8E-33	mCD301b+ DTR
Slc27a3	0.5748	0.323	0.057	1.4E-55	2.1E-51	mCD301b+ DTR
Clta	0.5565	0.931	0.828	1.1E-73	1.6E-69	mCD301b+ DTR
Stat4	0.5362	0.391	0.095	1.3E-52	1.9E-48	mCD301b+ DTR
Serpinb6b	0.5220	0.923	0.781	4.4E-42	6.6E-38	mCD301b+ DTR
Got1	0.5161	0.443	0.177	8.2E-48	1.2E-43	mCD301b+ DTR
Cd86	0.5121	0.523	0.269	2.4E-37	3.6E-33	mCD301b+ DTR
Pdcd1lg2	0.4999	0.367	0.084	3.9E-54	5.8E-50	mCD301b+ DTR
Rps27l	0.4585	0.977	0.959	7.8E-52	1.2E-47	mCD301b+ DTR
Syngr2	0.4536	0.976	0.896	7.0E-64	1.0E-59	mCD301b+ DTR
Plgrkt	0.4482	0.597	0.349	2.8E-37	4.2E-33	mCD301b+ DTR
Ccnd2	0.4410	0.215	0.056	4.9E-28	7.4E-24	mCD301b+ DTR
Tspo	0.4360	0.976	0.936	1.1E-44	1.7E-40	mCD301b+ DTR
Actg1	0.4239	1	0.989	2.2E-50	3.3E-46	mCD301b+ DTR
Cmc2	0.4229	0.407	0.185	2.6E-28	3.9E-24	mCD301b+ DTR
Ndrg1	0.4087	0.463	0.244	4.1E-25	6.2E-21	mCD301b+ DTR
Rab8b	0.4077	0.685	0.455	6.3E-32	9.5E-28	mCD301b+ DTR
Selm	0.4049	0.626	0.5	4.1E-13	6.1E-09	mCD301b+ DTR
Irf8	0.4034	0.765	0.648	6.7E-18	1.0E-13	mCD301b+ DTR
Lgals1	0.4004	0.658	0.579	5.1E-22	7.7E-18	mCD301b+ DTR
Lcp1	0.3991	0.737	0.542	1.0E-27	1.6E-23	mCD301b+ DTR
Gdi2	0.3987	0.856	0.668	2.5E-39	3.8E-35	mCD301b+ DTR
Cd80	0.3964	0.326	0.095	1.6E-35	2.4E-31	mCD301b+ DTR
Zfand6	0.3959	0.875	0.748	1.7E-37	2.5E-33	mCD301b+ DTR
Ncoa7	0.3844	0.421	0.209	8.1E-27	1.2E-22	mCD301b+ DTR
Lactb	0.3835	0.574	0.347	1.2E-29	1.8E-25	mCD301b+ DTR
Il7r	0.3805	0.453	0.248	1.2E-26	1.7E-22	mCD301b+ DTR
Ptpn1	0.3785	0.442	0.213	5.2E-29	7.8E-25	mCD301b+ DTR
Serpinb9	0.3770	0.846	0.712	6.6E-24	9.8E-20	mCD301b+ DTR
Crem	0.3695	0.255	0.059	1.0E-32	1.6E-28	mCD301b+ DTR
Pmvk	0.3618	0.615	0.412	3.4E-23	5.2E-19	mCD301b+ DTR
Calm1	0.3605	0.997	0.997	5.2E-35	7.8E-31	mCD301b+ DTR
Txn1	0.3591	0.943	0.878	1.8E-27	2.7E-23	mCD301b+ DTR
Amica1	0.3543	0.292	0.087	8.1E-31	1.2E-26	mCD301b+ DTR
Serpina3g	0.3438	0.33	0.13	4.4E-26	6.6E-22	mCD301b+ DTR
Rab14	0.3435	0.755	0.559	1.2E-27	1.8E-23	mCD301b+ DTR
Mif4gd	0.3379	0.524	0.299	2.4E-24	3.6E-20	mCD301b+ DTR
Tspan13	0.3313	0.615	0.426	4.3E-21	6.4E-17	mCD301b+ DTR

gene	avg_logFC	pct.1	pct.2	p_val	p_val_adj	cluster
Adprh	0.3298	0.434	0.201	9.6E-28	1.4E-23	mCD301b+ DTR
Lyz2	0.3228	0.597	0.449	4.3E-10	6.4E-06	mCD301b+ DTR
S100a6	0.3193	0.952	0.896	3.7E-22	5.5E-18	mCD301b+ DTR
Nt5c	0.3176	0.647	0.435	2.1E-23	3.1E-19	mCD301b+ DTR
Capg	0.3176	0.628	0.432	1.4E-20	2.2E-16	mCD301b+ DTR
Slamf1	0.3162	0.333	0.152	7.2E-21	1.1E-16	mCD301b+ DTR
Cd302	0.3159	0.292	0.134	2.9E-20	4.4E-16	mCD301b+ DTR
Myl6	0.3157	0.986	0.981	2.6E-24	3.9E-20	mCD301b+ DTR
Rac1	0.3135	0.87	0.739	1.1E-26	1.6E-22	mCD301b+ DTR
Lrrfip1	0.3126	0.436	0.246	1.0E-20	1.5E-16	mCD301b+ DTR
Akap9	0.3125	0.486	0.296	1.9E-19	2.9E-15	mCD301b+ DTR
Tpm4	0.3093	0.767	0.612	3.4E-20	5.1E-16	mCD301b+ DTR
Cd274	0.3074	0.658	0.423	4.6E-24	6.8E-20	mCD301b+ DTR
Dnajc12	0.3058	0.345	0.145	8.5E-24	1.3E-19	mCD301b+ DTR
Fabp5	0.3056	0.958	0.937	1.8E-12	2.6E-08	mCD301b+ DTR
Mrpl13	0.3035	0.431	0.246	2.0E-19	3.0E-15	mCD301b+ DTR
Cd200	0.3032	0.418	0.24	4.8E-16	7.2E-12	mCD301b+ DTR
Ywhah	0.3011	0.77	0.603	2.9E-22	4.3E-18	mCD301b+ DTR
Coro1a	0.3005	0.656	0.497	1.7E-15	2.5E-11	mCD301b+ DTR

Table 2.5 – relates to Figure 2.4. DE between mCD301b^{-} and mCD301b^{+} in control and *Foxp3*^{DTR} tdLN.

DE was performed where either mCD301b^{-} or mCD301b^{+} from control tdLN and Foxp3DTR tdLN were compared. Volcano plot in Figure 2.4D displayed all DE genes but highlighted genes with log *N* fold change >0.4. Supplementary Table 5 lists all DE genes with log *N* fold change > 0.3. DE parameters: min.pct = 0.1.

Table 2.6

gene	avg_logFC	pct.1	pct.2	p_val	p_val_adj	cluster
FCER1A	1.4134	0.839	0.243	6.7E-121	1.2E-116	0
CD1C	1.1697	0.766	0.2	1.2E-120	2.1E-116	0
CLEC10A	1.1260	0.917	0.546	5.5E-90	9.5E-86	0
CD1E	0.9994	0.64	0.177	4.0E-82	6.9E-78	0
LGALS2	0.8471	0.967	0.567	1.6E-85	2.7E-81	0
AREG	0.8340	0.937	0.788	2.8E-46	4.9E-42	0
CFP	0.8269	0.94	0.508	1.4E-94	2.5E-90	0
NDRG2	0.7004	0.829	0.297	2.9E-105	5.1E-101	0
JAML	0.6790	0.995	0.867	4.0E-93	6.9E-89	0
LTB	0.6416	0.748	0.494	4.8E-34	8.3E-30	0
CXCL10	1.5549	0.494	0.196	4.1E-36	7.2E-32	1
S100A8	1.3196	0.736	0.537	2.2E-26	3.9E-22	1
S100A9	1.0608	0.907	0.789	1.7E-26	2.9E-22	1
VAMP5	0.9384	0.902	0.655	1.7E-73	2.9E-69	1
TIMP1	0.9195	0.928	0.881	8.6E-27	1.5E-22	1
CXCL9	0.9069	0.39	0.16	9.1E-27	1.6E-22	1
GBP1	0.9015	0.783	0.471	1.1E-52	2.0E-48	1
FCN1	0.8446	0.744	0.479	1.8E-30	3.2E-26	1
VCAN	0.8344	0.486	0.277	2.2E-18	3.9E-14	1
STAT1	0.7899	0.879	0.577	1.4E-65	2.4E-61	1
CXCL2	0.5477	0.507	0.39	1.3E-08	2.3E-04	2
PHACTR1	0.5477	0.899	0.68	2.1E-42	3.6E-38	2
AREG	0.5328	0.896	0.802	1.0E-17	1.8E-13	2
LYZ	0.5173	1	0.986	1.6E-49	2.9E-45	2
THBD	0.5119	0.738	0.469	1.9E-32	3.4E-28	2
HES1	0.5019	0.447	0.206	5.1E-24	8.9E-20	2
RGS2	0.4688	0.992	0.932	7.3E-31	1.3E-26	2
ZNF331	0.4607	0.872	0.695	1.9E-25	3.3E-21	2
OSM	0.4513	0.523	0.359	4.1E-13	7.1E-09	2
HBEGF	0.4399	0.796	0.565	5.5E-25	9.6E-21	2
APOE	2.2950	0.996	0.61	4.2E-122	7.3E-118	3
RNASE1	1.9069	0.773	0.328	4.4E-64	7.7E-60	3
APOC1	1.8721	0.992	0.518	1.3E-113	2.3E-109	3
SEPP1	1.8631	0.909	0.326	3.5E-104	6.2E-100	3
IFI27	1.8423	0.657	0.185	9.7E-70	1.7E-65	3
C1QB	1.7300	1	0.782	1.3E-111	2.2E-107	3
FOLR2	1.6111	0.913	0.264	4.9E-123	8.5E-119	3
C1QA	1.5937	1	0.806	5.4E-109	9.4E-105	3
PLTP	1.5914	0.938	0.284	2.6E-129	4.6E-125	3
HAMP	1.5868	0.756	0.179	2.9E-96	5.1E-92	3
SPP1	2.3263	0.826	0.457	1.1E-41	2.0E-37	4
NUPR1	1.8168	0.584	0.168	4.7E-43	8.3E-39	4
GPNMB	1.4000	0.842	0.259	3.3E-63	5.7E-59	4
HSPB1	1.2162	0.853	0.651	7.8E-11	1.4E-06	4
HSPA1A	1.1509	0.705	0.463	5.5E-13	9.7E-09	4
PLIN2	1.0907	0.789	0.518	5.2E-18	9.1E-14	4
RNASE1	1.0631	0.9	0.328	5.9E-64	1.0E-59	4
LGALS1	0.9891	1	0.956	8.1E-32	1.4E-27	4
BNIP3	0.9039	0.505	0.144	1.1E-37	1.9E-33	4
CSTB	0.8899	0.989	0.946	8.3E-15	1.4E-10	4

gene	avg_logFC	pct.1	pct.2	p_val	p_val_adj	cluster
CLEC9A	1.8351	0.941	0.03	4.8E-237	8.4E-233	5
IDO1	1.7890	0.971	0.192	4.7E-96	8.3E-92	5
CPNE3	1.6050	1	0.423	2.2E-70	3.9E-66	5
DNASE1L3	1.5903	0.951	0.328	4.3E-59	7.4E-55	5
SNX3	1.4938	1	0.919	3.8E-58	6.7E-54	5
HIST1H4C	1.4578	0.784	0.451	5.3E-14	9.2E-10	5
C1orf54	1.2818	0.98	0.524	4.5E-55	7.9E-51	5
S100B	1.2652	0.745	0.391	1.8E-21	3.1E-17	5
IRF8	1.2457	0.98	0.664	6.4E-52	1.1E-47	5
LGALS2	1.2163	0.98	0.639	1.3E-41	2.3E-37	5
CCR7	3.0469	0.96	0.05	5.0E-84	8.8E-80	6
BIRC3	2.7268	1	0.532	1.6E-19	2.8E-15	6
CCL19	2.6507	0.88	0.065	8.6E-58	1.5E-53	6
MARCKSL1	2.5294	1	0.515	1.2E-19	2.0E-15	6
FSCN1	2.4204	0.96	0.211	1.0E-28	1.8E-24	6
CRIP1	2.1336	1	0.592	4.6E-17	8.0E-13	6
EBI3	2.0899	0.8	0.176	1.5E-20	2.5E-16	6
TXN	1.9230	1	0.829	6.4E-16	1.1E-11	6
IDO1	1.8681	0.8	0.23	1.9E-15	3.4E-11	6
IL7R	1.6540	0.92	0.039	2.0E-90	3.5E-86	6

Table 2.6 – relates to Figure 2.6. Top 10 DE genes between all myeloid clusters in human tdLN scRNA-Seq.

DE was performed where every cluster was compared to all remaining cells. The top 10 DE genes for each cluster was selected and displayed in the Figure 2.6B and Supplementary Table 6. DE parameters: logfc.threshold = 0.4, min.pct = 0.25.

Table 2.7

gene	avg_logFC	pct.1	pct.2	p_val	p_val_adj	cluster
DDIT4	0.3954	0.911	0.765	1.0E-09	1.8E-05	0.1
CORO1A	0.3129	1	0.978	2.3E-14	4.0E-10	0.1
LIMD2	0.2937	0.975	0.933	9.0E-11	1.6E-06	0.1
GYPC	0.2925	0.519	0.287	1.4E-07	2.4E-03	0.1
HINT1	0.2829	1	0.974	1.0E-11	1.8E-07	0.1
CRIP1	0.2788	0.924	0.81	8.2E-07	1.4E-02	0.1
ACTB	0.2742	1	1	3.7E-14	6.4E-10	0.1
PDLIM1	0.2706	0.424	0.142	5.3E-12	9.2E-08	0.1
SRSF2	0.2626	0.981	0.888	5.7E-09	9.9E-05	0.1
GSTP1	0.2543	1	0.993	8.2E-13	1.4E-08	0.1
SEPT6	0.2464	0.797	0.634	3.3E-07	5.8E-03	0.1
SRSF3	0.2443	0.994	0.929	1.3E-07	2.2E-03	0.1
ANXA6	0.2413	0.734	0.593	1.7E-06	2.9E-02	0.1
HNRNPK	0.2365	1	0.963	1.2E-08	2.0E-04	0.1
CXCR4	0.2345	1	0.974	1.5E-06	2.5E-02	0.1
COTL1	0.2301	1	0.996	4.9E-08	8.6E-04	0.1
ACTG1	0.2273	1	1	4.8E-10	8.3E-06	0.1
MYL12A	0.2230	1	0.996	5.5E-09	9.6E-05	0.1
HLA-DOB	0.2205	0.449	0.235	7.5E-07	1.3E-02	0.1
SNX3	0.2198	0.981	0.937	2.1E-06	3.7E-02	0.1
PRELID1	0.2186	1	0.963	2.0E-06	3.5E-02	0.1
CAP1	0.2132	0.994	0.948	1.0E-06	1.8E-02	0.1
RPSA	0.1942	1	1	1.5E-12	2.6E-08	0.1
SYTL1	0.1874	0.399	0.183	3.4E-07	6.0E-03	0.1
NPM1	0.1868	1	1	7.3E-07	1.3E-02	0.1
GDI2	0.1866	0.981	0.966	2.8E-07	4.9E-03	0.1
PFN1	0.1831	1	1	5.8E-10	1.0E-05	0.1
LSP1	0.1711	1	0.993	8.2E-07	1.4E-02	0.1
GAPDH	0.1674	1	1	4.5E-07	7.8E-03	0.1
RPL10A	0.1618	1	1	1.9E-12	3.2E-08	0.1
HNRNPA2B1	0.1564	1	0.985	1.3E-06	2.3E-02	0.1
RPL8	0.1562	1	1	5.1E-13	8.8E-09	0.1
RPL5	0.1560	1	1	7.9E-10	1.4E-05	0.1
RPS17	0.1513	1	1	3.1E-11	5.3E-07	0.1
C14orf2	0.1467	1	0.974	2.7E-06	4.6E-02	0.1
RPS5	0.1448	1	1	2.7E-10	4.7E-06	0.1
RPS23	0.1334	1	1	4.9E-10	8.5E-06	0.1
NACA	0.1310	1	1	2.8E-06	4.8E-02	0.1
RPS18	0.1261	1	1	1.8E-09	3.2E-05	0.1
RPS3	0.1243	1	1	3.5E-10	6.2E-06	0.1
RPS3A	0.1234	1	1	3.4E-09	5.9E-05	0.1
RPL9	0.1215	1	1	1.6E-07	2.7E-03	0.1
RPL18A	0.1208	1	1	7.0E-10	1.2E-05	0.1
RPL18	0.1186	1	1	5.7E-08	9.9E-04	0.1
RPS7	0.1179	1	1	3.7E-08	6.4E-04	0.1
RPS13	0.1173	1	1	1.6E-08	2.8E-04	0.1
RPL7A	0.1146	1	1	1.2E-06	2.2E-02	0.1
RPL19	0.1110	1	1	1.1E-07	1.9E-03	0.1
RPS2	0.1101	1	1	1.7E-06	2.9E-02	0.1
RPS6	0.1075	1	1	6.0E-08	1.0E-03	0.1

gene	avg_logFC	pct.1	pct.2	p_val	p_val_adj	cluster
RPL13A	0.1048	1	1	1.1E-06	1.9E-02	0.1
RPS11	0.1041	1	1	2.2E-06	3.8E-02	0.1
RPS15	0.1004	1	1	5.7E-07	9.9E-03	0.1
DNASE1L3	1.5074	0.752	0.346	1.6E-22	2.8E-18	0.2
CCL4L2	1.2087	0.664	0.329	1.2E-14	2.2E-10	0.2
C1QA	1.0690	0.861	0.702	3.1E-16	5.4E-12	0.2
HLA-DQB2	1.0322	0.628	0.135	5.1E-27	9.0E-23	0.2
CD1E	0.9392	0.861	0.529	2.7E-21	4.7E-17	0.2
CCL3L3	0.9381	0.708	0.37	3.4E-13	6.0E-09	0.2
C1QB	0.8877	0.839	0.647	1.4E-12	2.4E-08	0.2
C1QC	0.8721	0.642	0.46	9.2E-08	1.6E-03	0.2
CCL4	0.7649	0.562	0.239	1.4E-11	2.4E-07	0.2
MT2A	0.6880	0.81	0.564	7.4E-10	1.3E-05	0.2
CCL3	0.6767	0.723	0.554	9.9E-07	1.7E-02	0.2
S100B	0.6617	0.562	0.27	9.4E-10	1.6E-05	0.2
CXCL8	0.6254	0.62	0.384	1.5E-06	2.5E-02	0.2
IDO1	0.6155	0.46	0.17	9.5E-11	1.7E-06	0.2
STAT1	0.5936	0.715	0.346	1.1E-16	1.9E-12	0.2
ACP5	0.5706	0.759	0.256	1.0E-24	1.8E-20	0.2
GBP1	0.5565	0.708	0.408	1.1E-11	1.8E-07	0.2
TMEM176B	0.5429	0.467	0.235	3.3E-08	5.8E-04	0.2
IFITM3	0.5387	0.978	0.772	4.2E-13	7.3E-09	0.2
CD1B	0.5358	0.423	0.128	1.5E-12	2.7E-08	0.2
FAM26F	0.5056	0.978	0.927	9.7E-17	1.7E-12	0.2
CD68	0.4581	0.927	0.779	2.7E-13	4.7E-09	0.2
PLA2G7	0.4254	0.635	0.356	3.8E-09	6.6E-05	0.2
TUBB	0.4107	0.876	0.772	4.2E-07	7.3E-03	0.2
LGALS2	0.4084	1	0.955	1.6E-13	2.9E-09	0.2
GSN	0.4023	0.993	0.979	4.8E-13	8.4E-09	0.2
HLA-DQA2	0.3966	0.277	0.035	6.5E-14	1.1E-09	0.2
CLEC10A	0.3903	0.978	0.896	1.8E-09	3.2E-05	0.2
EGR2	0.3857	0.409	0.125	2.8E-11	4.9E-07	0.2
SERPINF1	0.3671	0.759	0.433	7.2E-11	1.3E-06	0.2
RGS10	0.3538	0.985	0.948	2.6E-13	4.5E-09	0.2
PLEKHO1	0.3524	0.876	0.678	4.2E-08	7.3E-04	0.2
PTMS	0.3417	0.73	0.429	3.5E-10	6.1E-06	0.2
C1orf54	0.3397	0.526	0.26	5.6E-09	9.8E-05	0.2
NAP1L1	0.3375	1	0.99	2.0E-14	3.4E-10	0.2
HCAR2	0.3337	0.474	0.173	1.8E-10	3.1E-06	0.2
MMP9	0.3315	0.255	0.076	3.4E-07	5.9E-03	0.2
FTL	0.3141	1	1	1.6E-07	2.7E-03	0.2
HLA-DQB1	0.3001	1	1	9.7E-17	1.7E-12	0.2
NPC2	0.2953	0.993	0.983	2.6E-09	4.5E-05	0.2
HLA-DPB1	0.2845	1	1	2.3E-15	4.0E-11	0.2
ENPP2	0.2837	0.584	0.263	3.3E-10	5.8E-06	0.2
ITM2B	0.2813	1	1	1.3E-09	2.3E-05	0.2
FGL2	0.2746	0.985	0.99	1.1E-06	1.9E-02	0.2
SLAMF7	0.2738	0.555	0.263	8.7E-09	1.5E-04	0.2
HLA-DRB5	0.2732	1	1	1.0E-20	1.8E-16	0.2
SLAMF8	0.2723	0.701	0.405	2.9E-08	5.1E-04	0.2
CD63	0.2691	0.985	0.962	3.2E-07	5.6E-03	0.2
LGALS3BP	0.2657	0.474	0.173	5.1E-11	8.9E-07	0.2

gene	avg_logFC	pct.1	pct.2	p_val	p_val_adj	cluster
NINJ1	0.2656	0.606	0.346	1.7E-06	2.9E-02	0.2
PNRC1	0.2606	0.964	0.952	5.3E-07	9.3E-03	0.2
PILRA	0.2601	0.788	0.564	3.4E-07	5.9E-03	0.2
TMEM176A	0.2544	0.372	0.135	2.2E-08	3.9E-04	0.2
GBP4	0.2505	0.613	0.367	1.6E-06	2.9E-02	0.2
FRMD4B	0.2484	0.613	0.325	6.7E-08	1.2E-03	0.2
HLA-DQA1	0.2368	1	1	4.6E-12	8.0E-08	0.2
HLA-DRA	0.2352	1	1	1.9E-20	3.3E-16	0.2
CST3	0.2165	1	1	2.2E-09	3.9E-05	0.2
PVRL2	0.2145	0.584	0.336	1.0E-06	1.8E-02	0.2
GPR34	0.2130	0.409	0.149	1.2E-08	2.1E-04	0.2
LPAR6	0.2120	0.489	0.225	3.4E-07	5.9E-03	0.2
HLA-DRB1	0.2115	1	1	7.9E-14	1.4E-09	0.2
HLA-DPA1	0.2097	1	1	2.6E-12	4.5E-08	0.2
HLA-E	0.2032	0.985	0.99	2.6E-06	4.5E-02	0.2
CD74	0.2006	1	1	7.8E-20	1.4E-15	0.2
CPVL	0.1980	1	0.993	2.3E-06	4.0E-02	0.2
TYROBP	0.1941	1	0.997	2.4E-06	4.3E-02	0.2
TPT1	0.1813	1	1	1.6E-11	2.9E-07	0.2
B2M	0.1775	1	1	5.2E-09	9.1E-05	0.2
IL6ST	0.1770	0.38	0.138	6.9E-08	1.2E-03	0.2
HLA-DMB	0.1709	0.993	1	1.5E-06	2.6E-02	0.2
SERPING1	0.1649	0.314	0.114	1.2E-06	2.2E-02	0.2
ELAVL4	0.1300	0.27	0.083	4.6E-07	7.9E-03	0.2
FCGR1B	0.1282	0.328	0.121	2.3E-06	4.0E-02	0.2
FCN1	1.1242	0.679	0.342	4.4E-18	7.7E-14	0.3
S100A9	1.0495	0.779	0.559	1.2E-14	2.0E-10	0.3
FCER1A	0.9011	0.924	0.803	2.5E-13	4.4E-09	0.3
S100A4	0.8120	0.992	0.915	3.7E-24	6.5E-20	0.3
S100A8	0.7891	0.489	0.298	5.1E-07	8.9E-03	0.3
CD14	0.6979	0.893	0.631	1.2E-17	2.1E-13	0.3
TSPO	0.6136	0.977	0.722	7.6E-23	1.3E-18	0.3
HBEGF	0.5721	0.763	0.492	3.4E-12	6.0E-08	0.3
VCAN	0.5464	0.412	0.071	2.5E-19	4.3E-15	0.3
S100A6	0.5026	1	0.98	2.0E-16	3.5E-12	0.3
FCGR2A	0.3600	0.679	0.529	1.2E-08	2.1E-04	0.3
SAMSN1	0.3526	0.779	0.603	2.3E-07	3.9E-03	0.3
RHOB	0.3499	0.595	0.414	2.1E-06	3.6E-02	0.3
ID3	0.3399	0.298	0.085	1.0E-08	1.8E-04	0.3
CAPG	0.3327	0.878	0.851	2.0E-07	3.4E-03	0.3
NUP214	0.3248	0.481	0.186	8.7E-12	1.5E-07	0.3
TGIF1	0.3215	0.656	0.481	2.7E-06	4.6E-02	0.3
NAMPT	0.3153	0.954	0.888	3.1E-08	5.4E-04	0.3
SERPINA1	0.3059	0.962	0.908	1.3E-08	2.3E-04	0.3
CD1D	0.3042	0.763	0.624	1.6E-07	2.7E-03	0.3
FCGRT	0.2945	0.992	0.973	5.8E-10	1.0E-05	0.3
NEAT1	0.2937	1	0.993	8.3E-09	1.4E-04	0.3
CTSS	0.2906	1	0.997	1.9E-10	3.3E-06	0.3
NPC2	0.2903	0.985	0.986	2.8E-09	4.8E-05	0.3
LY96	0.2894	0.779	0.634	2.5E-07	4.4E-03	0.3
HNMT	0.2870	0.55	0.305	5.1E-08	9.0E-04	0.3
TKT	0.2779	0.931	0.939	1.8E-06	3.1E-02	0.3

gene	avg_logFC	pct.1	pct.2	p_val	p_val_adj	cluster
F13A1	0.2660	0.344	0.125	1.3E-08	2.2E-04	0.3
SLC11A1	0.2518	0.328	0.122	3.3E-08	5.7E-04	0.3
MT-ND3	0.2388	0.992	1	1.2E-07	2.2E-03	0.3
PSAP	0.2281	1	0.997	5.9E-07	1.0E-02	0.3
FCER1G	0.2226	1	0.997	3.8E-08	6.7E-04	0.3
LAPTM5	0.2193	0.992	0.993	1.2E-08	2.0E-04	0.3
MT-ND2	0.2174	1	0.997	2.0E-08	3.6E-04	0.3
SNCA	0.2147	0.336	0.105	1.2E-09	2.1E-05	0.3
CD2	0.2134	0.412	0.2	5.3E-07	9.2E-03	0.3
CD300E	0.2122	0.305	0.125	6.4E-07	1.1E-02	0.3
TYROBP	0.2107	1	0.997	5.8E-10	1.0E-05	0.3
S100A12	0.2042	0.252	0.054	2.1E-09	3.6E-05	0.3
AIF1	0.2010	0.992	1	1.7E-06	3.0E-02	0.3
FTL	0.1999	1	1	6.9E-10	1.2E-05	0.3
MT-CO3	0.1877	0.992	1	2.4E-06	4.1E-02	0.3
MT-ND1	0.1858	0.992	0.997	2.1E-06	3.6E-02	0.3
H3F3A	0.1427	1	1	6.1E-08	1.1E-03	0.3

Table 2.7 – relates to Figure 2.6. DE genes between BDCA-1^{+} cDC2 clusters

DE was performed where BDCA-1+ cDC2 clusters 0.1, 0.2 and 0.3 were compared to one another. All DE genes above the logFC threshold are displayed in Figure 2.6D as heatmap and in Supplementary Table 7. DE parameters: logfc.threshold = 0.1, min.pct = 0.25.

Table 2.8 Key reagents and resources

REAGENT or RESOURCE	SOURCE	IDENTIFIER
Antibodies		
Anti-mouse CD11c BV650 (clone N418)	Biolegend	117339
anti-mouse/human CD11b BV605 (clone M1/70)	Biolegend	101257
anti-mouse CD103 BV421 (clone 2E7)	Biolegend	121421
anti-mouse Ly-6C BV711 (clone HK1.4)	Biolegend	128037
anti-mouse CD90.2 BV785 (clone 30-H12)	Biolegend	105331
anti-mouse/human CD45R/B220 BV785 (clone RA3-6B2)	Biolegend	103246
anti-mouse Ly-6G BV785 (clone IA8)	Biolegend	127645
anti-mouse Siglec F BV786 (clone E50-2440)	BD Biosciences	740956
anti-mouse NK1.1 BV785 (clone PK136)	Biolegend	108749
anti-mouse CD24 PE/Cy7 (clone M1/69)	Biolegend	101822
anti-mouse MHC-II AF700 (clone M5/114.15.2)	Biolegend	107622
anti-mouse CD301b PE or APC (clone URA-1)	Biolegend	146814, 146803
anti-mouse CD8a PerCP/Cy5.5 or PE/Cy7 (clone 53-6.7)	Biolegend	100734, 100722
anti-mouse F4/80 FITC (clone BM8)	Biolegend	123107
anti-mouse CD45 PerCP/Cy5.5 (clone A20)	Biolegend	110727
anti-mouse CD197/CCR7 PE	Biolegend	120105
anti-mouse CD9 AF647 (clone MZ3)	Biolegend	124809
anti-mouse CD135/FLT3 PE (clone A2F10)	Biolegend	135305
anti-mouse CD172a/SIRPA PE (clone P84)	Biolegend	144011
anti-mouse CD273/PDL2 PE (clone TY25)	Biolegend	107205
anti-mouse CD14 PE (clone Sa14-2)	Biolegend	123309
anti-mouse CD16/32 PE (clone 93)	Biolegend	101307
anti-mouse CD200R PE (clone OX110)	Biolegend	123907
anti-mouse CD206 PE (clone C068C2)	Biolegend	141705
anti-mouse CD4 BUV395 (clone GK1.5)	BD Biosciences	563790
anti-mouse/rat/human CD278/ICOS APC (clone C398.4A)	Biolegend	313510
anti-mouse CD279/PD-1 PE (clone RMP1-14)	Biolegend	114118
anti-mouse/human CD44 BV711 (clone IM7)	Biolegend	103057
anti-mouse CD69 BV650 (clone H1.2F3)	Biolegend	104541
anti-mouse Foxp3 eF450 (clone FJK-16s)	Thermo Fisher	48-5773-82
anti-mouse/rat/human Foxp3 AF647 (clone 150D)	Biolegend	320014
anti-mouse IL-4 PE (clone 11B11)	Biolegend	504104
anti-mouse IL-17a BV421 (clone TC11-18H10.1)	Biolegend	506926
anti-mouse IFNg PE/Cy7 (clone XMG1.2)	Biolegend	505825
anti-mouse/human T-bet BV605 (clone 4B10)	Biolegend	644817
anti-human CD45 APC/e780 (clone HI30)	Thermo Fisher	47-0459-42
anti-human CD3e PerCP/e710 (clone OKT3)	Thermo Fisher	46-0037-42
anti-human HLA-DR BUV395 (clone G46-6)	BD Biosciences	564040
anti-human CD56 BUV737 (clone NCAM16.2)	BD Biosciences	564448
anti-human CD4 PE/Dazzle 594 (clone S3.5)	Biolegend	100455
anti-human CD8a BV605 (clone RPA-T8)	Biolegend	301039
anti-human CD127 BV650 (clone HIL-7R-M21)	BD Biosciences	563225

REAGENT or RESOURCE	SOURCE	IDENTIFIER
Antibodies		
anti-human CD38 AF700 (clone HIT2)	Biolegend	303523
anti-human CD25 APC (clone 2A3)	BD Biosciences	340939
anti-human CD45RO PE (clone UCHL1)	BD Biosciences	561889
anti-human PD-1 BV786 (clone EH12)	BD Biosciences	563789
anti-human ICOS BV711 (clone DX29)	BD Biosciences	563833
anti-human FoxP3 PE/Cy7 (clone 236A/E7)	Thermo Fisher	25-4777-41
anti-human CTLA-4 BV421 (clone BNI3)	BD Biosciences	565931
anti-human/mouse/rat Ki67 AF488 (clone SolA15)	Thermo Fisher	11-5698-82
anti-human CD19 PerCP/e710 (clone H1B19)	Thermo Fisher	45-0199-42
anti-human CD20 PerCP/e710 (clone 2H7)	Thermo Fisher	45-0209-42
anti-human CD56 PerCP/e710 (clone CMSSB)	Thermo Fisher	46-0567-42
anti-human CD64 BUV737 (clone 10.1)	BD Biosciences	564425
anti-human CD11c AF700 (clone 3.9)	Thermo Fisher	56-0116-42
anti-human CD16 BV605 (clone 3G8)	Biolegend	302039
anti-human CD273/PDL2 BV650 (clone MIH18)	BD Biosciences	563844
anti-human/mouse TREM2 APC (clone 237920)	R&D Systems	FAB17291A
anti-human CD304 PE (clone 12C2)	Biolegend	354503
anti-human CD1C/BDCA-1 PE/Cy7 (clone L161)	Biolegend	331515
anti-human CD197 BV421 (clone G043H7)	Biolegend	353207
anti-human BDCA-3 FITC (clone AD5-14H12)	Miltenyi	130-098-843
anti-human PDL1 BV786 (clone MIH1)	BD Biosciences	563739
anti-human CD14 BV711 (clone M5E2)	Biolegend	301837
PE Rat IgG2a, k Isotype Ctrl Antibody (clone RTK2758)	Biolegend	400508
PE Rat IgG1, k Isotype Ctrl Antibody (clone RTK2071)	Biolegend	400408
APC Armenian Hamster IgG Isotype Ctrl Antibody (clone HTK888)	Biolegend	400912
BV605 Mouse IgG1, k Isotype Ctrl Antibody (clone MOPC-21)	Biolegend	400162
BV421 Mouse IgG2a, k Isotype Ctrl Antibody (clone MOPC-173)	Biolegend	400259
anti-mouse CD4 InVivoMab (clone GK1.5)	BioXCell	BE0003-1
anti-mouse CD8 InVivoMab (clone 2.43)	BioXCell	BE0061
anti-mouse CTLA-4 (CD152) InVivoMab (clone 9H10)	BioXCell	BE0131
Rat IgG2b, k InVivoMab	BioXCell	BE0090
Polyclonal Syrian hamster IgG InVivoMab	BioXCell	BE0087
anti-mouse CD16/32 InVivoMab	BioXCell	BE0307
Normal Rat Serum	Thermo Fisher	10710C
Armenian Hamster Serum	Innovative Research	IGHMA-SER
Biological Samples		
Human tumor samples	UC San Francisco	IRB # 13-12246 and 14-15342
Mouse tissue samples (LN, tumor)	UC San Francisco	IACUC: AN170208

REAGENT or RESOURCE	SOURCE	IDENTIFIER
Chemicals, Peptides, and Recombinant Proteins		
Matrigel GFR, Phenol-red free	Corning	356231
Collagenase, Type I	Worthington Biochemical	LS004197
Collagenase, Type IV	Worthington Biochemical	LS004189
DNAse I	Roche	10104159001
Liberase TL	Roche	5401020001
Human TruStain FcX	Biolegend	422302
Zombie Aqua Fixable Viability Kit	Biolegend	423102
Zombie NIR Fixable Viability Kit	Biolegend	423106
Brilliant Stain Buffer Plus	BD Biosciences	566385
Brefeldin A (BFA)	Sigma-Aldrich	B7651
Phorbol 12-myristate 13-acetate (PMA)	Sigma-Aldrich	P8139
Ionomycin	Invitrogen	I24222
Monensin Solution (1000X)	Thermo Fisher	00-4505-51
Diphtheria Toxin (unnicked)	List Biological Laboratories	150
FTY720	Cayman Chemical Company	10006292
eBioscience™ Cell Proliferation Dye eFluor™ 670		65-0840-85
Ovalbumin Endofit	Invivogen	Vac-pova
OVA peptide (323-339)	Genscript	RP10610-1
Critical Commercial Assays		
Chromium Single Cell 3' Library & Gel Bead Kit V2	10X Genomics	120237
BD Cytofix	BD Biosciences	554655
Foxp3/Transcription factor staining buffer set	Thermo Fisher	00-5523-00
EasySep Mouse $CD4^+$ T Cell Isolation kit	STEMCELL Technologies	19852
Deposited Data		
GEO XXXXXX		
Experimental Models: Cell Lines		
B16-F10	ATCC	CRL-6475
B16-ChOVA	UC San Francisco	N/A
B78-ChOVA	UC San Francisco	N/A
B16-GM-CSF	UC San Francisco	N/A
B16-ZsGreen	UC San Francisco	N/A
Experimental Models: Organisms/Strains		
Mouse: C57BL/6J	The Jackson Laboratory	000664
Mouse: B6 CD45.1 (B6.SJL-$Ptprc^a$ $Pepc^b$/BoyJ)	The Jackson Laboratory	002014

REAGENT or RESOURCE	SOURCE	IDENTIFIER
Experimental Models: Organisms/Strains		
Mouse: OT-II (B6.Cg-Tg(TcraTcrb)425Cbn/J	The Jackson Laboratory	004194
Mouse: *Irf4 fl/fl (*B6.129S1-*Irf4tm1Rdf*/J)	The Jackson Laboratory	009380
Experimental Models: Organisms/Strains		
Mouse: *ActB-Cre* (FVB/N-*Tmem163*$^{Tg(ACTB-cre)2Mrt}$/J)	The Jackson Laboratory	003376
Mouse: *CD11c-Cre* (B6.Cg-Tg(Itgax-cre)1-1Reiz/J)	The Jackson Laboratory	008068
Mouse: *Cx3cr1*^{iDTR} (B6N.129P2-*Cx3cr1*$^{tm3(DTR)Litt}$/J)	The Jackson Laboratory	025629
Mouse: *Ccr7-/-* (B6.129P2(C)-*Ccr7*^{tm1Rfor}/J)	The Jackson Laboratory	006621
Mouse: *Zbtb46*^{GFP} *(*B6.129S6(C)-*Zbtb46*$^{tm1.1Kmm}$/J)	The Jackson Laboratory	027618
Mouse: *Foxp3*^{DTR} *(*B6.129(Cg)-*Foxp3*$^{tm3(DTR/GFP)Ayr}$/J)	The Jackson Laboratory	016958
Mouse: *Xcr1*^{DTR} *(*Xcr1$^{tm2(HBEGF/Venus)Ksho}$)	Tsuneyasu Kaisho, Osaka University	
Software and Algorithms		
CellRanger 2.0	10X Genomics	10xgenomics.com
STAR	Dobin et.al. 2013	code.google.com/p/rna-star/.
Seurat	Satija et al. 2015	satijalab.org/seurat/
R: The Project for Statistical Computing		r-project.org

REFERENCES

1. Topalian, S.L., Drake, C.G. & Pardoll, D.M. Immune checkpoint blockade: a common denominator approach to cancer therapy. *Cancer Cell* **27**, 450-461 (2015).
2. Kawamura, S.*, et al.* Identification of a Human Clonogenic Progenitor with Strict Monocyte Differentiation Potential: A Counterpart of Mouse cMoPs. *Immunity* **46**, 835-848.e834 (2017).
3. Hettinger, J.*, et al.* Origin of monocytes and macrophages in a committed progenitor. *Nat Immunol* **14**, 821-830 (2013).
4. Serbina, N.V. & Pamer, E.G. Monocyte emigration from bone marrow during bacterial infection requires signals mediated by chemokine receptor CCR2. *Nat Immunol* **7**, 311-317 (2006).
5. Shi, C. & Pamer, E.G. Monocyte recruitment during infection and inflammation. *Nat Rev Immunol* **11**, 762-774 (2011).
6. Jakubzick, C.V., Randolph, G.J. & Henson, P.M. Monocyte differentiation and antigen-presenting functions. *Nat Rev Immunol* **17**, 349-362 (2017).
7. Ginhoux, F. & Jung, S. Monocytes and macrophages: developmental pathways and tissue homeostasis. *Nat Rev Immunol* **14**, 392-404 (2014).
8. Jakubzick, C.*, et al.* Minimal differentiation of classical monocytes as they survey steady-state tissues and transport antigen to lymph nodes. *Immunity* **39**, 599-610 (2013).

9. Holmgaard, R.B.*, et al.* Tumor-Expressed IDO Recruits and Activates MDSCs in a Treg-Dependent Manner. *Cell reports* **13**, 412-424 (2015).
10. Rodriguez, P.C.*, et al.* Arginase I in myeloid suppressor cells is induced by COX-2 in lung carcinoma. *The Journal of experimental medicine* **202**, 931-939 (2005).
11. Donkor, M.K.*, et al.* Mammary tumor heterogeneity in the expansion of myeloid-derived suppressor cells. *International immunopharmacology* **9**, 937-948 (2009).
12. Mao, Y.*, et al.* Melanoma-educated CD14+ cells acquire a myeloid-derived suppressor cell phenotype through COX-2-dependent mechanisms. *Cancer Res* **73**, 3877-3887 (2013).
13. Lu, T.*, et al.* Tumor-infiltrating myeloid cells induce tumor cell resistance to cytotoxic T cells in mice. *The Journal of clinical investigation* **121**, 4015-4029 (2011).
14. Headley, M.B.*, et al.* Visualization of immediate immune responses to pioneer metastatic cells in the lung. *Nature* **531**, 513-517 (2016).
15. Auffray, C.*, et al.* Monitoring of blood vessels and tissues by a population of monocytes with patrolling behavior. *Science (New York, N.Y.)* **317**, 666-670 (2007).
16. Carlin, L.M.*, et al.* Nr4a1-dependent Ly6C(low) monocytes monitor endothelial cells and orchestrate their disposal. *Cell* **153**, 362-375 (2013).
17. Hanna, R.N.*, et al.* Patrolling monocytes control tumor metastasis to the lung. *Science (New York, N.Y.)* **350**, 985-990 (2015).

18. Broz, M.L.*, et al.* Dissecting the tumor myeloid compartment reveals rare activating antigen-presenting cells critical for T cell immunity. *Cancer Cell* **26**, 638-652 (2014).

19. Mantovani, A., Biswas, S.K., Galdiero, M.R., Sica, A. & Locati, M. Macrophage plasticity and polarization in tissue repair and remodelling. *The Journal of pathology* **229**, 176-185 (2013).

20. Noy, R. & Pollard, J.W. Tumor-associated macrophages: from mechanisms to therapy. *Immunity* **41**, 49-61 (2014).

21. Gautier, E.L.*, et al.* Gene-expression profiles and transcriptional regulatory pathways that underlie the identity and diversity of mouse tissue macrophages. *Nat Immunol* **13**, 1118-1128 (2012).

22. Zhu, Y.*, et al.* Tissue-Resident Macrophages in Pancreatic Ductal Adenocarcinoma Originate from Embryonic Hematopoiesis and Promote Tumor Progression. *Immunity* **47**, 323-338.e326 (2017).

23. Franklin, R.A.*, et al.* The cellular and molecular origin of tumor-associated macrophages. *Science (New York, N.Y.)* **344**, 921-925 (2014).

24. Murray, P.J.*, et al.* Macrophage Activation and Polarization: Nomenclature and Experimental Guidelines. *Immunity* **41**, 14-20 (2014).

25. Mantovani, A.*, et al.* The chemokine system in diverse forms of macrophage activation and polarization. *Trends Immunol.* **25**, 677-686 (2004).

26. Mills, C.D., Kincaid, K., Alt, J.M., Heilman, M.J. & Hill, A.M. M-1/M-2 macrophages and the Th1/Th2 paradigm. *Journal of immunology (Baltimore, Md. : 1950)* **164**, 6166-6173 (2000).

27. Gunderson, A.J.*, et al.* Bruton Tyrosine Kinase-Dependent Immune Cell Cross-talk Drives Pancreas Cancer. *Cancer discovery* **6**, 270-285 (2016).

28. Kaneda, M.M.*, et al.* PI3Kγ is a molecular switch that controls immune suppression. *Nature* **539**, 437-442 (2016).

29. Daley, D.*, et al.* Dectin 1 activation on macrophages by galectin 9 promotes pancreatic carcinoma and peritumoral immune tolerance. *Nature medicine* **23**, 556-567 (2017).

30. Lieschke, G.J.*, et al.* Mice lacking granulocyte colony-stimulating factor have chronic neutropenia, granulocyte and macrophage progenitor cell deficiency, and impaired neutrophil mobilization. *Blood* **84**, 1737-1746 (1994).

31. Wculek, S.K. & Malanchi, I. Neutrophils support lung colonization of metastasis-initiating breast cancer cells. *Nature* **528**, 413-417 (2015).

32. Nywening, T.M.*, et al.* Targeting tumour-associated macrophages with CCR2 inhibition in combination with FOLFIRINOX in patients with borderline resectable and locally advanced pancreatic cancer: a single-centre, open-label, dose-finding, non-randomised, phase 1b trial. *The Lancet Oncology* **17**, 651-662 (2016).

33. Coffelt, S.B.*, et al.* IL-17-producing γδ T cells and neutrophils conspire to promote breast cancer metastasis. *Nature* **522**, 345-348 (2015).

34. Casbon, A.-J.*, et al.* Invasive breast cancer reprograms early myeloid differentiation in the bone marrow to generate immunosuppressive neutrophils. *Proceedings of the National Academy of Sciences of the United States of America* **112**, E566-575 (2015).

35. Fridlender, Z.G.*, et al.* Polarization of tumor-associated neutrophil phenotype by TGF-beta: "N1" versus "N2" TAN. *Cancer Cell* **16**, 183-194 (2009).

36. Ho, A.S.*, et al.* Neutrophil elastase as a diagnostic marker and therapeutic target in colorectal cancers. *Oncotarget* **5**, 473-480 (2014).

37. Merad, M., Sathe, P., Helft, J., Miller, J. & Mortha, A. The dendritic cell lineage: ontogeny and function of dendritic cells and their subsets in the steady state and the inflamed setting. *Annual review of immunology* **31**, 563-604 (2013).

38. Nakano, H., Lyons-Cohen, M.R., Whitehead, G.S., Nakano, K. & Cook, D.N. Distinct functions of CXCR4, CCR2, and CX3CR1 direct dendritic cell precursors from the bone marrow to the lung. *Journal of leukocyte biology* **101**, 1143-1153 (2017).

39. Schlitzer, A.*, et al.* Identification of cDC1- and cDC2-committed DC progenitors reveals early lineage priming at the common DC progenitor stage in the bone marrow. *Nat Immunol* **16**, 718-728 (2015).

40. Chen, D.S. & Mellman, I. Oncology meets immunology: the cancer-immunity cycle. *Immunity* **39**, 1-10 (2013).

41. Edelson, B.T.*, et al.* Peripheral CD103+ dendritic cells form a unified subset developmentally related to CD8alpha+ conventional dendritic cells. *The Journal of experimental medicine* **207**, 823-836 (2010).

42. Hildner, K.*, et al.* Batf3 deficiency reveals a critical role for CD8alpha+ dendritic cells in cytotoxic T cell immunity. *Science (New York, N.Y.)* **322**, 1097-1100 (2008).

43. Schiavoni, G.*, et al.* ICSBP is essential for the development of mouse type I interferon-producing cells and for the generation and activation of CD8alpha(+) dendritic cells. *The Journal of experimental medicine* **196**, 1415-1425 (2002).

44. Hacker, C.*, et al.* Transcriptional profiling identifies Id2 function in dendritic cell development. *Nat Immunol* **4**, 380-386 (2003).

45. Kashiwada, M., Pham, N.L., Pewe, L.L., Harty, J.T. & Rothman, P.B. NFIL3/E4BP4 is a key transcription factor for CD8alpha(+) dendritic cell development. *Blood* **117**, 6193-6197 (2011).

46. Miller, J.C.*, et al.* Deciphering the transcriptional network of the dendritic cell lineage. *Nat Immunol* **13**, 888-899 (2012).

47. Roberts, Edward W.*, et al.* Critical Role for CD103+/CD141+ Dendritic Cells Bearing CCR7 for Tumor Antigen Trafficking and Priming of T Cell Immunity in Melanoma. *Cancer Cell* **30**, 324-336 (2016).

48. Salmon, H.*, et al.* Expansion and Activation of CD103+ Dendritic Cell Progenitors at the Tumor Site Enhances Tumor Responses to Therapeutic PD-L1 and BRAF Inhibition. *Immunity* **44**, 924-938 (2016).

49. Sánchez-Paulete, A.R.*, et al.* Cancer Immunotherapy with Immunomodulatory Anti-CD137 and Anti-PD-1 Monoclonal Antibodies Requires BATF3-Dependent Dendritic Cells. *Cancer discovery* **6**, 71-79 (2016).

50. Ruffell, B.*, et al.* Macrophage IL-10 blocks CD8+ T cell-dependent responses to chemotherapy by suppressing IL-12 expression in intratumoral dendritic cells. *Cancer Cell* **26**, 623-637 (2014).

51. Tamura, T.*, et al.* IFN regulatory factor-4 and -8 govern dendritic cell subset development and their functional diversity. *Journal of immunology (Baltimore, Md. : 1950)* **174**, 2573-2581 (2005).

52. Scott, C.L.*, et al.* The transcription factor Zeb2 regulates development of conventional and plasmacytoid DCs by repressing Id2. *The Journal of experimental medicine* **213**, 897-911 (2016).

53. Granot, T.*, et al.* Dendritic Cells Display Subset and Tissue-Specific Maturation Dynamics over Human Life. *Immunity* **46**, 504-515 (2017).

54. Villani, A.C.*, et al.* Single-cell RNA-seq reveals new types of human blood dendritic cells, monocytes, and progenitors. *Science (New York, N.Y.)* **356**(2017).

55. Laoui, D.*, et al.* The tumour microenvironment harbours ontogenically distinct dendritic cell populations with opposing effects on tumour immunity. *Nature communications* **7**, 13720 (2016).

56. Russell, J.H. & Ley, T.J. Lymphocyte-mediated cytotoxicity. *Annual review of immunology* **20**, 323-370 (2002).

57. Brinkman, C.C., Peske Jd Fau - Engelhard, V.H. & Engelhard, V.H. Peripheral tissue homing receptor control of naive, effector, and memory CD8 T cell localization in lymphoid and non-lymphoid tissues.

58. Bierer, B.E. & Burakoff, S.J. T cell adhesion molecules. *FASEB journal : official publication of the Federation of American Societies for Experimental Biology* **2**, 2584-2590 (1988).

59. Vesely, M.D. & Schreiber, R.D. Cancer immunoediting: antigens, mechanisms, and implications to cancer immunotherapy. *Annals of the New York Academy of Sciences* **1284**, 1-5 (2013).

60. Willimsky, G. & Blankenstein, T. Sporadic immunogenic tumours avoid destruction by inducing T-cell tolerance. *Nature* **437**, 141-146 (2005).

61. Garbe, A.I.*, et al.* Genetically induced pancreatic adenocarcinoma is highly immunogenic and causes spontaneous tumor-specific immune responses. *Cancer Res.* **66**, 508-516 (2006).

62. DuPage, M.*, et al.* Endogenous T cell responses to antigens expressed in lung adenocarcinomas delay malignant tumor progression. *Cancer Cell* **19**, 72-85 (2011).

63. Pauken, K.E. & Wherry, E.J. Overcoming T cell exhaustion in infection and cancer. *Trends Immunol.* **36**, 265-276 (2015).

64. Wherry, E.J. T cell exhaustion. *Nat Immunol* **12**, 492-499 (2011).

65. Philip, M.*, et al.* Chromatin states define tumour-specific T cell dysfunction and reprogramming. *Nature* **545**, 452-456 (2017).

66. Pauken, K.E.*, et al.* Epigenetic stability of exhausted T cells limits durability of reinvigoration by PD-1 blockade. *Science (New York, N.Y.)* **354**, 1160-1165 (2016).

67. Schietinger, A.*, et al.* Tumor-Specific T Cell Dysfunction Is a Dynamic Antigen-Driven Differentiation Program Initiated Early during Tumorigenesis. *Immunity* **45**, 389-401 (2016).

68. Jenkins, M.K.*, et al.* In vivo activation of antigen-specific CD4 T cells. *Annual review of immunology* **19**, 23-45 (2001).

69. Zhu, J., Yamane, H. & Paul, W.E. Differentiation of effector CD4 T cell populations (*). *Annual review of immunology* **28**, 445-489 (2010).

70. Szabo, S.J.*, et al.* A novel transcription factor, T-bet, directs Th1 lineage commitment. *Cell* **100**, 655-669 (2000).

71. Ho, I.C., Tai, T.S. & Pai, S.Y. GATA3 and the T-cell lineage: essential functions before and after T-helper-2-cell differentiation. *Nat Rev Immunol* **9**, 125-135 (2009).

72. Wang, N., Liang, H. & Zen, K. Molecular mechanisms that influence the macrophage m1-m2 polarization balance. *Frontiers in immunology* **5**, 614 (2014).

73. Ivanov, II*, et al.* The orphan nuclear receptor RORgammat directs the differentiation program of proinflammatory IL-17+ T helper cells. *Cell* **126**, 1121-1133 (2006).

74. Kryczek, I.*, et al.* Cutting edge: Th17 and regulatory T cell dynamics and the regulation by IL-2 in the tumor microenvironment. *Journal of immunology (Baltimore, Md. : 1950)* **178**, 6730-6733 (2007).

75. Muranski, P.*, et al.* Tumor-specific Th17-polarized cells eradicate large established melanoma. *Blood* **112**, 362-373 (2008).

76. Hung, K.*, et al.* The central role of CD4(+) T cells in the antitumor immune response. *The Journal of experimental medicine* **188**, 2357-2368 (1998).

77. Tempero, R.M.*, et al.* CD4+ lymphocytes provide MUC1-specific tumor immunity in vivo that is undetectable in vitro and is absent in MUC1 transgenic mice. *Journal of immunology (Baltimore, Md. : 1950)* **161**, 5500-5506 (1998).

78. Bennett, S.R., Carbone, F.R., Karamalis, F., Miller, J.F. & Heath, W.R. Induction of a CD8+ cytotoxic T lymphocyte response by cross-priming requires cognate CD4+ T cell help. *The Journal of experimental medicine* **186**, 65-70 (1997).

79. Ossendorp, F., Mengede, E., Camps, M., Filius, R. & Melief, C.J. Specific T helper cell requirement for optimal induction of cytotoxic T lymphocytes against major histocompatibility complex class II negative tumors. *The Journal of experimental medicine* **187**, 693-702 (1998).

80. Shiao, S.L.*, et al.* TH2-Polarized CD4(+) T Cells and Macrophages Limit Efficacy of Radiotherapy. *Cancer immunology research* **3**, 518-525 (2015).

81. DeNardo, D.G.*, et al.* CD4(+) T cells regulate pulmonary metastasis of mammary carcinomas by enhancing protumor properties of macrophages. *Cancer Cell* **16**, 91-102 (2009).

82. Chen, W.*, et al.* Conversion of peripheral CD4+CD25- naive T cells to CD4+CD25+ regulatory T cells by TGF-beta induction of transcription factor Foxp3. *The Journal of experimental medicine* **198**, 1875-1886 (2003).

83. Josefowicz, S.Z., Lu, L.F. & Rudensky, A.Y. Regulatory T cells: mechanisms of differentiation and function. *Annual review of immunology* **30**, 531-564 (2012).

84. Plitas, G.*, et al.* Regulatory T Cells Exhibit Distinct Features in Human Breast Cancer. *Immunity* **45**, 1122-1134 (2016).

85. Curiel, T.J.*, et al.* Specific recruitment of regulatory T cells in ovarian carcinoma fosters immune privilege and predicts reduced survival. *Nature medicine* **10**, 942-949 (2004).

86. Bates, G.J.*, et al.* Quantification of regulatory T cells enables the identification of high-risk breast cancer patients and those at risk of late relapse. *Journal of clinical oncology : official journal of the American Society of Clinical Oncology* **24**, 5373-5380 (2006).

87. Bos, P.D., Plitas, G., Rudra, D., Lee, S.Y. & Rudensky, A.Y. Transient regulatory T cell ablation deters oncogene-driven breast cancer and enhances radiotherapy. *The Journal of experimental medicine* **210**, 2435-2466 (2013).

88. Vignali, D.A., Collison, L.W. & Workman, C.J. How regulatory T cells work. *Nat Rev Immunol* **8**, 523-532 (2008).

89. Qureshi, O.S.*, et al.* Trans-endocytosis of CD80 and CD86: a molecular basis for the cell-extrinsic function of CTLA-4. *Science (New York, N.Y.)* **332**, 600-603 (2011).

90. Simpson, T.R.*, et al.* Fc-dependent depletion of tumor-infiltrating regulatory T cells co-defines the efficacy of anti-CTLA-4 therapy against melanoma. *The Journal of experimental medicine* **210**, 1695-1710 (2013).

91. Arce Vargas, F.*, et al.* Fc-Optimized Anti-CD25 Depletes Tumor-Infiltrating Regulatory T Cells and Synergizes with PD-1 Blockade to Eradicate Established Tumors. *Immunity* **46**, 577-586 (2017).

92. Ali, H.R., Chlon, L., Pharoah, P.D., Markowetz, F. & Caldas, C. Patterns of Immune Infiltration in Breast Cancer and Their Clinical Implications: A Gene-Expression-Based Retrospective Study. *PLoS medicine* **13**, e1002194 (2016).

93. Newman, A.M.*, et al.* Robust enumeration of cell subsets from tissue expression profiles. *Nat. Methods* **12**, 453-457 (2015).

94. Aran, D., Hu, Z. & Butte, A.J. xCell: digitally portraying the tissue cellular heterogeneity landscape. *Genome biology* **18**, 220 (2017).

95. Bindea, G.*, et al.* Spatiotemporal dynamics of intratumoral immune cells reveal the immune landscape in human cancer. *Immunity* **39**, 782-795 (2013).

96. Mlecnik, B.*, et al.* Integrative Analyses of Colorectal Cancer Show Immunoscore Is a Stronger Predictor of Patient Survival Than Microsatellite Instability. *Immunity* **44**, 698-711 (2016).

97. Herbst, R.S.*, et al.* Predictive correlates of response to the anti-PD-L1 antibody MPDL3280A in cancer patients. *Nature* **515**, 563-567 (2014).

98. Ademmer, K.*, et al.* Effector T lymphocyte subsets in human pancreatic cancer: detection of CD8+CD18+ cells and CD8+CD103+ cells by multi-epitope imaging. *Clinical and experimental immunology* **112**, 21-26 (1998).

99. Beatty, G.L.*, et al.* Exclusion of T Cells From Pancreatic Carcinomas in Mice Is Regulated by Ly6C(low) F4/80(+) Extratumoral Macrophages. *Gastroenterology* **149**, 201-210 (2015).

100. Spranger, S. Mechanisms of tumor escape in the context of the T-cell-inflamed and the non-T-cell-inflamed tumor microenvironment. *International immunology* **28**, 383-391 (2016).

101. Evans, R.A.*, et al.* Lack of immunoediting in murine pancreatic cancer reversed with neoantigen. *JCI insight* **1**(2016).

102. Lee, H.J.*, et al.* Tertiary lymphoid structures: prognostic significance and relationship with tumour-infiltrating lymphocytes in triple-negative breast cancer. *Journal of clinical pathology* **69**, 422-430 (2016).

103. Finkin, S.*, et al.* Ectopic lymphoid structures function as microniches for tumor progenitor cells in hepatocellular carcinoma. *Nat Immunol* **16**, 1235-1244 (2015).

104. Neyt, K., Perros, F., GeurtsvanKessel, C.H., Hammad, H. & Lambrecht, B.N. Tertiary lymphoid organs in infection and autoimmunity. *Trends Immunol* **33**, 297-305 (2012).

105. Lutz, E.R.*, et al.* Immunotherapy converts nonimmunogenic pancreatic tumors into immunogenic foci of immune regulation. *Cancer immunology research* **2**, 616-631 (2014).

106. Sumimoto, H., Imabayashi, F., Iwata, T. & Kawakami, Y. The BRAF-MAPK signaling pathway is essential for cancer-immune evasion in human melanoma cells. *The Journal of experimental medicine* **203**, 1651-1656 (2006).

107. Pylayeva-Gupta, Y., Lee, K.E., Hajdu, C.H., Miller, G. & Bar-Sagi, D. Oncogenic Kras-induced GM-CSF production promotes the development of pancreatic neoplasia. *Cancer Cell* **21**, 836-847 (2012).

108. Bayne, L.J.*, et al.* Tumor-derived granulocyte-macrophage colony-stimulating factor regulates myeloid inflammation and T cell immunity in pancreatic cancer. *Cancer Cell* **21**, 822-835 (2012).

109. Spranger, S., Dai, D., Horton, B. & Gajewski, T.F. Tumor-Residing Batf3 Dendritic Cells Are Required for Effector T Cell Trafficking and Adoptive T Cell Therapy. *Cancer Cell* **31**, 711-723 e714 (2017).

110. Spranger, S., Bao, R. & Gajewski, T.F. Melanoma-intrinsic β-catenin signalling prevents anti-tumour immunity. *Nature* **523**, 231-235 (2015).

111. Qian, B.-Z.*, et al.* CCL2 recruits inflammatory monocytes to facilitate breast-tumour metastasis. *Nature* **475**, 222-225 (2011).

112. Bonavita, E.*, et al.* PTX3 is an extrinsic oncosuppressor regulating complement-dependent inflammation in cancer. *Cell* **160**, 700-714 (2015).

113. Condeelis, J. & Pollard, J.W. Macrophages: obligate partners for tumor cell migration, invasion, and metastasis. *Cell* **124**, 263-266 (2006).

114. Lin, E.Y., Nguyen, A.V., Russell, R.G. & Pollard, J.W. Colony-stimulating factor 1 promotes progression of mammary tumors to malignancy. *The Journal of experimental medicine* **193**, 727-740 (2001).

115. Scholl, S.M.*, et al.* Anti-colony-stimulating factor-1 antibody staining in primary breast adenocarcinomas correlates with marked inflammatory cell infiltrates and prognosis. *Journal of the National Cancer Institute* **86**, 120-126 (1994).

116. Pollard, J.W. Tumour-educated macrophages promote tumour progression and metastasis. *Nature reviews. Cancer* **4**, 71-78 (2004).

117. Khalili, J.S.*, et al.* Oncogenic BRAF(V600E) promotes stromal cell-mediated immunosuppression via induction of interleukin-1 in melanoma. *Clinical cancer research : an official journal of the American Association for Cancer Research* **18**, 5329-5340 (2012).

118. Lujambio, A.*, et al.* Non-cell-autonomous tumor suppression by p53. *Cell* **153**, 449-460 (2013).

119. Guinney, J.*, et al.* The consensus molecular subtypes of colorectal cancer. *Nature medicine* **21**, 1350-1356 (2015).

120. Angelova, M.*, et al.* Characterization of the immunophenotypes and antigenomes of colorectal cancers reveals distinct tumor escape mechanisms and novel targets for immunotherapy. *Genome biology* **16**, 64 (2015).

121. Becht, E.*, et al.* Immune and Stromal Classification of Colorectal Cancer Is Associated with Molecular Subtypes and Relevant for Precision Immunotherapy. *Clinical cancer research : an official journal of the American Association for Cancer Research* **22**, 4057-4066 (2016).

122. Gatalica, Z.*, et al.* Programmed cell death 1 (PD-1) and its ligand (PD-L1) in common cancers and their correlation with molecular cancer type. *Cancer epidemiology, biomarkers & prevention : a publication of the American Association for Cancer Research, cosponsored by the American Society of Preventive Oncology* **23**, 2965-2970 (2014).

123. Boland, P.M. & Ma, W.W. Immunotherapy for Colorectal Cancer. *Cancers* **9**(2017).

124. Koelwyn, G.J., Quail, D.F., Zhang, X., White, R.M. & Jones, L.W. Exercise-dependent regulation of the tumour microenvironment. *Nature reviews. Cancer* **17**, 620-632 (2017).

125. Shaw, A.C., Goldstein, D.R. & Montgomery, R.R. Age-dependent dysregulation of innate immunity. *Nat Rev Immunol* **13**, 875-887 (2013).

126. Julia, V., Macia, L. & Dombrowicz, D. The impact of diet on asthma and allergic diseases. *Nat Rev Immunol* **15**, 308-322 (2015).

127. Tall, A.R. & Yvan-Charvet, L. Cholesterol, inflammation and innate immunity. *Nat Rev Immunol* **15**, 104-116 (2015).

128. Hooper, L.V., Littman, D.R. & Macpherson, A.J. Interactions between the microbiota and the immune system. *Science (New York, N.Y.)* **336**, 1268-1273 (2012).

129. Robinson, D.P., Lorenzo, M.E., Jian, W. & Klein, S.L. Elevated 17beta-estradiol protects females from influenza A virus pathogenesis by suppressing inflammatory responses. *PLoS pathogens* **7**, e1002149 (2011).

130. Ridker, P.M.*, et al.* Effect of interleukin-1beta inhibition with canakinumab on incident lung cancer in patients with atherosclerosis: exploratory results from a randomised, double-blind, placebo-controlled trial. *Lancet (London, England)* **390**, 1833-1842 (2017).

131. Cook, N.R.*, et al.* Low-dose aspirin in the primary prevention of cancer: the Women's Health Study: a randomized controlled trial. *Jama* **294**, 47-55 (2005).

132. Burn, J.*, et al.* Long-term effect of aspirin on cancer risk in carriers of hereditary colorectal cancer: an analysis from the CAPP2 randomised controlled trial. *Lancet (London, England)* **378**, 2081-2087 (2011).

133. Zelenay, S.*, et al.* Cyclooxygenase-Dependent Tumor Growth through Evasion of Immunity. *Cell* **162**, 1257-1270 (2015).

134. Marigo, I.*, et al.* Tumor-induced tolerance and immune suppression depend on the C/EBPbeta transcription factor. *Immunity* **32**, 790-802 (2010).

135. Kowanetz, M.*, et al.* Granulocyte-colony stimulating factor promotes lung metastasis through mobilization of Ly6G+Ly6C+ granulocytes. *Proceedings of the National Academy of Sciences of the United States of America* **107**, 21248-21255 (2010).

136. Waight, J.D., Hu, Q., Miller, A., Liu, S. & Abrams, S.I. Tumor-Derived G-CSF Facilitates Neoplastic Growth through a Granulocytic Myeloid-Derived Suppressor Cell-Dependent Mechanism. *PLoS ONE* **6**, e27690 (2011).

137. Engblom, C.*, et al.* Osteoblasts remotely supply lung tumors with cancer-promoting SiglecF(high) neutrophils. *Science (New York, N.Y.)* **358**(2017).

138. Cortez-Retamozo, V.*, et al.* Angiotensin II drives the production of tumor-promoting macrophages. *Immunity* **38**, 296-308 (2013).

139. Pucci, F.*, et al.* PF4 Promotes Platelet Production and Lung Cancer Growth. *Cell reports* **17**, 1764-1772 (2016).

140. Verschoor, C.P.*, et al.* Blood CD33(+)HLA-DR(-) myeloid-derived suppressor cells are increased with age and a history of cancer. *Journal of leukocyte biology* **93**, 633-637 (2013).

141. Ruhland, M.K.*, et al.* Stromal senescence establishes an immunosuppressive microenvironment that drives tumorigenesis. *Nature communications* **7**, 11762 (2016).

142. Hale, M.*, et al.* Obesity triggers enhanced MDSC accumulation in murine renal tumors via elevated local production of CCL2. *PLoS One* **10**, e0118784 (2015).

143. Svoronos, N.*, et al.* Tumor Cell-Independent Estrogen Signaling Drives Disease Progression through Mobilization of Myeloid-Derived Suppressor Cells. *Cancer discovery* **7**, 72-85 (2017).

144. Thompson, M.G., Peiffer, D.S., Larson, M., Navarro, F. & Watkins, S.K. FOXO3, estrogen receptor alpha, and androgen receptor impact tumor growth rate and infiltration of dendritic cell subsets differentially between male and female mice. *Cancer immunology, immunotherapy : CII* **66**, 615-625 (2017).

145. Sivan, A.*, et al.* Commensal Bifidobacterium promotes antitumor immunity and facilitates anti-PD-L1 efficacy. *Science (New York, N.Y.)* **350**, 1084-1089 (2015).

146. Vetizou, M.*, et al.* Anticancer immunotherapy by CTLA-4 blockade relies on the gut microbiota. *Science (New York, N.Y.)* **350**, 1079-1084 (2015).

147. Kokolus, K.M.*, et al.* Baseline tumor growth and immune control in laboratory mice are significantly influenced by subthermoneutral housing temperature. *Proceedings of the National Academy of Sciences of the United States of America* **110**, 20176-20181 (2013).

148. Kokolus, K.M.*, et al.* Stressful presentations: mild cold stress in laboratory mice influences phenotype of dendritic cells in naive and tumor-bearing mice. *Frontiers in immunology* **5**, 23 (2014).

149. Flint, T.R.*, et al.* Tumor-Induced IL-6 Reprograms Host Metabolism to Suppress Anti-tumor Immunity. *Cell metabolism* **24**, 672-684 (2016).

150. Pietrocola, F.*, et al.* Caloric Restriction Mimetics Enhance Anticancer Immunosurveillance. *Cancer Cell* **30**, 147-160 (2016).

151. Di Biase, S.*, et al.* Fasting-Mimicking Diet Reduces HO-1 to Promote T Cell-Mediated Tumor Cytotoxicity. *Cancer Cell* **30**, 136-146 (2016).

152. Wang, A.*, et al.* Opposing Effects of Fasting Metabolism on Tissue Tolerance in Bacterial and Viral Inflammation. *Cell* **166**, 1512-1525 e1512 (2016).

153. Smyth, M.J., Ngiow, S.F., Ribas, A. & Teng, M.W. Combination cancer immunotherapies tailored to the tumour microenvironment. *Nature reviews. Clinical oncology* **13**, 143-158 (2016).

154. Tsujikawa, T.*, et al.* Quantitative Multiplex Immunohistochemistry Reveals Myeloid-Inflamed Tumor-Immune Complexity Associated with Poor Prognosis. *Cell reports* **19**, 203-217 (2017).

155. Spitzer, M.H.*, et al.* Systemic Immunity Is Required for Effective Cancer Immunotherapy. *Cell* **168**, 487-502.e415 (2017).

156. Lavin, Y.*, et al.* Innate Immune Landscape in Early Lung Adenocarcinoma by Paired Single-Cell Analyses. *Cell* **169**, 750-765.e717 (2017).

157. Tirosh, I.*, et al.* Dissecting the multicellular ecosystem of metastatic melanoma by single-cell RNA-seq. *Science (New York, N.Y.)* **352**, 189-196 (2016).

158. Cong, L.*, et al.* Multiplex genome engineering using CRISPR/Cas systems. *Science (New York, N.Y.)* **339**, 819-823 (2013).

159. Wang, H.*, et al.* One-step generation of mice carrying mutations in multiple genes by CRISPR/Cas-mediated genome engineering. *Cell* **153**, 910-918 (2013).

160. Hodi, F.S.*, et al.* Immunologic and clinical effects of antibody blockade of cytotoxic T lymphocyte-associated antigen 4 in previously vaccinated cancer

patients. *Proceedings of the National Academy of Sciences of the United States of America* **105**, 3005-3010 (2008).

161. Huang, A.C.*, et al.* T-cell invigoration to tumour burden ratio associated with anti-PD-1 response. *Nature* **545**, 60-65 (2017).

162. Topalian, S.L.*, et al.* Survival, durable tumor remission, and long-term safety in patients with advanced melanoma receiving nivolumab. *Journal of clinical oncology : official journal of the American Society of Clinical Oncology* **32**, 1020-1030 (2014).

163. Larkin, J.*, et al.* Combined Nivolumab and Ipilimumab or Monotherapy in Untreated Melanoma. *The New England journal of medicine* **373**, 23-34 (2015).

164. Tumeh, P.C.*, et al.* PD-1 blockade induces responses by inhibiting adaptive immune resistance. *Nature* **515**, 568-571 (2014).

165. Behrens, G.*, et al.* Helper T cells, dendritic cells and CTL Immunity. *Immunology and cell biology* **82**, 84-90 (2004).

166. Corthay, A.*, et al.* Primary antitumor immune response mediated by CD4+ T cells. *Immunity* **22**, 371-383 (2005).

167. Laidlaw, B.J., Craft, J.E. & Kaech, S.M. The multifaceted role of CD4(+) T cells in CD8(+) T cell memory. *Nat Rev Immunol* **16**, 102-111 (2016).

168. Quezada, S.A.*, et al.* Tumor-reactive CD4(+) T cells develop cytotoxic activity and eradicate large established melanoma after transfer into lymphopenic hosts. *The Journal of experimental medicine* **207**, 637-650 (2010).

169. Curran, M.A., *et al.* Systemic 4-1BB activation induces a novel T cell phenotype driven by high expression of Eomesodermin. *The Journal of experimental medicine* **210**, 743-755 (2013).

170. Johnson, D.B., *et al.* Melanoma-specific MHC-II expression represents a tumour-autonomous phenotype and predicts response to anti-PD-1/PD-L1 therapy. *Nature communications* **7**, 10582 (2016).

171. Fan, X., Quezada, S.A., Sepulveda, M.A., Sharma, P. & Allison, J.P. Engagement of the ICOS pathway markedly enhances efficacy of CTLA-4 blockade in cancer immunotherapy. *The Journal of experimental medicine* **211**, 715-725 (2014).

172. Zappasodi, R., *et al.* Non-conventional Inhibitory CD4(+)Foxp3(-)PD-1(hi) T Cells as a Biomarker of Immune Checkpoint Blockade Activity. *Cancer Cell* **33**, 1017-1032.e1017 (2018).

173. Bauer, C.A., *et al.* Dynamic Treg interactions with intratumoral APCs promote local CTL dysfunction. *The Journal of clinical investigation* **124**, 2425-2440 (2014).

174. Gutierrez-Martinez, E., *et al.* Cross-Presentation of Cell-Associated Antigens by MHC Class I in Dendritic Cell Subsets. *Frontiers in immunology* **6**, 363 (2015).

175. Gerner, M.Y., Casey, K.A., Kastenmuller, W. & Germain, R.N. Dendritic cell and antigen dispersal landscapes regulate T cell immunity. *The Journal of experimental medicine* **214**, 3105-3122 (2017).

176. Belz, G.T., Shortman, K., Bevan, M.J. & Heath, W.R. CD8alpha+ dendritic cells selectively present MHC class I-restricted noncytolytic viral and intracellular

bacterial antigens in vivo. *Journal of immunology (Baltimore, Md. : 1950)* **175**, 196-200 (2005).

177. Bedoui, S.*, et al.* Cross-presentation of viral and self antigens by skin-derived CD103+ dendritic cells. *Nat Immunol* **10**, 488-495 (2009).

178. Gao, Y.*, et al.* Control of T helper 2 responses by transcription factor IRF4-dependent dendritic cells. *Immunity* **39**, 722-732 (2013).

179. Krishnaswamy, J.K.*, et al.* Migratory CD11b(+) conventional dendritic cells induce T follicular helper cell-dependent antibody responses. *Science immunology* **2**(2017).

180. Heng, T.S. & Painter, M.W. The Immunological Genome Project: networks of gene expression in immune cells. *Nat Immunol* **9**, 1091-1094 (2008).

181. Baratin, M.*, et al.* T Cell Zone Resident Macrophages Silently Dispose of Apoptotic Cells in the Lymph Node. *Immunity* **47**, 349-362.e345 (2017).

182. Alferink, J.*, et al.* Compartmentalized production of CCL17 in vivo: strong inducibility in peripheral dendritic cells contrasts selective absence from the spleen. *The Journal of experimental medicine* **197**, 585-599 (2003).

183. Kumamoto, Y., Hirai, T., Wong, P.W., Kaplan, D.H. & Iwasaki, A. CD301b(+) dendritic cells suppress T follicular helper cells and antibody responses to protein antigens. *eLife* **5**(2016).

184. Satpathy, A.T.*, et al.* Zbtb46 expression distinguishes classical dendritic cells and their committed progenitors from other immune lineages. *The Journal of experimental medicine* **209**, 1135-1152 (2012).

185. Meredith, M.M.*, et al.* Expression of the zinc finger transcription factor zDC (Zbtb46, Btbd4) defines the classical dendritic cell lineage. *The Journal of experimental medicine* **209**, 1153-1165 (2012).

186. Allison, K.A.*, et al.* Affinity and dose of TCR engagement yield proportional enhancer and gene activity in CD4+ T cells. *eLife* **5**(2016).

187. Shiow, L.R.*, et al.* CD69 acts downstream of interferon-alpha/beta to inhibit S1P1 and lymphocyte egress from lymphoid organs. *Nature* **440**, 540-544 (2006).

188. Sun, S., Zhang, X., Tough, D.F. & Sprent, J. Type I interferon-mediated stimulation of T cells by CpG DNA. *The Journal of experimental medicine* **188**, 2335-2342 (1998).

189. Chiba, K.*, et al.* FTY720, a novel immunosuppressant, induces sequestration of circulating mature lymphocytes by acceleration of lymphocyte homing in rats. I. FTY720 selectively decreases the number of circulating mature lymphocytes by acceleration of lymphocyte homing. *Journal of immunology (Baltimore, Md. : 1950)* **160**, 5037-5044 (1998).

190. Mandal, R.*, et al.* The head and neck cancer immune landscape and its immunotherapeutic implications. *JCI insight* **1**, e89829 (2016).

191. Barry, K.C.*, et al.* A natural killer-dendritic cell axis defines checkpoint therapy-responsive tumor microenvironments. *Nature medicine* (2018).

192. Tussiwand, R.*, et al.* Klf4 expression in conventional dendritic cells is required for T helper 2 cell responses. *Immunity* **42**, 916-928 (2015).

193. Ochiai, S.*, et al.* CD326(lo)CD103(lo)CD11b(lo) dermal dendritic cells are activated by thymic stromal lymphopoietin during contact sensitization in mice. *Journal of immunology (Baltimore, Md. : 1950)* **193**, 2504-2511 (2014).

194. Kumamoto, Y.*, et al.* CD301b(+) dermal dendritic cells drive T helper 2 cell-mediated immunity. *Immunity* **39**, 733-743 (2013).

195. Nirschl, C.J.*, et al.* IFNgamma-Dependent Tissue-Immune Homeostasis Is Co-opted in the Tumor Microenvironment. *Cell* **170**, 127-141.e115 (2017).

196. Wallin, J.J.*, et al.* Atezolizumab in combination with bevacizumab enhances antigen-specific T-cell migration in metastatic renal cell carcinoma. *Nature communications* **7**, 12624 (2016).

197. Pandiyan, P., Zheng, L., Ishihara, S., Reed, J. & Lenardo, M.J. CD4+CD25+Foxp3+ regulatory T cells induce cytokine deprivation-mediated apoptosis of effector CD4+ T cells. *Nat Immunol* **8**, 1353-1362 (2007).

198. Zou, T., Caton, A.J., Koretzky, G.A. & Kambayashi, T. Dendritic cells induce regulatory T cell proliferation through antigen-dependent and -independent interactions. *Journal of immunology (Baltimore, Md. : 1950)* **185**, 2790-2799 (2010).

199. Liang, J.*, et al.* Inflammatory Th1 and Th17 in the Intestine Are Each Driven by Functionally Specialized Dendritic Cells with Distinct Requirements for MyD88. *Cell reports* **17**, 1330-1343 (2016).

200. Wei, S.C.*, et al.* Distinct Cellular Mechanisms Underlie Anti-CTLA-4 and Anti-PD-1 Checkpoint Blockade. *Cell* **170**, 1120-1133.e1117 (2017).

201. Shang, B., Liu, Y., Jiang, S.J. & Liu, Y. Prognostic value of tumor-infiltrating FoxP3+ regulatory T cells in cancers: a systematic review and meta-analysis. *Scientific reports* **5**, 15179 (2015).

202. Binnewies, M.*, et al.* Understanding the tumor immune microenvironment (TIME) for effective therapy. *Nature medicine* **24**, 541-550 (2018).

203. Puram, S.V.*, et al.* Single-Cell Transcriptomic Analysis of Primary and Metastatic Tumor Ecosystems in Head and Neck Cancer. *Cell* **171**, 1611-1624.e1624 (2017).

204. Azizi, E.*, et al.* Single-Cell Map of Diverse Immune Phenotypes in the Breast Tumor Microenvironment. *Cell* (2018).

205. Barry, K.C.*, et al.* A natural killer–dendritic cell axis defines checkpoint therapy–responsive tumor microenvironments. *Nature medicine* (2018).

206. Engelhardt, J.J.*, et al.* Marginating dendritic cells of the tumor microenvironment cross-present tumor antigens and stably engage tumor-specific T cells. *Cancer Cell* **21**, 402-417 (2012).

207. Dranoff, G.*, et al.* Vaccination with irradiated tumor cells engineered to secrete murine granulocyte-macrophage colony-stimulating factor stimulates potent, specific, and long-lasting anti-tumor immunity. *Proceedings of the National Academy of Sciences of the United States of America* **90**, 3539-3543 (1993).

208. Dobin, A.*, et al.* STAR: ultrafast universal RNA-seq aligner. *Bioinformatics (Oxford, England)* **29**, 15-21 (2013).

209. Satija, R., Farrell, J.A., Gennert, D., Schier, A.F. & Regev, A. Spatial reconstruction of single-cell gene expression data. *Nature biotechnology* **33**, 495-502 (2015).

210. Kowalczyk, M.S.*, et al.* Single-cell RNA-seq reveals changes in cell cycle and differentiation programs upon aging of hematopoietic stem cells. *Genome research* **25**, 1860-1872 (2015).

211. Macosko, E.Z.*, et al.* Highly Parallel Genome-wide Expression Profiling of Individual Cells Using Nanoliter Droplets. *Cell* **161**, 1202-1214 (2015).

212. Ritchie, M.E.*, et al.* limma powers differential expression analyses for RNA-sequencing and microarray studies. *Nucleic acids research* **43**, e47 (2015).

213. Benjamini, Y. & Hochberg, Y. Controlling the False Discovery Rate: A Practical and Powerful Approach to Multiple Testing. *Journal of the Royal Statistical Society. Series B (Methodological)* **57**, 289-300 (1995).

214. Thomas, P.G.*, et al.* An unexpected antibody response to an engineered influenza virus modifies CD8+ T cell responses. *Proceedings of the National Academy of Sciences of the United States of America* **103**, 2764-2769 (2006).

215. GeurtsvanKessel, C.H.*, et al.* Clearance of influenza virus from the lung depends on migratory langerin+CD11b- but not plasmacytoid dendritic cells. *The Journal of experimental medicine* **205**, 1621-1634 (2008).

Publishing Agreement

It is the policy of the University to encourage the distribution of all theses, dissertations, and manuscripts. Copies of all UCSF theses, dissertations, and manuscripts will be routed to the library via the Graduate Division. The library will make all theses, dissertations, and manuscripts accessible to the public and will preserve these to the best of their abilities, in perpetuity.

Please sign the following statement:

I hereby grant permission to the Graduate Division of the University of California, San Francisco to release copies of my thesis, dissertation, or manuscript to the Campus Library to provide access and preservation, in whole or in part, in perpetuity.

Author Signature

08/17/2018

Date